Biofluid Dynamics

P. Nithiarasu [1]

School of Engineering

Swansea University, SWansea SA2 8PP

[1]e-mail: P.Nithiarasu@swansea.ac.uk

Contents

3 Governing Equations   29

4 Analytical Forms   43

5 Computational Methods   51

Chapter 1

Introduction, Anatomy and Physiology

Biofluid dynamics may be defined as the topic that studies the fluid flow, fluid-structure interaction and heat and mass transfer in mammalian systems and in medical devices[1].

1.1 Importance of the Subject

The subject of biofluid dynamics is a fascinating subject due to the fact that it attracts attention from both the scientists and general public. We focus our attention on both the human body circulatory and respiratory systems. Understanding the circulatory system is one of the major areas of research and many engineering scientists have carried out some remarkable work. The respiratory system is very closely linked to the circulatory system and is extremely complex to study and understand. In addition to curiosity, the study of biofluid dynamics is directed towards finding solutions to some of the human body related diseases and disorders.

Unlike engineering applications, understanding human body biofluid dynamics is not easy. This is due to the fact that *in vivo* experiments are not easy to perform. Non-invasive experiments are useful but not always give the desired result. Thus, both theoretical and computational biofluid dynamics play a major role in the understanding of human body biofluid dynamics.

The extracorporeal systems, such as medical devices, can be experimentally tested by satisfying local government regulations. Real biofluids are often essential to test these devices. Such fluids can only be obtained by licensed bodies. Thus, in the development of medical devices both theoretical and computational biofluid dynamics play a major role at the early stages of design and development.

1.2 The Cardiovascular System

The cardiovascular system or *circulatory system* consists of the heart (pump) and a network of tubes that transport the blood. The heart consists of two pulsatile pumps in series and circulates blood through the vasculature (network)(see Figure 1.1(a)). The vasculature consists of *arteries, arterioles, capillaries, venules and veins*(see Figure1.1(b)). The cardiovascular system circulates about 5 litres of blood at a rate of approximately 6 l/m. The vasculature is normally divided into two parts: the *pulmonary* and *systemic* circulations. The network of blood vessels from the right heart to the lungs and back to the left heart is referred to as the pulmonary circulation system.
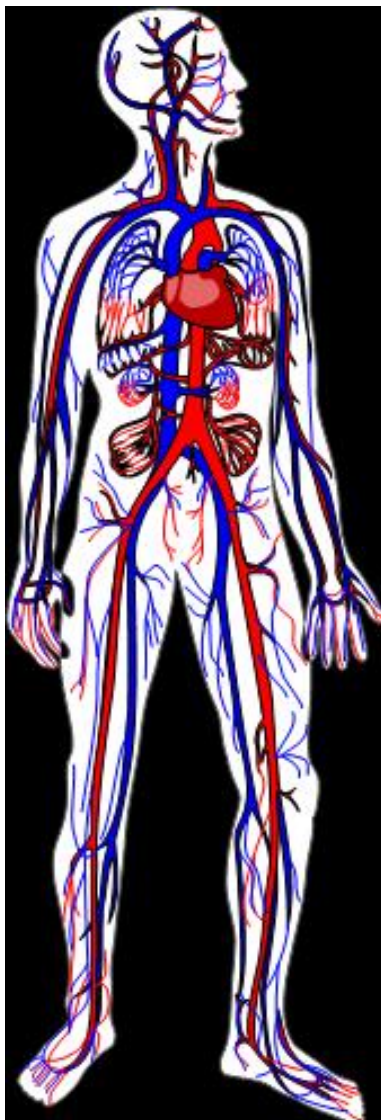
(a) Whole system
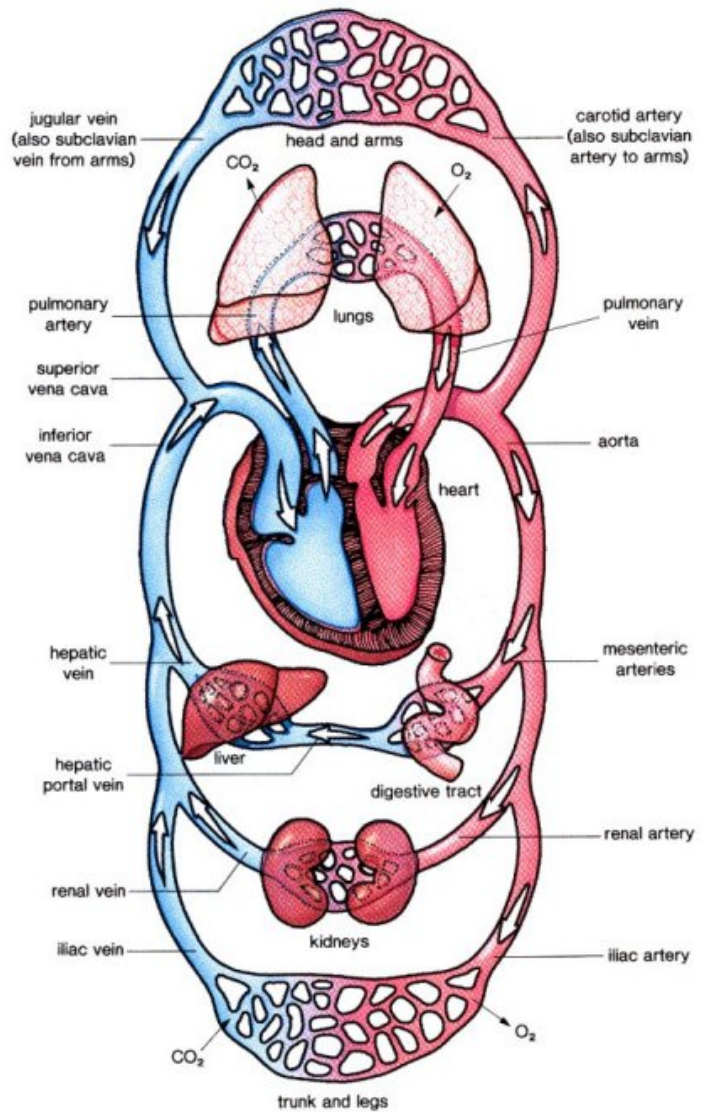
(b) Simplified system

Figure 1.1: Schematic description of the circulatory system[2].

Table 1.1: Approximate and average systemic vascular tree[3].

Type → / Parameters ↓	Aorta	Large arteries	Major arterial branches	Arterioles	Capillaries	Venules	Major venous branches	Large veins	Venae cavae
Number	1	Increasing	Increasing	0.16×10^9	5.0×10^9	0.5×10^9	Decreasing	Decreasing	2
Single vessel diameter (cm)	2.6	0.8	0.3 - 0.06	0.002	0.0009	0.0025	0.15-0.7	1.6	3.2
Total cross sectional area (cm^2)	5.3	20	20	500	3500	2700	100	30	18
Total volume (cm^3)	180	250	250	125	300	550	1150	900	250

The rest of the blood flow loop is called systemic circulation system. Both the divisions take the blood through large arteries first and then branches into smaller arteries before reaching arterioles and capillaries. After capillaries, the blood enters the venules before joining smaller veins first and then larger veins before reaching the right heart. Following subsections explain different parts and aspects of the circulatory system.

1.2.1   Pulmonary circulation

Figure 1.2 shows a sketch of the pulmonary circuit. This consists of tricuspid valve, right heart (right ventricle), pulmonary valve, pulmonary artery, lungs, pulmonary veins and right heart. In essence, this circuit is responsible for the gas exchange. The de-oxygenated blood from the right ventricle is pumped to the lungs where the capillaries surrounding the alveole sacks exchange carbon dioxide for oxygen. The red blood cells are responsible for this exchange before they are carried to the left ventricle of the heart.
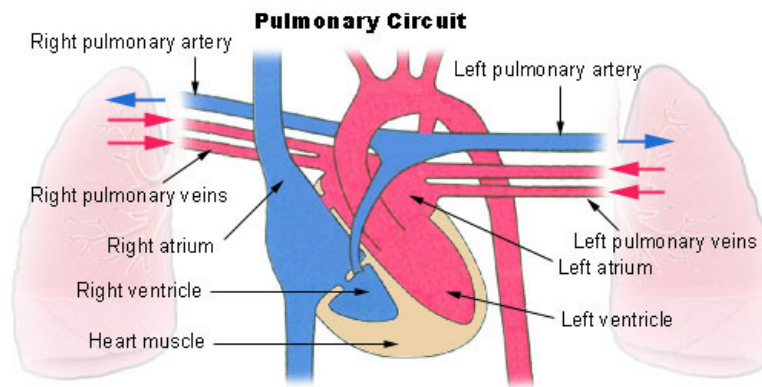
Figure 1.2: Pulmonary circuit[4].

1.2.2   Systemic circulation

While the pulmonary system is responsible for oxygenation of the blood, the systemic circulation is responsible for taking the oxygenated blood to various organs and tissues via the arterial tree before taking the deoxygenated blood to the right ventricle using the venous system(Figure 1.1(a)). Table 1.1 shows various parts of the human systemic circulation and their dimensions. It is important to remember that the data provided here is for a an average human systemic circulation.

1.2.3   The heart

The heart consists of two equally divided pumps in series as shown in Figure 1.3(a). These two pumps are divided by one single wall and they have a single electrical system for stimulation. Each pump consists of a pumping chamber (*ventricle*) and a holding chamber (*atrium*) and two non-return valves, one each for atrium and ventricle. The valve connecting the right atrium and the right ventricle is *tricuspid valve* and the valve connecting the right ventricle and the pulmonary

artery is called the *pulmonary valve*. The corresponding two valves of the left ventricle are referred to as *mitral* and *aortic* valves. Both the tricuspid and mitral valves are supported by connecting thin tissue strands and prevented from leaking. The pulmonary and aortic valves have no such tissue strands but they have three leaflets. These leaflets lean up against one another to avoid leaks when closed.

The pressure generated by the left heart is roughly three times higher ($\approx$13 kPa) than that of the right heart ($\approx$ 4 kPa). This is due to the fact that the thin capillary walls are essential for effective exchange of oxygen and carbon dioxide in lungs. Due to the very thin walls of the pulmonary capillaries, the pressure generated by the right heart should be smaller to avoid any damage to these thin walls. Due to this reason the thickness of the right heart muscle is much smaller than left ventricle muscles. The left ventricle needs to generate much higher pressure to handle the systemic circulation. The arterial walls are evolved to withstand the higher pressure generated by the left ventricle.

The cardiac cycle consists of *diastole* and *systole*. Diastole or atrial filling is the process of filling the ventricles. During diastole, the tricuspid and mitral valves open and establish the connection between the atria and ventricles. Both the pulmonary and aortic valves are closed during diastole. Both atria contract due to an electrical stimulus and force the blood into ventricles. Once the ventricles are filled with the blood, they are now stimulated and the atrial valves snap shut. The contraction of ventricles then results in the opening of the pulmonary and aortic valves. The processes of diastole and systole are schematically shown in Figure 1.3(b).

Figure 1.3(c) shows the cardiac cycle in detail. As seen both diastole and systole consist of several sub-processes. Lets start with systole this time and concentrate only on the left heart. Immediately after the ventricular filling stage, the atrial valve closes. The closing sound can be detected using a stethoscope. Figure 1.3(c) also shows the rapid change in both electrocardiogram and phonocardiogram. This more or less coincides with the isovolumic (this is due to the incompressible nature of blood) contraction of the ventricle. As soon as the ventricle pressure reaches the aortic pressure, the aortic valve pop opens and ejection takes place. After reaching a peak pressure, the pressure and volume of ventricle falls and reaches a isovolumic relaxation stage at which the aortic valve closes. The start of the relaxation stage is also the start of diastole and the ventricular volume at this stage is the lowest. At the end of relaxation period, the mitral valve opens and the volume of the ventricle start increasing at almost constant pressure. Initially a rapid flow takes place and at the middle of diastole passive filling of ventricles slows down and the atrium gets ready to contract. This latter process is called *diastasis*. After diastasis atrial contraction tales place and increases the pressure slightly inside the atrium to complete ventricular filling. Once the atrial systole is completed, the mitral valve closes and isovolumic contraction of ventricle starts and the cycles continue.

1.2.4   A typical arterial tree

Figure 1.4 shows an approximate arterial tree that includes all major arteries[7]. The numbered arteries in the figure are named in Table 1.2. Other details such as length, diameter and material properties are also given in this table. The material property β is given as

$$\beta = \frac{\sqrt{\pi}hE}{A_o(1-\sigma)^2} \tag{1.1}$$
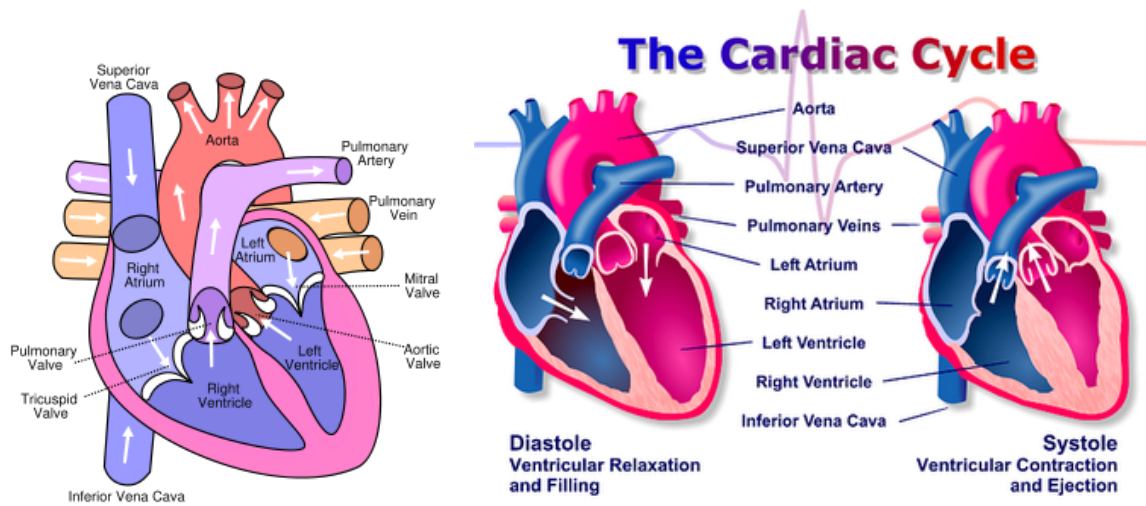
(a) The heart

(b) Cardiac cycle
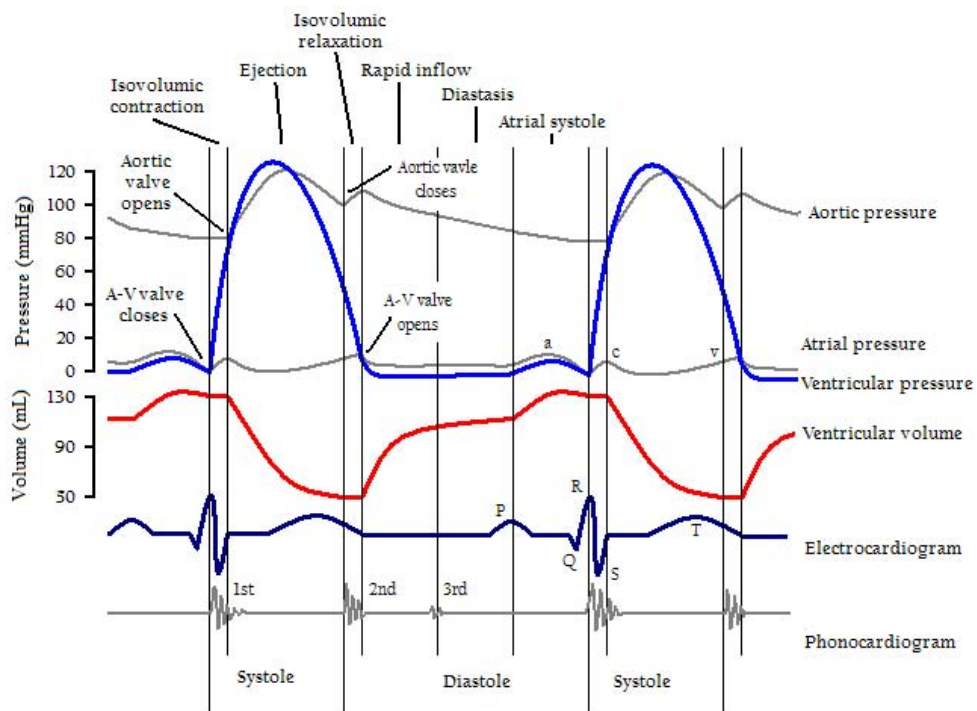
(c) Quantitative description

Figure 1.3: Schematic description of the human heart and cardiac cycle[4, 5, 6].

Table 1.2: Geometry and material properties of the arterial tree model. Data adapted from [8, 9, 10, 11]

Vessel	ID	L (cm)	A_0 (cm²)	β (10⁶dyne/cm³)	ID	Vessel	L (cm)	A_0 (cm²)	β (10⁶dyne/cm³)
Aortic Root	1	1	7.010	0.227	32	L Ulnar B	47.8	0.113 → 0.105	5.751 → 6.200
L Coronary	2	3	0.210	7.121	33	Intercostals	8	1.208 → 0.679	0.288 → 0.511
L Subendo.	3	7	0.120 → 0.060	12.462 → 24.924	34	Thoracic Aorta B	10.4	1.431 → 1.307	0.660 → 0.723
L Subepi.	4	7	0.120 → 0.060	12.462 → 24.924	35	Abdom. Aorta A	5.3	1.169	0.728
R Coronary	5	3	0.180	7.604	36	Coeliac	2	0.126	4.814
R Subendo.	6	7	0.103 → 0.052	13.289 → 26.577	37	Hepatic	12.5	0.152	3.046
R Subepi.	7	7	0.103 → 0.052	13.289 → 26.577	38	Splenic	6.3	0.102	4.179
Asc. Aorta	8	4	6.789 → 6.514	0.227 → 0.266	39	Gastric	7.1	0.238	2.149
Aortic Arch A	9	2	3.941	0.302	40	Sup. Mensenteric	17.2	0.283	2.307
Brachioceph.	10	3.4	1.535 → 1.208	0.277 → 0.528	41	Abdom. Aorta B	1	1.094	0.692
R Subclavian A	11	3.4	0.919 → 0.562	0.689 → 1.127	42	L Renal	3.2	0.212	2.359
R Carotid	12	17.7	0.430	1.385	43	Abdom. Aorta C	1	1.094	0.692
R Vertebral	13	14.8	0.111 → 0.105	7.662 → 8.087	44	R Renal	3.2	0.212	2.359
R Subclavian B	14	42.2	0.510 → 0.175	1.862 → 7.239	45	Abdom. Aorta D	10.6	1.057 → 0.943	0.671 → 0.751
R Radius	15	29	0.053 → 0.036	22.968 → 33.698	46	Inf. Mesenteric	5	0.080	5.054
R Ulnar A	16	6.7	0.145	8.983	47	Abdom. Aorta E	1	0.849	0.723
R Interosseous	17	7.9	0.026	40.697	48	L Common Iliac	5.9	0.425 → 0.385	1.333 → 1.474
R Ulnar B	18	30.3	0.129 → 0.105	6.718 → 8.266	49	R Common Iliac	5.8	0.425 → 0.385	1.333 → 1.474
R Int. Carotid	19	17.6	0.283 → 0.062	3.009 → 13.817	50	L Ext. Iliac	14.4	0.322 → 0.229	3.115 → 4.375
R Ext. Carotid	20	17.7	0.283 → 0.062	2.808 → 12.896	51	L Int. Iliac	5	0.285	5.314
Aortic Arch B	21	3.9	3.597	0.302	52	L Femoral	44.3	0.211 → 0.113	4.486 → 8.335
L Carotid	22	20.8	0.430	1.385	53	L Deep Femoral	7.3	0.091 → 0.049	19.574 → 36.373
L Int. Carotid	23	17.6	0.283 → 0.062	3.009 → 13.817	54	L Post. Tibial	21	0.126 → 0.062	13.541 → 27.243
L Ext. Carotid	24	17.7	0.283 → 0.062	2.808 → 12.896	55	L Ant. Tibial	16	0.053	27.775
Thor. Aorta A	25	5.2	3.135	0.332	56	R Ext. Iliac	14.5	0.322 → 0.229	3.115 → 4.375
L Subclavian A	26	3.4	0.562	1.110	57	R Int. Iliac	5	0.285	5.314
L Vertebral	27	14.8	0.111 → 0.105	7.662 → 8.087	58	R Femoral	44.4	0.211 → 0.113	4.486 → 8.335
L Subclavian B	28	42.2	0.510 → 0.175	1.862 → 7.239	59	R Deep Femoral	12.7	0.091 → 0.049	19.574 → 36.373
L Radius A	29	37.5	0.053 → 0.036	22.968 → 33.698	60	R Post. Tibial	32.2	0.126 → 0.062	13.541 → 27.243
L Ulnar A	30	6.7	0.145	8.983	61	R Ant. Tibial	40.9	0.053	27.775
L Interosseous	31	57.8	0.020	59.240					
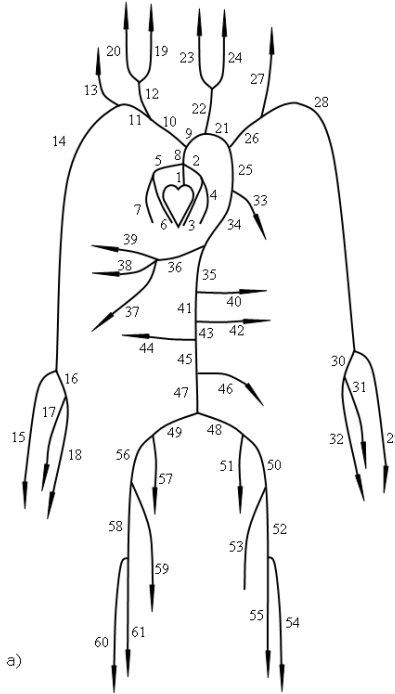
Figure 1.4: A typical arterial tree[7].

where h is the wall thickness, E is the Young's modulus, A_o is the cross sectional area when transmural pressure is zero (no difference between the external pressure and pressure inside), and σ is the Poisson's ratio.

1.3　Human Respiratory System

Human respiratory system can broadly be divided into human upper and lower airways (see Figure 1.5). Upper part includes the nose, *larynx* and part of *trachea*(see Figure 1.6). Lower part consists of part of trachea and lung. The lung is divided into *conducting, transition* and *respiratory* zones (see Figure 1.7). Each and every part of the airway plays an important role.

1.3.1　Upper Airway

Figure 1.5 shows a diagram of a vertical cross section (sagittal) of a typical human upper airway. It is usually divided into anatomically distinct sections, based on anatomical, physiological or pathological considerations. Here the upper airway is divided into six segments: the nasal cavities, nasopharynx (including the inferior portion or velopharynx), oropharynx, laryngopharynx, larynx and trachea[13]. The nasal cavities extend from the external nares (nostrils) to the posterior choanae, where the two cavities open into the nasopharynx. The lower part of the nasopharynx (velopharynx) lies behind the soft palate and is highly flexible and constantly changes in shape. It is a common site of snoring. The oropharynx extends from soft palate to the level of the tongue base and the laryngopharynx from tongue base to larynx. The larynx is a valve separating the
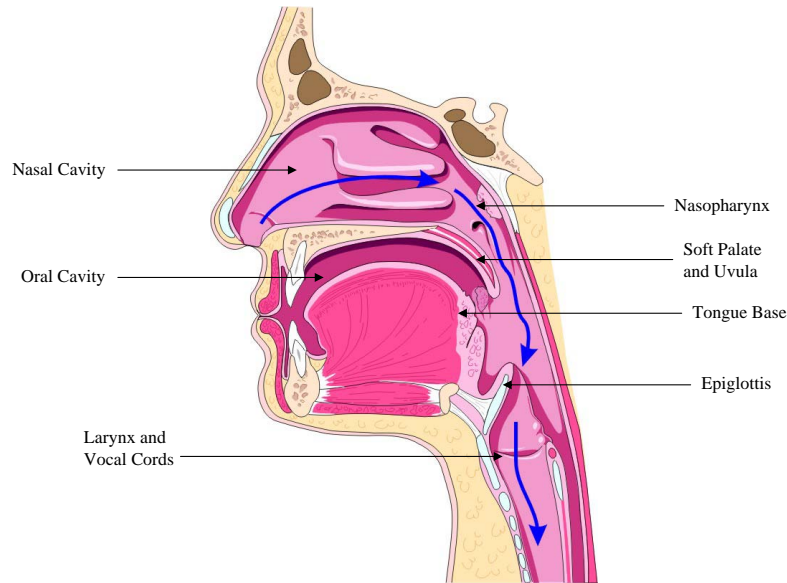
Figure 1.5: A typical human upper airway.[12].

pharynx and the trachea. The trachea (windpipe) extends from the larynx into the chest and lungs.

The walls of the upper airway are formed mostly of soft tissues, including over 20 muscle groups, adipose tissue (fat), tonsil tissue and a flexible mucosal lining. The muscles actively constrict and dilate the lumen of the upper airway[14, 15, 16]. In the nasal cavities, larynx and trachea, the walls also contain more rigid cartilaginous and bony structures. A large number and wide range of cross sectional measurements of the airway have been made[13]. The minimum airway size in the awake state occurs at one of three levels: the anterior nares (nasal valve), the velopharynx (behind the soft palate) and at the junction of larynx and trachea (the subglottis)[17, 18, 19]. During sleep the two narrowest portions are at the velopharynx and in the oropharynx at tongue base level. These two sites are of great interest as likely areas of soft tissue collapse of the airway, causing snoring and, most importantly, obstructive sleep apnoea. The posterior and lateral walls contain the superior, middle and inferior constrictor muscles, while the anterior wall comprises soft palate and tongue base. The laryngeal and tracheal parts of the airway are much less variable during sleep. However, in the awake state there are significant changes in glottic (laryngeal) area. During quiet breathing the vocal cords open during inspiration, to widen the airway, and close a little during expiration. During phonation the vocal cords are closely approximated with near complete closure of the airway.

1.3.2 Lower Airway

The two cone-shaped lungs present in human beings are located in the pleural cavities of the thorax on either side of the heart as shown in Figure 1.6. The lungs normally have clear anatomical divisions known as lobes. The right lung is divided into three lobes viz., superior, middle and inferior lobes, by the oblique and horizontal fissures. While the left lung, which is slightly smaller,
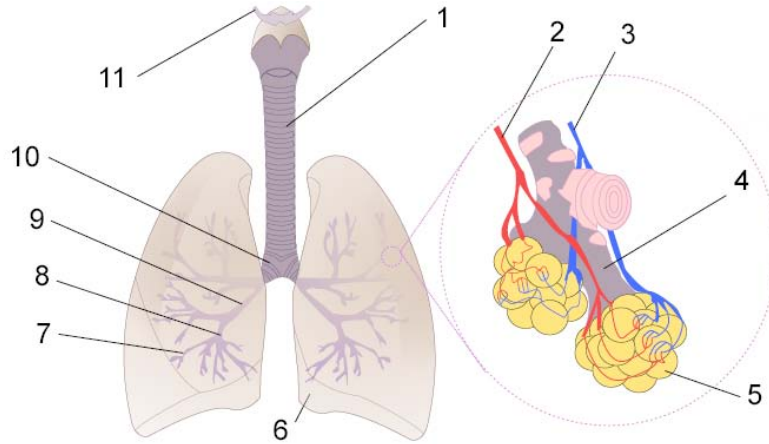
Figure 1.6: A typical human lower airway. 1:Trachea 2:Pulmonary artery 3:Pulmonary vein 4:Alveolar duct 5:Alveoli 6:Cardiac notch 7:Bronchioles 8:Tertiary bronchi 9:Secondary bronchi 10:Primary bronchi 11:Larynx [4].

is divided into two lobes viz., superior and inferior lobes, by the oblique fissure.

The trachea or the wind pipe leads the inhaled air from the larynx, into the conducting airways of the lungs which begin with the bifurcating bronchi. The first generation (or primary) of the bronchus leads the air into each of the lungs where they subdivide into secondary bronchi. The second generation (or secondary) bronchus leads into each of the lobes within which they subdivide into tertiary bronchus. These tertiary bronchi serve into each of the pyramid-shaped bronchopulmonary segments which are separated from one another by connective tissue septa. Each of these segment is served by its own artery and vein are clinically important because pulmonary disease is often confined to one or a few segments and these can be surgically removed without affecting the function of the other segments. Within these segments the tertiary bronchi further subdivide in several generations of numerous smaller bronchioles. These conducting airways lead into the respiratory zone of the lungs comprising of respiratory bronchioles, alveolar ducts and alveoli. The thin-walled sacs called alveoli are the respiratory surfaces of the lung. The alveolar ducts lead into a terminal bunch or into the alveolar sacs formed by a cluster of alveoli(see Figure 1.6, right).

Weibel[20] has observed 23 generations of conducting, transition and respiratory airway zones ranging from the trachea until the terminal bronchioles in normal human respiratory system as shown in Figure1.7. Approximately between 400 and 500 million alveolar sacs are present in a human lung achieving an enormous surface area for gas exchange of 50-140 square metres (≈ 75 times the body's external surface area). Pulmonary circulation dictates the deoxygenated blood flow between the right heart and the lungs. The pulmonary artery divides in stages to first form the right and left pulmonary arteries (see Figure 1.2) and then into the lobar arteries and finally into the finer pulmonary capillaries which surround the alveolar surface. The oxygenated blood is then collected by the four pulmonary vein, which then serve the left heart completing the circuit of pulmonary circulation.

Figure 1.7: Lung geometry[20].

1.4 Cardiovascular Diseases

Cardiovascular diseases refer to the class of diseases that involve the heart or blood vessels (arteries and veins)[21].

1.4.1 Aneurysms

An aneurysm is a localized, blood-filled dilation of a blood vessel caused by disease or weakening of the vessel wall. Most common areas prone to aneurysms in arteries are at the base of the brain (the circle of Willis) and in the aorta (the main artery coming out of the heart). The aneurysms of brain are referred to as cerebral aneurysms. The aortic aneurysms can be classified based on the locations. One common form of thoracic (aortic) aneurysm involves widening of the proximal aorta and the aortic root. The aneurysms at the distal part of the aorta are known as abdominal aortic aneurysms (AAA). Aneurysms occur in the legs also, particularly in the deep vessels such as the popliteal vessels in the knee.

The bulge in a blood vessel can burst and lead to death at any time. The larger an aneurysm becomes, the more likely it is to burst. Since aneurysms have a natural tendency to grow, given enough time they will inevitably reach the bursting point if undetected.

1.4.2 Angina

Angina pectoris, commonly known as angina, is severe chest pain due to ischemia (lack of blood and hence oxygen supply) of the heart muscle. This happens generally due to obstruction or spasm

of the coronary arteries that supply blood to heart walls. Coronary artery disease, the main cause of angina, is due to atherosclerosis of the cardiac arteries.

1.4.3 Atherosclerosis

Atherosclerosis is a disease affecting arterial blood vessels. It is a chronic inflammatory response in the walls of arteries, in large part due to the accumulation of macrophage white blood cells and promoted by low density (especially small particle) lipoproteins (plasma proteins that carry cholesterol and triglycerides) without adequate removal of fats and cholesterol from the macrophages by functional high density lipoproteins (HDL). It is commonly referred to as a "hardening" or "furring" of the arteries. It is caused by the formation of multiple plaques within the arteries.

These complications are chronic, slowly progressing and cumulative. Most commonly, soft plaque suddenly ruptures, causing the formation of a thrombus that will rapidly slow or stop blood flow, leading to death of the tissues fed by the artery in approximately 5 minutes. This catastrophic event is called an infarction. One of the most common recognized scenarios is called coronary thrombosis of a coronary artery, causing myocardial infarction (a heart attack). Another common scenario in very advanced disease is claudication from insufficient blood supply to the legs, typically due to a combination of both stenosis and aneurysmal segments narrowed with clots. Since atherosclerosis is a body-wide process, similar events occur also in the arteries to the brain, intestines, kidneys, legs, etc.

1.4.4 Stroke

A stroke is the rapidly developing loss of brain functions due to a disturbance in the blood vessels supplying blood to the brain. This can be due to ischemia (lack of blood supply) caused by thrombosis or embolism or due to a hemorrhage. As a result, the affected area of the brain is unable to function, leading to inability to move one or more limbs on one side of the body, inability to understand or formulate speech or inability to see one side of the visual field. In the past, stroke was referred to as cerebrovascular accident or CVA, but the term "stroke" is now preferred.

1.4.5 Cerebrovascular disease

Cerebrovascular disease is a group of brain dysfunctions related to disease of blood vessels supplying the brain. Hypertension is the most important cause that damages the blood vessel lining endothelium exposing the underlying collagen where platelets aggregate to initiate a repairing process which is not always complete and perfect. Sustained hypertension permanently changes the architecture of the blood vessels making them narrow, stiff, deformed and uneven which are more vulnerable to fluctuations of blood pressure. A fall in blood pressure during sleep can lead to marked reduction in blood flow in the narrowed blood vessels causing ischemic stroke in the morning whereas a sudden rise in blood pressure can cause tearing of the blood vessels causing intracranial hemorrhage during excitation at daytime. Primarily people who are elderly, diabetic, smoker, or have ischemic heart disease, have cerebrovascular disease. All diseases related to artery dysfunction can be classified under a disease as known as *Macrovascular disease*. This is a simplistic study by which arteries are blocked by fatty deposits or by a blood clot. The results of

cerebrovascular disease can include a stroke, or even sometimes a hemorrhagic stroke. Ischemia or other blood vessel dysfunctions can affect one during a cerebrovascular accident.

1.4.6   Heart failure

Heart failure is a cardiac condition that occurs when a problem with the structure or function of the heart impairs its ability to supply sufficient blood flow to meet the body's needs.

1.4.7   Coronary disease

Coronary disease (or coronary heart disease) refers to the failure of coronary circulation to supply adequate circulation to cardiac muscle and surrounding tissue.

1.4.8   Myocardial infarction

Myocardial infarction (MI or AMI for acute myocardial infarction), also known as a heart attack, occurs when the blood supply to part of the heart is interrupted. This is most commonly due to occlusion (blockage) of a coronary artery following the rupture of a vulnerable atherosclerotic plaque, which is an unstable collection of lipids (like cholesterol) and white blood cells (especially macrophages) in the wall of an artery. The resulting ischemia (restriction in blood supply) and oxygen shortage, if left untreated for a sufficient period, can cause damage and/or death (infarction) of heart muscle tissue (myocardium).

1.5   Respiratory Diseases

Respiratory disease is the term for diseases of the respiratory system. These include diseases of the lung, pleural cavity, bronchial tubes, trachea, upper respiratory tract and of the nerves and muscles of breathing. Respiratory diseases range from mild and self-limiting such as the common cold to life-threatening such as bacterial pneumonia or pulmonary embolism. They are a common and important cause of illness and death. In the US, people suffer 1 billion colds per year. One in seven people in the UK is affected by some form of chronic lung disease, most commonly chronic obstructive pulmonary disease (COPDD) and asthma. Respiratory disease is responsible for over 10% of hospitalizations and over 16% of deaths in Canada. The study of respiratory disease is known as *pulmonology*. A doctor who specializes in respiratory disease is known as a pulmonologist, a chest medicine specialist, a respiratory medicine specialist, a respirologist or a thoracic medicine specialist.

1.5.1   Chronic obstructive pulmonary disease

Chronic obstructive pulmonary disease (COPD), also known as chronic obstructive airways disease (COAD) or chronic airflow limitation (CAL), is a group of illnesses characterised by airflow limitation that is not fully reversible. The flow of air into and out of the lungs is impaired. This can be measured with breathing devices such as a peak flow meter or by spirometry. The term COPD includes the conditions emphysema and chronic bronchitis although most patients with

COPD have characteristics of both conditions to varying degrees. Asthma being a reversible obstruction of airways is often considered separately, but many COPD patients also have some degree of reversibility in their airways.

The most common cause of COPD is cigarette smoking. COPD is a gradually progressive condition and usually only develops after about 20 pack-years of smoking. COPD may also be caused by breathing in other particles and gasses.The diagnosis of COPD is established through spirometry although other pulmonary function tests can be helpful. A chest x-ray is often ordered to look for hyperinflation and rule out other lung conditions but the lung damage of COPD is not always visible on a chest x-ray. Emphysema, for example can only be seen on CT scan.

1.5.2   Asthma

Asthma is an obstructive lung disease where the bronchial tubes (airways) are extra sensitive (hyperresponsive). The airways become inflamed and produce excess mucus and the muscles around the airways tighten making the airways narrower. Asthma is usually triggered by breathing in things in the air such as dust or pollen that produce an allergic reaction. It may be triggered by other things such as an upper respiratory tract infection, cold air, exercise or smoke. Asthma is a common condition and affects over 300 million people around the world. Asthma causes recurring episodes of wheezing, breathlessness, chest tightness, and coughing, particularly at night or in the early morning.

1.5.3   Cystic fibrosis

Cystic fibrosis is an inherited disorder of the CFTR gene, a chloride ion channel. The lack of this channel causes reduced water content of secretions. This affects the mucus secreted as part of the lung's defence and creates sticky, viscous mucus. This makes the lungs more susceptible to infection, inflammation and mucous plugging.

1.5.4   Bronchiolitis

In many parts of the world, the most common cause of obstructive lung disease is lung scarring after tuberculosis infection.

1.5.5   Restrictive lung diseases

Restrictive lung diseases (also known as interstitial lung diseases) are characterised by a loss of lung compliance, causing incomplete lung expansion and increased lung stiffness. The underlying process is usually pulmonary fibrosis (scarring of the lung). As the disease progresses, the normal lung tissue is gradually replaced by scar tissue interspersed with pockets of air. This can lead to parts of the lung having a honeycomb-like appearance.

Restrictive lung diseases may be due to a specific cause such as:

Asbestosis caused by long-term exposure to asbestos dust. Radiation fibrosis, usually from the radiation given for cancer treatment. Certain drugs such as amiodarone, bleomycin and methotrexate. As a consequence of another disease such as rheumatoid arthritis. Hypersensitivity pneumonitis due to an allergic reaction to inhaled particles. Acute respiratory distress syndrome (ARDS),

a severe lung condition occurring in response to a critical illness or injury. Infant respiratory distress syndrome due to a deficiency of surfactant in the lungs of a baby born prematurely. Many cases of restrictive lung disease are idiopathic (have no known cause). Examples are: Idiopathic pulmonary fibrosis, Idiopathic interstitial pneumonia, of which there are several types, Sarcoidosis Eosinophilic pneumonia, Lymphangioleiomyomatosis, Pulmonary Langerhans cell histiocytosis Pulmonary alveolar proteinosis

1.5.6   Respiratory tract infections

Infections can affect any part of the respiratory system. They are traditionally divided into upper respiratory tract infections and lower respiratory tract infections.

Upper respiratory tract infection

The most common upper respiratory tract infection is the common cold however infections of specific organs of the upper respiratory tract such as sinusitis, tonsillitis, otitis media, pharyngitis and laryngitis are also considered upper respiratory tract infections.

Lower respiratory tract infection

The most common lower respiratory tract infection in is pneumonia, a lung infection. Pneumonia is usually caused by bacteria, particularly [Streptococcus pneumoniae] in Western countries. Worldwide, tuberculosis is an important cause of pneumonia. Other pathogens such as viruses and fungi can cause pneumonia for example severe acute respiratory syndrome and pneumocystis pneumonia. A pneumonia may develop complications such as a lung abscess, a round cavity in the lung caused by the infection or an empyema, the spread of the infection to the pleural cavity.

1.5.7   Respiratory tumours

Tumours of the respiratory system are either malignant or benign.

Malignant tumours

Malignant tumours, or cancers of the respiratory system, particularly lung cancers, are a major health problem responsible for 15% of all cancer diagnoses and 29% of all cancer deaths. The majority of respiratory system cancers are attributable to smoking tobacco.

The major types of respiratory system cancer are: Small cell lung cancer, Non-small cell lung cancer, Adenocarcinoma, Squamous cell carcinoma, Large cell undifferentiated carcinoma, Other lung cancers (carcinoid, Kaposis sarcoma, melanoma), Lymphoma, Head and neck cancer, Mesothelioma, usually caused by exposure to asbestos dust.

In addition, since many cancers spread via the bloodstream and the entire cardiac output passes through the lungs, it is common for cancer metastases to occur in the lung. Breast cancer may invade directly through local spread, and through lymph node metastases. After metastasis to the liver, colon cancer frequently metastasizes to the lung. Prostate cancer, germ cell cancer and renal cell carcinoma may also metastasize to the lung.

Treatment of respiratory system cancer depends on the type of cancer. Surgery (usually removal of part of the lung, a lobectomy or an entire lung, a pneumonectomy), chemotherapy and radiotherapy are all used. The chance of surviving lung cancer depends on the cancer stage at the time the cancer is diagnosed and is only about 14-17% overall. In the case of metastases to the lung, treatment can occasionally be curative but only in certain, rare circumstances.

Benign tumours

Benign tumours are relatively rare causes of respiratory disease. Examples of benign tumours are: Pulmonary hamartoma: Congenital malformations such as pulmonary sequestration and congenital cystic adenomatoid malformation (CCAM).

1.5.8   Pleural cavity diseases

Pleural cavity diseases include empyema and mesothelioma which are mentioned above.

A collection of fluid in the pleural cavity is known as a pleural effusion. This may be due to fluid shifting from the bloodstream into the pleural cavity due to conditions such as congestive heart failure and cirrhosis. It may also be due to inflammation of the pleura itself as can occur with infection, pulmonary embolus, tuberculosis, mesothelioma and other conditions.

A pneumothorax is a hole in the pleura covering the lung allowing air in the lung to escape into the pleural cavity. The affected lung collapses like a deflated balloon. A tension pneumothorax is a particularly severe form of this condition where the air in the pleural cavity cannot escape, so the pneumothorax keeps getting bigger until it compresses the heart and blood vessels, leading to a life threatening situation.

1.5.9   Pulmonary vascular diseases

Pulmonary vascular diseases are conditions that affect the pulmonary circulation (see also Section 1.4). Examples of these conditions are:

Pulmonary embolism, a blood clot that forms in a vein, breaks free, travels through the heart and lodges in the lungs (thromboembolism). Large pulmonary emboli are fatal, causing sudden death. A number of other substances can also embolise to the lungs but they are much more rare: fat embolism (particularly after bony injury), amniotic fluid embolism (with complications of labour and delivery), air embolism (iatrogenic).

Pulmonary arterial hypertension, elevated pressure in the pulmonary arteries. It can be idiopathic or due to the effects of another disease, particularly COPD. This can lead to strain on the right side of the heart, a condition known as cor pulmonale.

Pulmonary edema, leakage of fluid from capillaries of the lung into the alveoli (or air spaces). It is usually due to congestive heart failure.

Pulmonary hemorrhage, inflammation and damage to capillaries in the lung resulting in blood leaking into the alveoli. This may cause blood to be coughed up. Pulmonary hemorrhage can be due to auto-immune disorders such as Wegener's Granulomatosis and Goodpasture's syndrome.

1.5.10 Disorders of breathing mechanics

The brain co-ordinates breathing and sends messages via nerves to the muscles of respiration. The muscles produce the movements of breathing. Disorders of the brains control of breathing, the nerves or the muscles of respiration can affect the respiratory system. Common disorders of breathing mechanics are:

Obstructive sleep apnea; Central sleep apnea; Amyotrophic lateral sclerosis; Guillan-Barre syndrome; Myasthenia gravis

Obesity is often associated with sleep apnea and can cause either an obstructive or a restrictive pattern on spirometry. Obesity reduces the movement of the chest wall which can, in extreme cases, result in the obesity-hypoventilation syndrome, a cause of respiratory failure.

1.6 Summary

This chapter is designed to introduce the topic of biofluid dynamics and its importance with respect to solving problems of cardiovascular and respiratory systems. In addition to outlining the importance of the topic, this chapter also provided the reader with anatomy and physiology of both cardiovascular and respiratory systems. A detailed description of various cardiovascular and respiratory diseases is also provided. Those who seek further details on the topic are referred to the references list provided below.

Bibliography

[1] C. Kleinstreuer. *Biofluid Dynamics. Principles and Selected Applications.* Taylor & Francis, Boca Raton, 2006.

[2] http://www.daviddarling.info/encyclopedia/C/circulatory_system.html, 2008.

[3] A. Despopoulos and S. Silbernagl. *Color Atlas of Physiology.* Georg Thieme Verlag, New York, 1986.

[4] Wikipedia. 2008.

[5] A. Howell. *What is systole?* http://drhowellnet.blogspot.com/2007/07/what-is-systole.html.

[6] http://commons.wikimedia.org. 2008.

[7] J.P. Mynard and P. Nithiarasu. A 1d arterial blood flow model incorporating ventricular pressure, aortic valve and regional coronary flow using the locally conservative galerkin (lcg) method. *Communications in Numerical Methods in Engineering*, 24:367–417, 2008.

[8] J.J. Wang and K.H. Parker. Wave propagation in a model of the arterial circulation. *Journal of Biomechanics*, 37(4):457–470, 2004.

[9] N. Stergiopulos, D.F. Young, and T.R. Rogge. Computer simulation of arterial flow with applications to arterial and aortic stenoses. *Journal of Biomechanics*, 25(12):1477–1488, 1992.

[10] A. Avolio. Multi-branched model of the human arterial system. *Medical and Biological Engineering and Computing*, 18(6):709–718, 1980.

[11] N. Westerhof, F. Bosman, C.J. De Vries, and A. Noordergraaf. Analog studies of the human systemic arterial tree. *Journal of Biomechanics*, 2(2):121–134, 1969.

[12] P. Nithiarasu, O. Hassan, K. Morgan, N.P. Weatherill, C. Fielder, H. Whittet, P. Ebden, and K.R. Lewis. Steady flow through a realistic human upper airway geometry. *International Journal for Numerical Methods in Fluids*, 57:631–651, 2008.

[13] I. Ayappa and D.M. Rapoport. The upper airway in sleep: Physiology of the pharynx. *Physiological Review*, 7:9–33, 2003.

[14] T. Nishino and K. Hiraga. Coordination of swallowing and respiration in unconscious subjects. *Journal of Applied Phsiology*, 70:988–993, 1991.

[15] J.M. Fouke, J.P. Teeter, and K.P. Strohl. Pressure-volume behaviour of the upper airway. *Journal of Applied Phsiology*, 61:912–918, 1986.

[16] K.P. Strohl and J.M. Fouke. Dialating forces on the upper airway of anethetized dogs. *Journal of Applied Phsiology*, 58:452–458, 1985.

[17] A. Verneuil, D.A. Berry, J. Kreiman, B.R. Gerratt, M. Ye, and G.S. Berke. Modelling measured glottal volume velocity waveforms. *Annals of Otology Rhinology and Laryngology*, 112:120–131, 2003.

[18] T. Brancatisano, P. Collett, and L. Engel. Respiratory movements of the vocal cords. *Journal of Applied Phsiology*, 54:1269–1276, 1983.

[19] C. Renotte, V. Bouffioux, and F. Wilquem. Numerical 3d analysis of oscillatory flow in the time-varying laryngeal channel. *Journal of Biomechanics*, 33:1637–1644, 2000.

[20] E.R. Weibel. Morphometry of the human lung. *Science*, pages 115–126, 1963.

[21] A. Maton. *Human Biology and Health.* Prentice Hall, Englewood Cliffs,New Jersey, 1993.

Chapter 2

Biofluids, Blood Vessels and Respiratory System Walls

2.1   Introduction

The fluids associated with a human body includes air, O_2, CO_2, water, solvents, solutions, suspensions, serum, lymph and blood. This chapter gives importance to the major body fluid, blood. This is mainly due to the fact that the blood is an extremely complex fluid. It consists of blood cells suspended in plasma. Since blood flow in arteries and veins are closely linked to the blood vessel properties, morphology of blood vessels will also be discussed in this chapter. The mechanical properties of respiratory system walls will also be discussed briefly. Before studying about the blood vessels and the airway geometry properties, properties of blood is discussed in some detail first.

The major roles of the blood include[1]:

- Carries oxygen and nutrients to active tissues

- Delivers carbon dioxide to the lungs

- Brings metabolic end products to kidneys

- Blood is a buffering reservoir that controls pH of biofluids

- Plays a major role in the body's immune system

- In addition to mass, it also transports heat

In order to study the blood flow, it is essential to learn more about its composition.

2.2   Blood Components

2.2.1   Blood Plasma

Blood plasma is the liquid component of blood, in which the blood cells are suspended. It makes up about 55% of total blood volume. It is composed of mostly water, and contains dissolved

proteins, glucose, clotting factors, mineral ions, hormones and carbon dioxide. All the major components of blood plasma are listed in Table 2.1. In addition to the components listed in this table, plasma also contains small quantities of gases, carbon dioxide (2ml/100 ml), oxygen (0.2ml/100 ml) and nitrogen (0.9ml/100 ml); traces of nutrients such as amino acids (40mg/100 ml) and vitamins (0.0001-2.5mg/ 100 ml). In addition, traces of waste products such as urea (34mg/100 ml), creatinite (1mg/100 ml), uric acid (5mg/100 ml) and bilirubin (0.2-1.2mg/ 100ml) are also found in plasma[2].

Table 2.1: Composition of blood plasma

Component	Percentage/Concentration	Functions
1. Water	93%	Carrying medium
2. Proteins	6-8%	buffer; binding agent; antibodies Clotting factor; enzymes; non-penetrating solute
2.1 Albumin	3.3 - 4.0 g/100 ml	
2.2 Globulins	$\approx$ 4.5 g/100 ml	
2.3 Fibrinogen	0.34-0.43 g/100 ml	
3. Inorganic components	0.8%	
3.1 Sodium	0.31-0.34 g/100 ml	
3.2 Potassium	0.016-0.021 g/100 ml	
3.3 Calcium	0.009-0.011 g/100 ml	
3.4 Magnesium	0.002-0.003 g/100 ml	
3.5 Chloride	0.36-0.39 g/100 ml	
3.6 Bicarbonate	0.20-0.24 g/100 ml	
3.7 Phosphate	0.003-0.004 g/100 ml	
4. Lipids	0.6%	
5. Glucose	0.1%	

The density of the plasma is approximately 1030 kg/m^3. With natural proteins the plasma behaves like a Newtonian fluid with a viscosity of 1.2×10^{-3} Pa.s. The inorganic components in the plasma generate an osmotic pressure of about 8×10^5 Pa.

2.2.2   Blood Cells

Blood cells are normally divided into three components, red cells (*erythrocytes*), white cells (*leukocytes*) and *platelets*. The white cells and platelets play the respective role of immune response and blood clotting. However, the number of white blood cells and platelets are relatively small compared to the number of red blood cells.

Erythrocytes

As shown in Table 2.2, erythrocytes volume concentration in blood is about 45%. This concentration is often referred to as haematocrite (ratio between the volume of red blood cells to the total

Table 2.2: Blood cells

Cell	Volume in blood, %	Number per mm^3	Unstressed shape and size, (μm)
Erythrocytes	45	4-6×10^6	Biconcave disc, 8 × 1-3
Leucocytes		4-11×10^3	Roughly sphereical, 7-22
Platelets	1	2.5-5×10^5	rounded or oval, 2-4

blood volume). The shape of the red blood cell is shown in Figure 2.1. As shown the shape of an erythrocyte is biconcave discoid. The diameter of the disc is about 7μm and the thickness varies between 1 and 3 μm. The density of red blood cells is 1.08×10^3. The membrane on the outer of a red blood cell is covered with albumin at outside and another protein, spectrin, inside. The spectrin layer is a skeletal protein and supports the lipid layer. The liquid interior is a saturated solution of haemoglobin with a dynamic viscosity of $6\times10-3$ Pa.s. Haemoglobin binds oxygen and carbon dioxide. The biconcave shape makes the erythrocytes flexible to squeeze through small capillaries below 8μm size. The erythrocytes aggregate face to face if they are brought in contact with each other at low shear rates. Such aggregates are referred to as *rouleaux*. The secondary aggregation of the rouleaux leading to a rouleaux network happens at nearly zero shear rates.

(a) Group   (b) Single
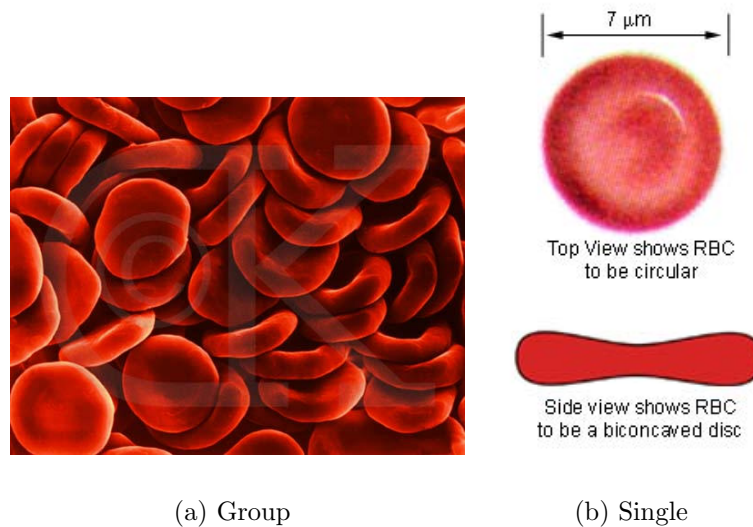
Figure 2.1: Red blood cells (erythrocytes)

Leucocytes

They are very small numbers compared ro red blood cells. Thus, they have a very small influence on on the rheological properties of blood.

Platelets

The volume concentration of platelets is about 0.3%. They are more rigid than red blood cells and responsible for blood clots. If the platelets are in contact with adenosine diphosphate (ADP) they aggregate and thrombus forms.

2.3   Blood Rheology

Blood is a non-Newtonian fluid. However, often the non-Newtonian effect is very small due to various reasons. Thus, it is important to know about the blood rheology. Rheology explains how a material deform/flow in response to applied forces.

(a) Viscosity   (b) Relative viscosity
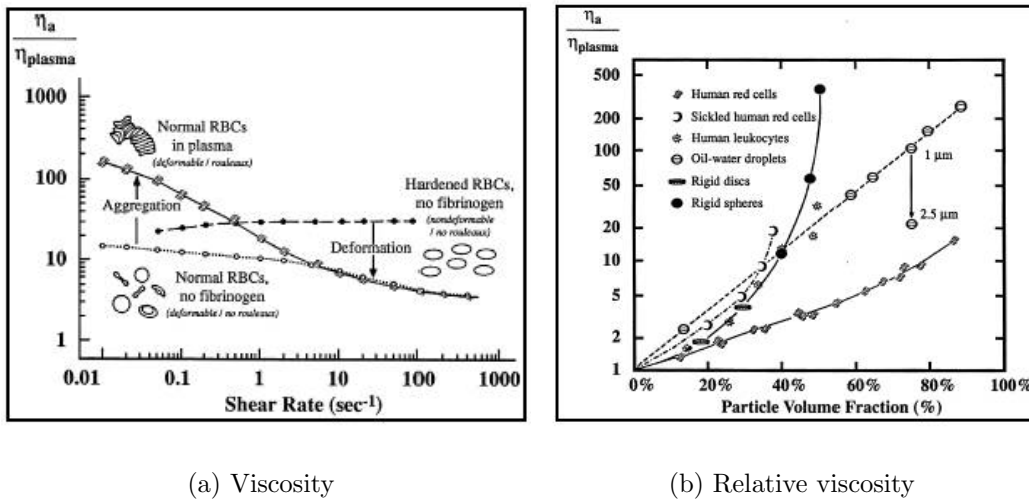
Figure 2.2: Human blood viscosity variation with respect to shear rate and particle volume fraction[3].

As mentioned previously, if the blood is stationary for several seconds, rouleaux begin to form. As a result the effective viscosity of the blood increases. When stationary state is disturbed with increasing shear rate, the rouleaux formation is destroyed and the viscosity decreases. The red blood cells in the body are often influenced by two mechanisms. First one is the random *Brownian motion* attempting to create a random aggregation of red blood cells. The second mechanism in which the flow attempts to orient the red blood cells in the streamline direction with the highest axis aligned with the streamline direction. The former mechanism increases the effective viscosity, while the latter one decreases the viscosity. From these physics, it is clear that blood is a shear thinning fluid, i.e., viscosity decreases with increase in shear rate.

Figure 2.2(a) shows the variation of human blood viscosity ratio (ratio between blood viscosity and plasma viscosity) variation with respect to shear rate. As seen, beyond a shear rate of about 100s^{-1}, the viscosity is nearly constant and the blood behaves like a Newtonian fluid and the Newtonian relation for shear stress,

$$\tau = \mu \dot{\gamma} \tag{2.1}$$

is sufficient to describe the behaviour. In the above equation, τ is the shear stress, μ is the dynamic viscosity and $\dot{\gamma}$ is the shear rate. However, below a shear rate of 100s^{-1} the above relationship is not valid. At lower shear rates the expression,

$$\tau = \mu_e \dot{\gamma} \tag{2.2}$$

may be used to describe the blood. Here μ_e is the effective dynamic viscosity. Strictly speaking the effective viscosity of blood not only depends on the shear rate but also on the history of shear rate. This makes the blood a viscoelastic material, i.e., viscous and elastic.

Figure 2.2(b) shows the viscosity variation with respect to particle volume fraction. As seen, for normal human blood, the viscosity reaches a valve between 3 to 4 times that of plasma when particle volume fraction reaches about 45% (actual hematocrit). The mort important point is that the normal blood flows much more easily compared to rigid particles, for the same particle volume fraction. This is due to the fact that the red blood cells can accommodate by deforming in order to pass by one another. It is also notable that the viscosity of blood with sickle cell anemia is very high for the same particle volume fraction ratio. The red blood cells of blood affected by sickle cell anemia is much less deformable than the normal blood cells.

2.4   Blood Constitutive Models

From the previous section it is obvious that the blood is a shear thinning fluid. Figure 2.3(a) shows the qualitative behaviour of a shear thinning fluid. As seen, a shear thinning plot is concave shape downwards. Although Figure 2.3(a) shows zero stress at zero shear rate, this is not true for blood. Blood behaves more like a shear thinning fluid in Figure 2.3(b). This graph shows a yield stress τ_o below which the blood behaves like a solid. Once this value is exceeded, blood starts flowing.

(a) Shear thinning behaviour   (b) Casson model
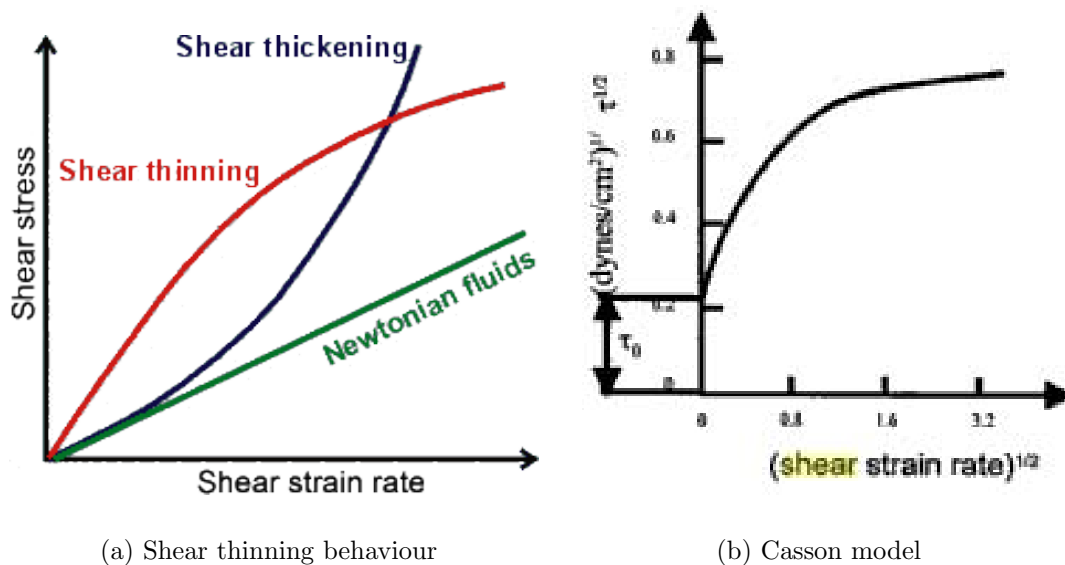
Figure 2.3: Shear thinning nature of blood and Casson model for blood[4].

The shear thinning behaviour shown in Figure 2.3(b) is often represented by the Casson model originally derived for printer's ink. Using Casson model, the blood shear stress is represented by

$$\sqrt{\tau} = \sqrt{\tau_o} + \sqrt{\mu\dot{\gamma}} \tag{2.3}$$

for $\tau \leq \tau_o$ and $\dot{\gamma} = 0$, $\tau < \tau_o$. It is easy to verify that when $\dot{\gamma} >> \tau_o/\mu$, the above equation approaches Newtonian equation, $\tau = \mu\dot{\gamma}$.

2.5   Other Biofluids

Lymph is the fluid that is formed as the interstitial fluid enters the lymph vessels by filtration. The lymph then travels to at least one lymph node before emptying ultimately into the right or the left subclavian vein, where it mixes back with blood.

Interstitial fluid (or tissue fluid) is a solution which bathes and surrounds the cells of multicellular animals. It is the main component of the extracellular fluid, which also includes plasma and transcellular fluid. On average, a person has about 11 litres (2.4 imperial gallons) of interstitial fluid providing the cells of the body with nutrients and a means of waste removal.

(a) Lymph capillary   (b) Interstitial fluid
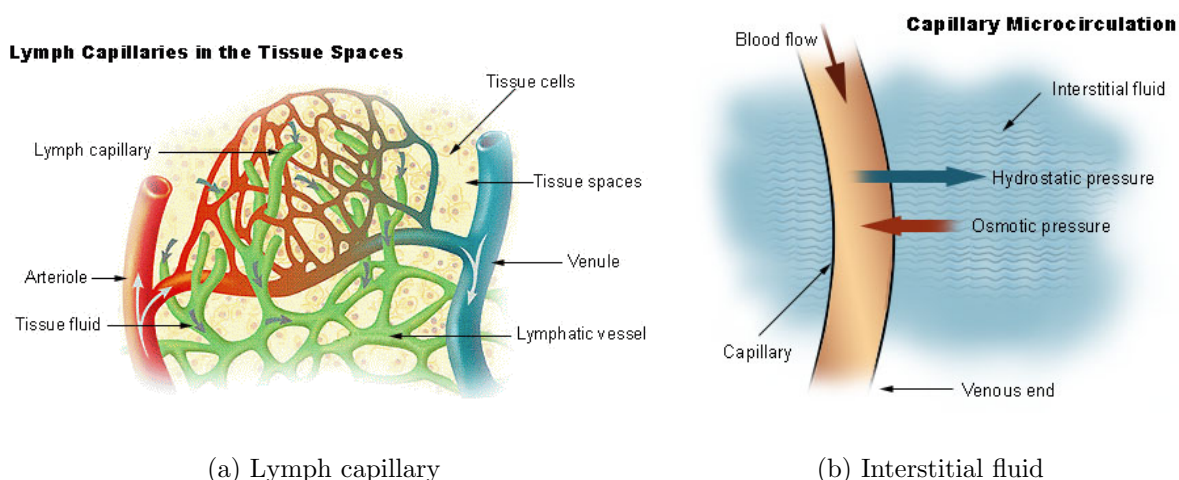
Figure 2.4: Human body micro circulation. Lymph system and tissue fluid[5].

In addition to these, properties of air are also important to study respiratory systems.

2.6   Blood Vessels

2.6.1   Morphology

The arterial wall consists of three layers. The inner layer is referred to as *tunica intima*, the outer layer is *tunica adventitia* and the middle layer is called *tunica media*. Figure 2.5 shows all the three layers in detail. The intima layer consists of endothelial cells and their basal lamina. The

endothelium is formed by a single layer of cells separated from media by thin elastic ring known as the internal elastic lamina(Figure 2.5). The outer layer, adventitia, is a loose connective tissue consists of type I collagen, nerves, fibroblasts, and some elastin fibers. The adventitia is responsible for connecting the artery to the surrounding tissues. The adventitia in some arteries contains a vascular network for supplying nutrients. The media consists of smooth muscle cells, types I,III, and V collagen and proteoglycans. This layer is the most important layer for determining the mechanical strength of an artery.

(a)

(b)
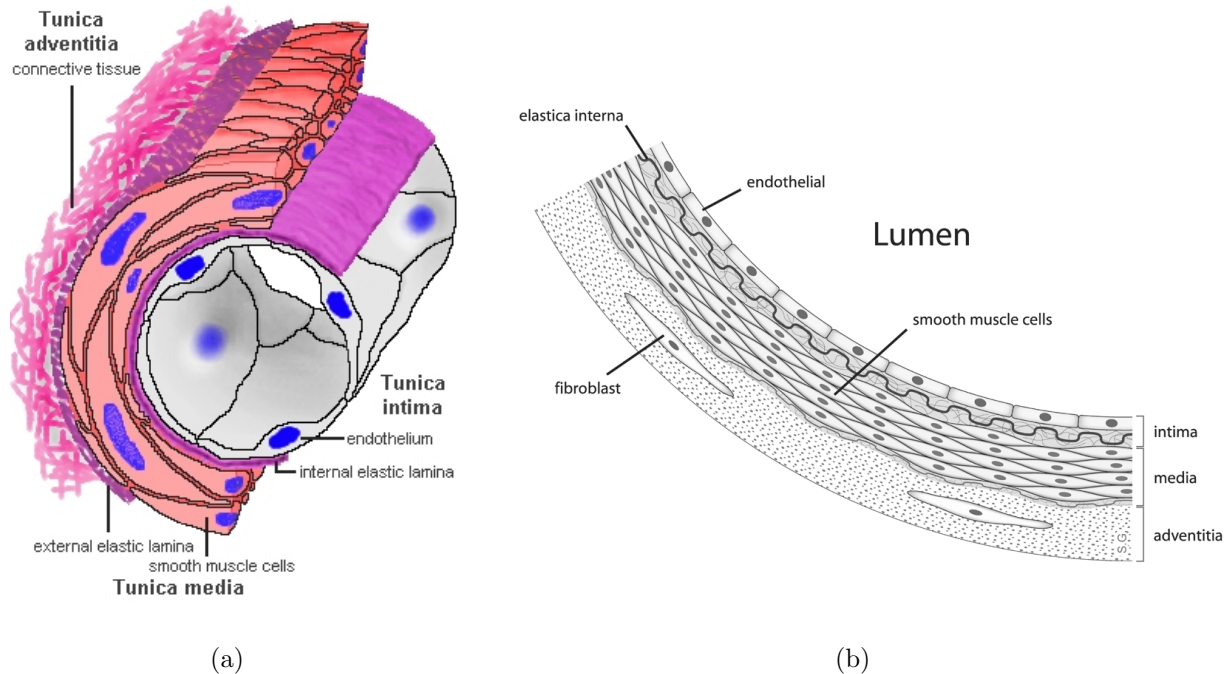
Figure 2.5: Typical structure of a blood vessel[5].

2.6.2 Properties

Figure 2.6 shows typical stress strain relationship for different solid materials. Both the linear and non-linear elastic materials follow the same path on unloading(Figures 2.6(a) and (b)). However, the viscoelastic material follows a different path during unloading as seen in Figure 2.6(c). Most of the biosolids belong to this last category and they are in general referred to as viscoelastic materials.

If stress in a material decreases with time when suddenly strained and maintained at a constant strain, the material is said to be under *stress relaxation* or *relaxation*. Some material continually deform with respect to time after suddenly stressed and maintained at constant stress. This phenomenon is known as *creep*. If a material gives a different stress-strain relationship during loading and unloading when subjected to cyclic loading, the behaviour is referred to as *hysteresis*(Figure 2.7). Collectively all such phenomena (relaxation, creep and hysteresis) are called *viscoelasticity*.

(a) Linear elastic   (b) Non-linear elastic   (c) Non-linear Viscoelastic
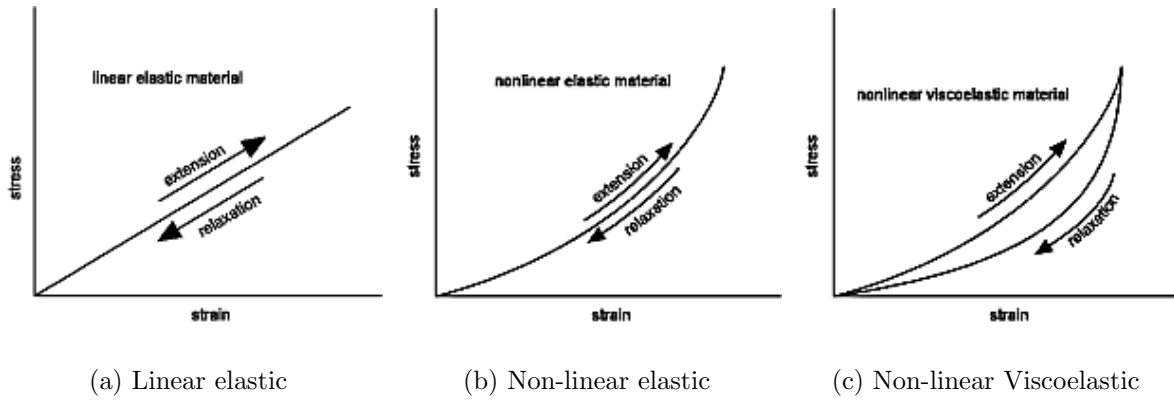
Figure 2.6: Stress-strain relationship for different kind of material.
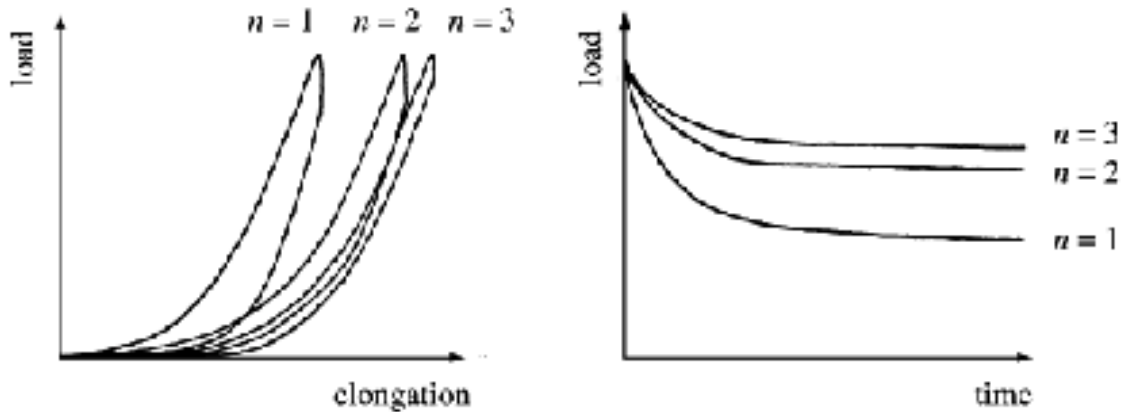
Figure 2.7: Load-elongation and relation curves of the first three cycles of a anterior cruciate ligament[6].

As seen in the previous section, three common constituents of blood vessel walls are elastin, collagen and smooth muscle. Elastin is the most linearly elastic biosolid material known[6]. Collagen is the main load carrying element in blood vessels, skin, tendons, cornea, sclera, bone, fascia, dura mater, the uterian cervix etc.[6]. Since collagen is the basic element, it winds itself together into fibrils and fibrils are organised into fibers and fibers form into various tissues.

Figure 2.7 shows the cyclic loading and unloading of a ligament. As seen the first three stress-strain relationships shift towards the right (Figure 2.7(left)). Figure 2.7(right) shows the first three relaxation curves. As seen the curves are moving upwards but the rate of upwards change is low as they go upwards. Eventually the curves stop changing for a given loading and unloading pattern and reach a *preconditioned* state[6].

Figure 2.8(a) shows composition of some selected arteries. As seen collagen, elastin and smooth muscle cells dominate the composition. Figure 2.8(b) shows a typical stress-strain relationship for aortic and carotid wall materials. It is once again important to note here that the vascular tissue is normally viscoelastic.

	Pulmonary artery	Thoracic aorta	Plantar artery
Media			
Smooth muscle	46.4 ± 7.7	33.5 ± 10.4	60.5 ± 6.5
Ground substance	17.2 ± 8.6	5.6 ± 6.7	26.4 ± 6.4
Elastin	9.0 ± 3.2	24.3 ± 7.7	1.3 ± 1.1
Collagen	27.4 ± 13.2	36.8 ± 10.2	11.9 ± 8.4
Adventitia			
Collagen	63.0 ± 8.5	77.7 ± 14.1	63.9 ± 9.7
Ground substance	25.1 ± 8.3	10.6 ± 10.4	24.7 ± 9.3
Fibroblasts	10.4 ± 6.1	9.4 ± 11.0	11.4 ± 2.6
Elastin	1.5 ± 1.5	2.4 ± 3.2	0
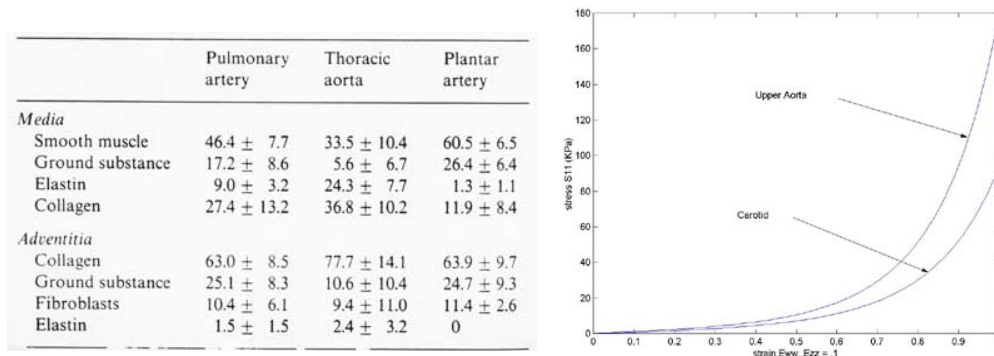
(a) Composition%[6] (b) Stress-strain relation[7]

Figure 2.8: Composition of different arteries and stress-strain relationship for aorta and carotid arteries.

2.7 Human Airway Walls

Human airway walls are much more complicated than arteries. As seen in the previous chapter, the upper airway consists of different types of muscles. Unlike blood vessels, it is extremely difficult to briefly define the upper airway properties due to the fact that the mechanical properties considerably differ between various sections of an airway. For example, the palate contains both soft and hard parts. Nose is generally a static structure. Tongue base is soft and the muscles along the pharynx varies in strength. Trachea consists partly of soft material strengthened by cartilages. The lung geometry below bifurcation normally contains elastin and collagen fibres.

2.7.1 Properties
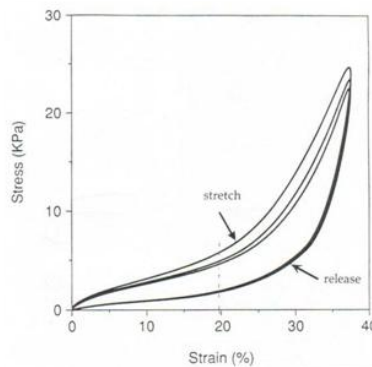
Figure 2.9: Stress-strain relationship for vocal-cord muscles[8].

Figure 2.9 shows the stress strain curve for a vocal-cord muscle. As seen the material clearly loses energy when unloaded from a stressed position. This clearly shows the viscoelastic behaviour

of this muscle. It is extremely difficult to find data in this area.

Lung tissue or parenchyma is naturally elastic due to high proportion of elastin. At low stresses, the collagen and elastin within the lung are randomly oriented. At high stresses they align along the direction of stretching. In addition to these load bearing elastin and collagen, surface tension also plays a major role in determining the strength of the lung geometries. The surface tension of the thin fluid section on the inner surface of alveolus tries to collapse the lung.

2.8   Summary

This chapter discussed the properties of natural biomaterials in general terms. It is clear that the blood is non-Newtonian fluid but shear thinning in nature. Thus, the non-Newtonian effect is negligibly small above a shear rate of about $100s^{-1}$. It was also very clear that majority of the living biosolids are viscoelastic in nature. In the following chapters, we will see more about the properties and constitutive modelling.

Bibliography

[1] C.R. Ethier and C.A. Simmons. *Introductory Biomechanics. From Cells to Organisms.* Cambridge University Press, 2007.

[2] A.J. Vander, J.H Sherman, and D.S Luciano. *Human Physiology: The Mechanisma of Body Function.* McGraw-Hill, 4th Edition, New York, 1985.

[3] R.A. Freitas Jr. *Nanomedicine, Volume I: Basic Capabilities.* Landes Bioscience, Georgetown, TX, 1999.

[4] A.B. Ritter, S. Reisman, and B.B. Michniak. *Biomedical Engineering Principles.* CRC Press, 2005.

[5] Wikipedia. 2008.

[6] Y.C. Fung. *Biomechanics. Mechanical properties of living tissues.* Springer-Verlag, 1993.

[7] V. Kasyanov and I. Knet-s. Deformation energy function of large human blood vessels. *Mekhanika Polimerov,* 1:122–128, 1974.

[8] G. Jiang. Chaos in vocal cord vibration a look at the evidences and promises it provide. *http://www.sfu.ca/ rpyke/335/projects/jiang/report.htm,* 2003.

Chapter 3

Governing Equations

3.1 Introduction

In this chapter, we introduce the basic governing equations for solid deformation and fluid motion. The isothermal systems need only conservation of mass and momentum and non-isothermal problems need energy conservation in addition to mass and momentum. To derive the basic equations of solids and fluids, consider the deformation mapping between original configuration $\boldsymbol{\kappa}_0$ and deformed configuration $\boldsymbol{\kappa}_t$ as shown in Figure 3.1. In the figure, $\mathbf{X}$ is the position vector of the original configuration and $\mathbf{x}$ is the position vector of the deformed configuration.
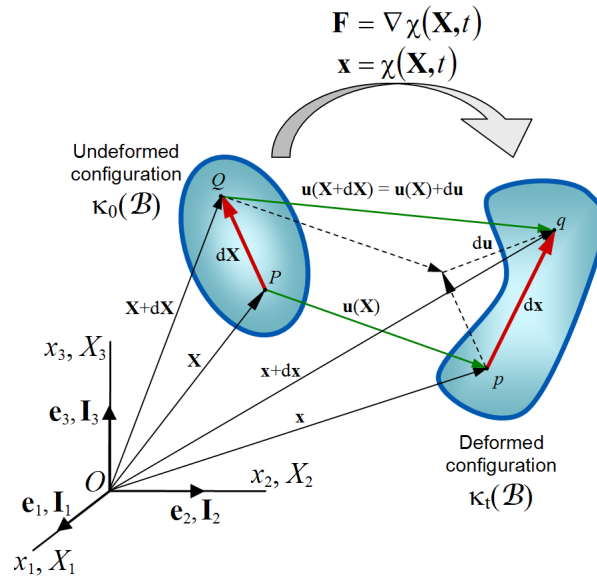
Figure 3.1: Deformation mapping[1].

The displacement vector of all material points is given as $\mathbf{u}(\mathbf{X}, t) = \mathbf{x}(\mathbf{X}, t) - \mathbf{X}$ or $u_i = x_i - \delta_{iJ} X_j$. From the figure, we can also see that $d\mathbf{x} = d\mathbf{X} + d\mathbf{u}$, where $d\mathbf{u}$ is the relative displacement vector. In terms of motion, the vector $d\mathbf{x}$ is related to $d\mathbf{X}$ as

29

$$dx = \frac{\partial \mathbf{x}}{\partial \mathbf{X}}.d\mathbf{X} \tag{3.1}$$

or in indicial notation,

$$dx_j = \frac{\partial x_i}{\partial X_j}dX_j \tag{3.2}$$

In the above equation the deformation gradient is $\mathbf{F} = \partial\mathbf{x}/\partial\mathbf{X}$ or $F_{ij} = \partial x_i/\partial X_j$. In cartesian coordinates $\mathbf{F}$ may be written as

$$\mathbf{F} = \begin{bmatrix} \frac{\partial x_1}{\partial X_1} & \frac{\partial x_1}{\partial X_2} & \frac{\partial x_1}{\partial X_3} \\ \frac{\partial x_2}{\partial X_1} & \frac{\partial x_2}{\partial X_2} & \frac{\partial x_2}{\partial X_3} \\ \frac{\partial x_3}{\partial X_1} & \frac{\partial x_3}{\partial X_2} & \frac{\partial x_3}{\partial X_3} \end{bmatrix} \tag{3.3}$$

Simple assumption that stress tensor $\boldsymbol{\sigma} = \boldsymbol{\sigma}(\mathbf{F})$ can be misleading and a simple rotation can result in change of state of stress. The true transformation consists of stretch and shear. The stretch of the material vector $d\mathbf{X}$ may be written as

$$\lambda = \frac{||d\mathbf{x}||}{||d\mathbf{X}||} = \sqrt{\frac{d\mathbf{x}.d\mathbf{x}}{||d\mathbf{X}||||d\mathbf{X}||}} = \sqrt{\frac{\mathbf{F}.d\mathbf{X}.\mathbf{F}.d\mathbf{X}}{||d\mathbf{X}||||d\mathbf{X}||}} = \sqrt{\frac{d\mathbf{X}.\mathbf{F}^T.\mathbf{F}.d\mathbf{X}}{||d\mathbf{X}||||d\mathbf{X}||}} = \sqrt{\mathbf{e}.\mathbf{F}^T.\mathbf{F}.\mathbf{e}} \tag{3.4}$$

where $\mathbf{e} = d\mathbf{X}/||d\mathbf{X}||$ is the unit vector in the direction of $d\mathbf{X}$. The shear deformation between two initial material vectors $d\mathbf{X}_1$ and $d\mathbf{X}_2$ is determined by the angle θ between the vectors after the deformation, i.e.,

$$\cos\theta = \frac{d\mathbf{x_1}}{||d\mathbf{x_1}||}.\frac{d\mathbf{x_2}}{||d\mathbf{x_2}||} = \frac{\mathbf{e}_1.\mathbf{F}^T.\mathbf{F}.\mathbf{e}_2}{\sqrt{\mathbf{e}_1.\mathbf{F}^T.\mathbf{F}.\mathbf{e}_1}\sqrt{\mathbf{e}_2.\mathbf{F}^T.\mathbf{F}.\mathbf{e}_2}} \tag{3.5}$$

From Equations 3.4 and 3.5 the true deformation can thus be described by the *Cauchy-Green* deformation tensor $\mathbf{C} = \mathbf{F}^T.\mathbf{F}$. These equations can be re-derived in terms of the current configuration to give the relationships in terms of the *Finger* tensor $\mathbf{B} = \mathbf{F}.\mathbf{F}^T$.

In fluid dynamics, not only the deformation but the rate of deformation is also important. The relative velocity between two points is defined by the relative displacement vector. The velocity of a material point is defined as

$$\mathbf{v}(\mathbf{X},t) = \dot{\mathbf{u}}(\mathbf{X},t) = \lim_{\Delta t \to 0} \frac{\mathbf{u}(\mathbf{X},t+\Delta t) - \mathbf{u}(\mathbf{X},t)}{\Delta t} \tag{3.6}$$

From the definition of $\mathbf{u}$ we can now write

$$\mathbf{v}(\mathbf{X},t) = \dot{\mathbf{x}}(\mathbf{X},t) = \lim_{\Delta t \to 0} \frac{\mathbf{x}(\mathbf{X},t+\Delta t) - \mathbf{x}(\mathbf{X},t)}{\Delta t} \tag{3.7}$$

If we now use the definition of $\mathbf{F}$ from Equation 3.1, we have

$$d\mathbf{v} = d\dot{\mathbf{x}} = \dot{\mathbf{F}}.d\mathbf{X} \tag{3.8}$$

The infinitesimal velocity can also be written as a function of space and time as

$$dv = \frac{\partial \mathbf{v}}{\partial \mathbf{x}}.d\mathbf{x} + \frac{\partial \mathbf{v}}{\partial t}.dt \tag{3.9}$$

At a fixed instant of time with $dt = 0$, we get

$$dv = \frac{\partial \mathbf{v}}{\partial \mathbf{x}}.d\mathbf{x} \equiv \mathbf{L}.d\mathbf{x} \tag{3.10}$$

where, $\mathbf{L}$ is the velocity gradient tensor. From Equation 3.8, we can write

$$\mathbf{L}.d\mathbf{x} = d\mathbf{v} = \dot{\mathbf{F}}.d\mathbf{X} = \dot{\mathbf{F}}.\mathbf{F}^{-1}d\mathbf{x} \tag{3.11}$$

This clearly shows that

$$\dot{\mathbf{F}} = \mathbf{L}.\mathbf{F} \tag{3.12}$$

The velocity gradient is often written as a dyadic product[1]of gradient vector ∇ and velocity vector $\mathbf{v}$, i.e., $\nabla \otimes \mathbf{v}$. To relate the rate of deformation to the stress, we need to decompose the gradient tensor $\mathbf{L}$ into two parts representing the rate of deformation (shear) and rotation, i.e,

$$\mathbf{L} = \mathbf{D} + \mathbf{\Omega} \tag{3.14}$$

with $\mathbf{D} = 1/2(\mathbf{L} + \mathbf{L}^T)$ and $\mathbf{\Omega} = 1/2(\mathbf{L} - \mathbf{L}^T)$, or

$$\mathbf{D} = \frac{1}{2}\left(\nabla \otimes \mathbf{v} + (\nabla \otimes \mathbf{v})^T\right)$$
$$\mathbf{\Omega} = \frac{1}{2}\left(\nabla \otimes \mathbf{v} - (\nabla \otimes \mathbf{v})^T\right) \tag{3.15}$$

It should be noted that $2\mathbf{D}$ is the rate of deformation or rate of strain tensor and $\mathbf{\Omega}$ is the vorticity or spin tensor.

For solids the constitutive equations for stress tensor can be written in terms of the Finer tensor and for fluids it is normally written in terms of its rate, i.e.,

$$\sigma = -p\mathbf{I} + \tau(\mathbf{B}) \tag{3.16}$$

for solids and

$$\sigma = -p\mathbf{I} + \tau(\mathbf{D}) \tag{3.17}$$

for fluids. For incompressible linear elastic solids, $\sigma = -p\mathbf{I} + G\mathbf{B}$ and for Newtonian incompressible flows, $\sigma = -p\mathbf{I} + 2\mu\mathbf{D}$, where G is the modulus of rigidity of the solid and μ is the dynamic viscosity of the fluid.

---

[1]Dyadic product of two vectors $\mathbf{u}$ and $\mathbf{u}$ may be written as

$$\mathbf{u} \otimes \mathbf{v} = \begin{bmatrix} u_1 \\ u_2 \\ u_3 \end{bmatrix} \begin{bmatrix} v_1 & v_2 & v_3 \end{bmatrix} = \begin{bmatrix} u_1v_1 & u_1v_2 & u_1v_3 \\ u_2v_1 & u_2v_2 & u_2v_3 \\ u_3v_1 & u_3v_2 & u_3v_3 \end{bmatrix} \tag{3.13}$$

3.2 Incompressible Flow Equations

Since the biofluids are normally incompressible we use incompressible flow assumption throughout this book. The isothermal incompressible flow is governed by conservation of mass and momentum equations. There are various ways of deriving these equations. We refer the reader to appropriate texts for full details [2, 3, 4, 5]. We give the final forms of the continuity and momentum equations here. The conservation of mass equation in its general form is

$$\frac{\partial \rho}{\partial t} + \nabla.(\rho \mathbf{v}) = 0 \tag{3.18}$$

Assuming a constant density flow (incompressible), we have

$$\nabla.\mathbf{v} = 0 \tag{3.19}$$

The momentum equation for an incompressible fluid may be written as

$$\rho \frac{\partial \mathbf{v}}{\partial t} + \rho(\mathbf{v}.\nabla)\mathbf{v} = \rho \mathbf{f} + \nabla.\sigma \tag{3.20}$$

In the above equation $\mathbf{f}$ is the body force vector and constitutive Cauchy-Green stress tensor, σ, varies depending on the type of fluid studied. In order to obtain solution to the continuity and momentum equations we need to prescribe appropriate boundary conditions. Initial conditions will also be necessary for time dependent problems. Following boundary conditions are relevant on a domain boundary. In the direction normal to a boundary, Γ, the Dirichlet condition is $(\mathbf{v}.\mathbf{n}) = v_{n\Gamma}$ and Neumann condition is $(\sigma.\mathbf{n}).\mathbf{n} = t_n$. In a similar fashion we can prescribe the tangential boundary condition as: Dirichlet condition is $(\mathbf{v}.\mathbf{t_i}) = v_{t_i\Gamma}$ and Neumann condition is $(\sigma.\mathbf{n}).\mathbf{t_i} = t_{t_i}$ with $i = 1, 2$. For time dependent problems appropriate velocity and stress should also be given for a complete definition of the problem.

3.2.1 Newtonian flow

The total stress tensor can be written as

$$\sigma = -p\mathbf{I} + \tau \tag{3.21}$$

For Newtonian fluids, the relation between the viscous stress τ and rate of deformation is linear, i.e.,

$$\tau = 2\mu \mathbf{D} = \mu \dot{\gamma} \tag{3.22}$$

As discussed previously the rate of deformation tensor is $\dot{\gamma} = \nabla \otimes \mathbf{v} + (\nabla \otimes \mathbf{v})^T$. Substituting the constitutive equation into the momentum equation, we obtain the momentum and continuity equations as

$$\rho \frac{\partial \mathbf{v}}{\partial t} + \rho(\mathbf{v}.\nabla)\mathbf{v} = \rho \mathbf{f} - \nabla p + \mu \nabla^2 \mathbf{v}$$
$$\nabla.\mathbf{v} = 0 \tag{3.23}$$

The non-dimensional form of the above equations can be obtained using appropriate length, time and velocity scales. For example, if we assume non-dimensional quantities $\mathbf{x}^* = \mathbf{x}/L$, $\mathbf{v}^* = \mathbf{v}/V$, $t^* = t/\theta$ and $p^* = p/\rho V^2$ and substitute into the above equations, we get

$$St\frac{\partial \mathbf{v}^*}{\partial t^*} + (\mathbf{v}^*.\nabla)\mathbf{v}^* = \frac{1}{Fr^2}\mathbf{f}^* - \nabla p^* + \frac{1}{Re}\nabla^2\mathbf{v}^*$$
$$\nabla.\mathbf{v}^* = 0 \tag{3.24}$$

where L, θ and V are appropriate reference quantities and the non-dimensional numbers Strouhal number (St), Reynolds number (Re) and Froude number (Fr) are given as

$$St = \frac{L}{\theta V}; \qquad Re = \frac{\rho V L}{\mu}; \qquad Fr = \frac{V}{\sqrt{gL}} \tag{3.25}$$

3.2.2 Inviscid Flow

For inviscid (zero viscosity) approximation, $\sigma = -p\mathbf{I}$ is used to get the following governing equations.

$$\rho\frac{\partial \mathbf{v}}{\partial t} + \rho(\mathbf{v}.\nabla)\mathbf{v} = \rho\mathbf{f} - \nabla p$$
$$\nabla.\mathbf{v} = 0 \tag{3.26}$$

If the flow is steady, the momentum equation can be integrated along the stream lines to give the following Bernoulli equation

$$\frac{1}{2}(\mathbf{v}.\mathbf{v}) + \frac{p}{\rho} + F = constant \tag{3.27}$$

where F represents the potential head.

3.2.3 Boundary Layer Flow

For flow along a smooth boundary parallel to the flow direction, the viscous forces are only large within the boundary layer. If the boundary layer thickness (δ) is small compared to a typical flow length scale L, the terms of the order of δ/L can be neglected to give in two dimension

$$\frac{\partial u_1}{\partial x_1} + \frac{\partial u_2}{\partial x_2} = 0$$
$$\rho\frac{\partial u_1}{\partial t} + \rho u_1\frac{\partial u_1}{\partial x_1} + \rho u_2\frac{\partial u_1}{\partial x_2} = -\frac{\partial p}{\partial x_1} + \mu\frac{\partial^2 u_1}{\partial x_1^2}$$
$$\frac{\partial p}{\partial x_2} = 0 \tag{3.28}$$

Outside the boundary layer, the flow is assumed to be inviscid and one directional. The equation outside the boundary layer may be written as

$$-\frac{\partial p}{\partial x_1} = \rho V\frac{\partial V}{\partial x_1} \tag{3.29}$$

3.2.4 Generalised Newtonian Fluids

The total stress tensor σ can be expressed in a power series as

$$\sigma = f_0\mathbf{D}^0 + f_1\mathbf{D}^1 + f_2\mathbf{D}^2 + f_3\mathbf{D}^3 + ... \tag{3.30}$$

The Cayley Hamilton theorem [6] states that for any symmetric tensor $\mathbf{D}$ it can be shown that:

$$\mathbf{D}^3 - I_D\mathbf{D}^2 + II_D\mathbf{D} - III_D\mathbf{I} = 0 \tag{3.31}$$

where $I_D = tr\mathbf{D}; II_D = 1/2(I_D^2 - tr\mathbf{D})$ and $III_D = det\mathbf{D}$ are the invarients of $\mathbf{D}$. The power series can now be expressed in terms of scalar functions that are functions of the invarients as

$$\sigma = g_0\mathbf{D}^0 + g_1\mathbf{D}^1 + g_2\mathbf{D}^2 \tag{3.32}$$

With zero deformation, the Cauchy stress for incompressible flow is reduced to hydrostatic pressure $-p\mathbf{I}$. Since $\mathbf{D}^0 = \mathbf{I}$, $g_0 = -p$. For Newtonian fluids g_1 is constant and equal to 2μ and $g_2 = 0$. Thus, for Newtonian fluids, $\sigma = -p\mathbf{I} + 2\mu\mathbf{D}$.

The non-Newtonian fluids differ from Newtonian fluids due to their shear rate dependent viscosity. To represent such fluids, non-Newtonian viscosity, dependent on strain rate tensor $\dot{\gamma}$ can be introduced. Note that the first invariant of the deformation tensor $\mathbf{D}$, $I_D = tr\mathbf{D} = \nabla.\mathbf{v} = 0$. Experimental results [7] show that viscosity rarely depends on $\mathbf{D}^2$ and thus $g_2 = 0$. For simple shear flows normally used to determine viscosity, $det\mathbf{D} = 0$. Thus, the constitutive equation for a non-Newtonian fluid can be expressed as

$$\sigma = -p\mathbf{I} + 2\mu(II_D)\mathbf{D} \tag{3.33}$$

From the expression for the second invariant, $II_d = -\frac{1}{2}(tr\mathbf{D}^2) = -|\dot{\gamma}|^2$ with $I_D = 0$, we can get the constitutive equation for generalised non-Newtonian fluid as

$$\sigma = -p\mathbf{I} + 2\mu(\dot{\gamma})\mathbf{D} \tag{3.34}$$

Some important generalised Newtonian models include power-law model, Carreau-Yasuda model and Casson model. They are listed below.

Power-law model

The viscosity-shear rate relation is given as

$$\mu = \mu_0(\lambda\dot{\gamma})^{n-1} \tag{3.35}$$

where μ_0 is the viscosity for $\dot{\gamma} = 1/\lambda$, λ is a time constant and n the power law constant. If $n > 1$ the fluid is called shear thickening and if $n < 1$ the fluid is referred to as a shear thinning fluid. Examples of shear thinning fluids include blood, polymer solutions and yogurt. The shear thickening behaviour is found in some concentrated suspensions of small particles. The drawback of this model is that it gives unrealistic valves of viscosity at very low and very high shear rates.

Correau-Yasuda model

This model is more realistic and is given as

$$\frac{\mu - \mu_\infty}{\mu_0 - \mu_\infty} = [1 + (\lambda\dot{\gamma})^a]^{(n-1)/a} \tag{3.36}$$

where μ_0 and μ_∞ are the viscosities at low and high shear rates, λ a time constant and n a power law constant. The parameter a determines the transition between the low shear rate region and the power-law region.

Casson model

This model was introduced in Chapter 2 and it is repeated here for completeness. The model was originally introduced by Bingham [8] to represent a certain yield stress τ_0 needed to break networks of polymer chains. One good example of such chain is rouleaux formation in blood. The equation is given as

$$\tau^{\frac{1}{m}} = \tau_0^{\frac{1}{m}} + (\mu_\infty\dot{\gamma})^{\frac{1}{m}} \tag{3.37}$$

With $m = 1$ the model is called Bingham model and when $m = 2$ the model is referred to as the Casson model. In terms of shear dependent viscosity this model may be expressed as

$$\mu = \mu_\infty \left[1 + \left(\frac{\tau_0}{\mu_\infty\dot{\gamma}} \right)^{\frac{1}{m}} \right]^m \tag{3.38}$$

3.2.5   Viscoelastic Fluids

The generalised Newtonian models discussed in the previous subsections can describe the shear rate dependency of viscosity quite well but can not describe the time dependence in response to deformation. This time dependency is described by some fluids that returns to its original position when the applied stress is removed. These fluids not only have a shear dependent viscosity ($\tau(t) = \tau(\dot{\gamma}(t))$) and posses elastic properties ($\tau(t_0, t) = \tau(\gamma(t_0, t))$). The shear rate and shear are defined here as

$$\dot{\gamma}(t) = \frac{\partial\gamma(t_0, t)}{\partial t} \tag{3.39}$$

and

$$\gamma(t_0, t) = \int_{t_0}^{t} \dot{\gamma}(t')dt' \tag{3.40}$$

Each increment in shear $\delta\gamma^n$ at time t^n is experienced by the material will induce a shear stress τ^n which will be a function of time but will be independent of the shear stress that is induced by other increments in shear. This Boltzmann's superposition is generally used in deriving viscoelastic flow equations. The time dependence of the response to shear rate increment at time $t = t^n$ can be defined by a relaxation function, i.e.,

$$\tau(t) = \Sigma_n \delta \gamma^n G_0 e^{\frac{-1}{\lambda_0}(t-t^n)} \tag{3.41}$$

After some integration and generalisation, we get the upper convected Maxwell model as

$$\lambda_0 \left\{ \frac{\partial \tau}{\partial t} + \mathbf{v}.\nabla \tau - [(\nabla \mathbf{v})^T.\tau + \tau.(\nabla \mathbf{v})] \right\} + \tau = 2\mu_0 \mathbf{D} \tag{3.42}$$

Thus for viscoelastic fluids, additional equation for stress should be calculated[9, 10, 11].

3.3   Turbulence

Flow in the human airways is generally turbulent in nature, especially at high flow rates. It is also suspected that blood flow reaches the transition close to the aortic root and also in vessels with a stenosis. Thus, this section is dedicated to modelling turbulence.

Turbulent flow is defined as a flow with random variation of various flow quantities such as velocity, pressure and density. Turbulence is a property of the flow, not the property of a fluid. The turbulent flow is marked by random variation of quantities as shown in Figure 3.3.
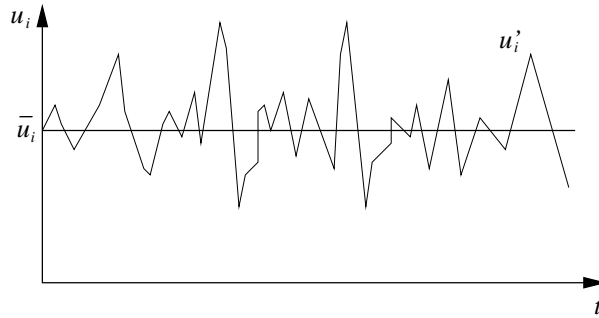
Figure 3.2: Random variation of velocity in a turbulent flow with respect to time

The Navier-Stokes equations are sufficient to resolve all turbulent scales if adequate mesh resolution is used. However, this requires extremely large computer resources. With the present day computers this is possible only for relatively low Reynolds numbers. Until sufficiently fast computing power is available it is essential to employ Reynolds decomposition and turbulence models.

In a real turbulent flow the the kinetic energy is transferred from larger scales to smaller scales. At smallest scale the kinetic energy is transformed into internal energy and this process is called dissipation and the process of energy transfer between the scales is called 'the cascade process'. The smallest turbulent length scale is determined by the molecular viscosity and dissipation rate. Such a length scale is often referred to as *Kolmogorov length scale* and given as

$$\left(\frac{\nu^3}{\epsilon} \right)^{1/4} \tag{3.43}$$

Similarly Kolmogorov velocity and time scales are determined as

$$v = (\nu \epsilon)^{1/4} \tag{3.44}$$

and

$$\tau = \left(\frac{\nu}{\epsilon}\right)^{1/2} \tag{3.45}$$

The dissipation rate can be linked to the energy of large eddies as

$$\epsilon = \frac{U^3}{l} \tag{3.46}$$

where U is the large eddy velocity scale and l is the large eddy length scale. The turbulent kinetic energy of a flow is defined as

$$\kappa = \frac{1}{2}\overline{u_i' u_i'} \tag{3.47}$$

where u_i' is the fluctuating component of the velocity as shown in Figure 3.3. The above relations are given to make the readers aware that the length scales, turbulent kinetic energy and dissipation are closely related. Various turbulence modelling procedures are developed based on these relationships.

3.3.1 Time averaging

As mentioned previously extremely high mesh resolution is required to solve molecular level turbulence and is very expensive and presently not possible for high Reynolds number flows. It is, therefore, obvious that other alternatives are necessary to get an approximate solution. The standard procedure is to employ time averaged Navier-Stokes equations along with a turbulence modelling approach to determine the essential time averaged quantities which reduces the excessive grid resolution otherwise needed. With reference to Figure 3.3 any turbulence quantity of interest may be expressed as

$$\phi = \overline{\phi} + \phi' \tag{3.48}$$

The time averaged quantity may be obtained as

$$\overline{\phi} = \frac{1}{2T}\int_{-T}^{T}\phi(t)dt \tag{3.49}$$

Let us consider a one dimensional steady state incompressible momentum equation to demonstrate time averaging

$$\frac{du^2}{dx} + \frac{1}{\rho}\frac{dp}{dx} - \frac{d}{dx}\left(\nu\frac{du}{dx}\right) = 0 \tag{3.50}$$

Substituting variation of the form of Equation 3.48 for velocity u and pressure p into Equation 3.50 and time averaging, we have

$$\frac{d}{dx}\left[\overline{(\overline{u}+u')(\overline{u}+u')}\right] + \frac{1}{\rho}\frac{d}{dx}\overline{(\overline{p}+p')} - \frac{d}{dx}\left[\nu\frac{d}{dx}\overline{(\overline{u}+u')}\right] = 0 \tag{3.51}$$

In the above equation the average of fluctuating components $\overline{u'}$ and $\overline{p'}$ are equal to zero. Now the simplified form of the above equation may be written as

$$\frac{d}{dx}\left[(\overline{u}^2 + \overline{u'^2})\right] + \frac{1}{\rho}\frac{d\overline{p}}{dx} - \frac{d}{dx}\left[\nu\frac{d}{dx}(\overline{u})\right] = 0 \tag{3.52}$$

Rearranging and rewriting the above momentum equation in multi-dimensions and including the time term, we have

$$\frac{\partial(\rho\overline{u}_i)}{\partial t} + \frac{\partial}{\partial x_j}(\rho\overline{u}_j\overline{u}_i) = -\frac{\partial\overline{p}}{\partial x_i} + \rho\frac{\partial\overline{\tau}_{ij}}{\partial x_j} - \frac{\partial}{\partial x_j}(\rho\overline{u_iu_i}) \tag{3.53}$$

where

$$\overline{\tau}_{ij} = \nu\left(\frac{\partial\overline{u}_i}{\partial x_j} + \frac{\partial\overline{u}_j}{\partial x_i} - \frac{2}{3}\frac{\partial\overline{u}_k}{\partial x_k}\delta_{ij}\right) \tag{3.54}$$

is the time averaged deviatoric stress and $\rho\overline{u_iu_i}$ is a new unknown referred to as *Reynolds stress*. The *Boussinesq assumption* gives the Reynolds stress as

$$-\rho\overline{u_iu_i} = \mu_T\left(\frac{\partial\overline{u}_i}{\partial x_j} + \frac{\partial\overline{u}_j}{\partial x_i} - \frac{2}{3}\frac{\partial\overline{u}_k}{\partial x_k}\delta_{ij}\right) \tag{3.55}$$

or

$$\overline{\tau}_{ij}^R = -\overline{u_iu_i} = \nu_T\left(\frac{\partial\overline{u}_i}{\partial x_j} + \frac{\partial\overline{u}_j}{\partial x_i} - \frac{2}{3}\frac{\partial\overline{u}_k}{\partial x_k}\delta_{ij}\right) \tag{3.56}$$

Thus, the unknown quantity to be modelled is the turbulent kinematic viscosity ν_T.

3.3.2   Relation between κ, ϵ and ν_T

The turbulent kinematic viscosity or turbulent eddy viscosity ν_T has the same dimensions as the laminar viscosity. Thus, we can express the turbulent eddy viscosity in terms of velocity and length scales of a large eddy, i.e.,

$$\nu_T = CUl \tag{3.57}$$

where C is a constant. The definitions of U and l are discussed in Section 3.3.1. In the above equation U may be replaced with $\sqrt{\kappa}$. With such a substitution the turbulent eddy viscosity may be determined by solving a scalar transport equation for κ and assuming an appropriate turbulence length scale l ($\kappa - l$ or one equation models). However, a better expression for turbulent eddy viscosity may be obtained by substituting Equation 3.46 into Equation 3.57 as

$$\nu_T = c_\mu\frac{\kappa^2}{\epsilon} \tag{3.58}$$

where c_μ is a constant. To employ the above equation, we need to solve two transport equations, one for κ and another for ϵ ($\kappa - \epsilon$ or two equation model). Details of many one and two equation models are provided in the following sections.

3.3.3   Reynolds Averaged Navier-Stokes Equations (RANS)

For turbulent flow computations, Reynolds averaged Navier-Stokes equations of motion are written in conservation form as follows
Mean-continuity

$$\frac{1}{\beta^2}\frac{\partial \bar{p}}{\partial t} + \frac{\partial \rho \bar{u}_i}{\partial x_i} = 0 \tag{3.59}$$

Mean-momentum

$$\frac{\partial \bar{u}_i}{\partial t} + \frac{\partial}{\partial x_j}(\bar{u}_j \bar{u}_k) = -\frac{1}{\rho}\frac{\partial \bar{p}}{\partial x_i} + \frac{\partial \bar{\tau}_{ij}}{\partial x_j} + \frac{\partial \bar{\tau}_{ij}^R}{\partial x_j} \tag{3.60}$$

where β is an artificial compressibility parameter, $\bar{u}_i$ are the mean velocity components, p is the pressure, ρ is the density, $\bar{\tau}_{ij}$ is the laminar shear stress tensor given as

$$\bar{\tau}_{ij} = \nu\left(\frac{\partial \bar{u}_i}{\partial x_j} + \frac{\partial \bar{u}_j}{\partial x_i} - \frac{2}{3}\frac{\partial \bar{u}_k}{\partial x_k}\delta_{ij}\right) \tag{3.61}$$

The Reynolds stress tensor, $\bar{\tau}_{ij}^R$, is introduced by Boussinesq's assumption as

$$\bar{\tau}_{ij}^R = -\overline{u_i' u_j'} = \nu_T\left(\frac{\partial \bar{u}_i}{\partial x_j} + \frac{\partial \bar{u}_j}{\partial x_i} - \frac{2}{3}\frac{\partial \bar{u}_k}{\partial x_k}\delta_{ij}\right) - \frac{2}{3}\kappa\delta_{ij} \tag{3.62}$$

In the above equations, ν is the kinematic viscosity of the fluid, ν_T is the turbulent eddy viscosity and δ_{ij} is the Kroneker delta.

3.4   Incompressible Solid

We learned previously for a general elastic solid, the constitutive equation is

$$\sigma = -p\mathbf{I} + \tau(\mathbf{B}) \tag{3.63}$$

The simplest version of such relation is that relates the extra stress τ linearly depends on the Finer tensor (left Cauchy-Green tensor). Such simple material are referred to as linear elastic or neo-Hookean solids. Most rubber like materials and some biological tissues belong to this category.

The equations describe the linear incompressible elastic solids are the continuity and momentum equations along with the constitutive equation

$$\sigma = -p\mathbf{I} + G(\mathbf{B} - \mathbf{I}) \tag{3.64}$$

where G is the shear modulus. The momentum and continuity equations can be written as

$$\rho\frac{\partial \mathbf{v}}{\partial t} + \rho(\mathbf{v}.\nabla)\mathbf{v} = \rho\mathbf{f} - \nabla p + G\nabla.(\mathbf{B} - \mathbf{I})$$

$$\nabla.\mathbf{v} = 0 \tag{3.65}$$

Compared to the terms on the right hand side of the above equation the left hand side terms are normally several orders of magnitude less. Thus, the above equations can be simplified to give (without body forces)

$$-\nabla p + G\nabla.(\mathbf{B} - \mathbf{I}) = 0$$
$$\nabla.\mathbf{v} = 0 \tag{3.66}$$

3.4.1 Small Strain Approximation

The deformation tensor is

$$\mathbf{F} = \frac{\partial \mathbf{x}}{\partial \mathbf{X}} = (\nabla^X \mathbf{x})^T = (\nabla^X (\mathbf{X} + \mathbf{u}))^T = \mathbf{I} + (\nabla^X \mathbf{u})^T \approx \mathbf{I} + (\nabla^x \mathbf{u})^T \tag{3.67}$$

The above approximation is only possible for small strains in which $||\nabla^x \mathbf{u}|| \approx ||\nabla^X \mathbf{u}||$. The Finger tensor can now be approximated as

$$\mathbf{B} = \mathbf{F}.\mathbf{F}^T \approx \mathbf{I} + (\nabla^x \mathbf{u})^T + \nabla^x \mathbf{u} \tag{3.68}$$

The infinitesimal strain is defined as

$$\varepsilon = \frac{1}{2}(\nabla^x \mathbf{u} + (\nabla^x \mathbf{u})^T) \tag{3.69}$$

Replacing $\mathbf{B}$ and $\mathbf{I}$ in Equation 3.66, we get

$$-\nabla p + G\nabla.\varepsilon = 0$$
$$\nabla.\mathbf{u} = 0 \tag{3.70}$$

or

$$-\nabla p + G\nabla^2 \mathbf{u} = 0$$
$$\nabla.\mathbf{u} = 0 \tag{3.71}$$

Prescribing appropriate boundary conditions (either stress or displacement) complete the problem definition.

3.4.2 Viscoelastic Solids

As mentioned previously, the viscoelastic material exhibits both viscous and elastic effects. One of the simplest models used to represent such effects is the Maxwell model. As shown in Figure 3.3, the Maxwell model can be mechanically represented by a spring and a dashpot connected in series.

From the figure, the total displacement may be written as the displacement of spring and the dashpot, i.e.,
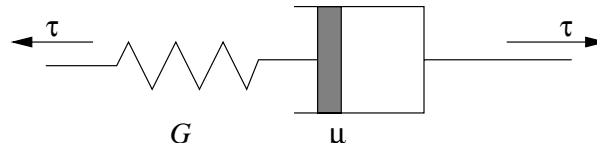
Figure 3.3: Physical representation of Maxwell model.

$$u^t = u^s + u^d \tag{3.72}$$

The rate of change may be written as

$$\dot{u}^t = \dot{u}^s + \dot{u}^d = \frac{\dot{F}^s}{E} + \frac{F^d}{\mu} \tag{3.73}$$

From this the strain rate may be calculated by dividing the force by area and displacement by length, i.e.,

$$\dot{\varepsilon} = \frac{\dot{\sigma}}{E} + \frac{\sigma}{\mu} \tag{3.74}$$

This equation clearly shows that the strain rate is governed by both the elasticity of spring and viscosity of the dashpot.

3.5   Summary

This chapter introduced some relevant equations governing the fluid flow and solid deformation. Only incompressible flow equations and incompressible solid equations are covered here as the majority of biofluids and biosolids are incompressible in nature. Only RANS turbulence models are covered here. However, use of LES in modelling human airway turbulence is becoming common. Only linear viscoelastic solids are covered here. The available models for non-linear viscoelasticity are extremely complex. It is also not clear whether such available models are suitable for modelling biosolids.

Bibliography

[1] Wikipedia. 2008.

[2] G.K. Bachelor. *An Introduction to Fluid Mechanics.* Cambridge University Press, 1967.

[3] H. Schlichting. *Boundary Layer Theory (6ᵗʰ) Edition.* McGraw-HillPublications, 1968.

[4] R.W. Lewis, P. Nithiarasu, and K.N. Seetharamu. *Fundamentals of the Finite Element Method for Heat and Fluid Flow.* Wiley, Chiester, 2004.

[5] O.C. Zienkiewicz, R.L. Taylor, and P. Nithiarasu. *The finite element method for fluid dynamics.* Elsevier Butterworth-Heinemann, Elsevier Butterworth-Heinemann, Burlinton, MA, 2005.

[6] P. Chadwick. *Continuum Mechanics.* John Wiley & Sons, 1976.

[7] C.W. Macosko. *Rheology, principles, measurements and applications.* VCH Publishers Inc., 1994.

[8] E. Bingham. *Fluidity and plasticity.* McGraw-Hill, 1922.

[9] P. Nithiarasu. A fully explicit characteristic based split (cbs) scheme for viscoelastic flow calculations. *International Journal for Numerical Methods in Engineering*, 60:949–978, 2004.

[10] C.B. Liu and P. Nithiarasu. The explicit characteristic based split (cbs) method for viscoelastic flow past a circular cylinder. *International Journal for Numerical Methods in Fluids*, 57:157–176, 2008.

[11] C.B. Liu and P. Nithiarasu. An artificial-dissipation-based fractional step scheme for upper-convected maxwell (ucm) fluid flow past a circular cylinder. *International Journal for Numerical Methods in Fluids*, 57:1171 – 1187, 2008.

Chapter 4

Analytical Forms

4.1   Introduction

In this chapter we discuss some basic analytical solutions for flow through circular tubes. In reality, the arteries are very complex and not necessarily circular. The additional difficulties of an arterial or venous system is that they have both bifurcations and curvature. Thus, studying straight tubes with circular cross section is a crude approximation. Such approximation can be used as a first and quick step for obtaining some basic results on blood flow through blood vessels. With reference to Figure 4.1, we can write the incompressible Navier-Stokes equations in axisymmetric coordinates as

$$\frac{1}{r}\frac{\partial}{\partial r}(ru_r) + \frac{\partial u_z}{\partial z} = 0$$

$$\frac{\partial u_r}{\partial t} + u_r\frac{\partial u_r}{\partial r} + u_z\frac{\partial u_r}{\partial z} = -\frac{1}{\rho}\frac{\partial p}{\partial x} + \nu\left[\frac{\partial}{\partial r}\left(\frac{1}{r}\frac{\partial}{\partial r}(ru_r)\right) + \frac{\partial^2 u_r}{\partial z^2}\right]$$

$$\frac{\partial u_z}{\partial t} + u_r\frac{\partial u_z}{\partial r} + u_z\frac{\partial u_z}{\partial z} = -\frac{1}{\rho}\frac{\partial p}{\partial z} + \nu\left[\frac{\partial}{\partial r}\left(\frac{1}{r}\frac{\partial}{\partial r}(ru_z)\right) + \frac{\partial^2 u_z}{\partial z^2}\right] \tag{4.1}$$
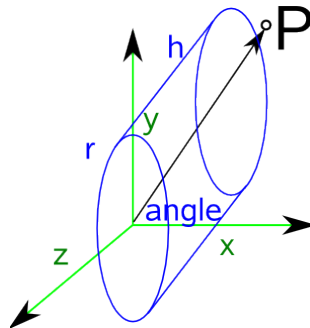
Figure 4.1: Cylindrical coordinates.

Note that the velocity in the circumferential direction is assumed to be zero, i.e., $u_\phi = 0$ and all the derivatives in this direction are also omitted. If we assume Newtonian fully developed profile,

all the derivatives with respect the axial z direction and the velocity in radial direction u_r are also equal to zero. Thus, the Navier-Stokes equations 4.1 are reduced to

$$\frac{\partial u_z}{\partial t} = -\frac{1}{\rho}\frac{\partial p}{\partial z} + \frac{\nu}{r}\frac{\partial}{\partial r}\left(r\frac{\partial u_z}{\partial r}\right) \tag{4.2}$$

The above equation can be written in non-dimensional form as

$$\alpha^2\frac{\partial u_z^*}{\partial t^*} = -Re\frac{\partial p^*}{\partial z^*} + \frac{1}{r^*}\frac{\partial}{\partial r^*}\left(r^*\frac{\partial u_z^*}{\partial r^*}\right) \tag{4.3}$$

Where the non-dimensional scales are $u_z^* = u_z/u_\infty$, $r^* = r/R$, $z^* = z/R$, $p^* = p/\rho u_\infty^2$ and $t^* = t\omega$, where u_∞ is a reference velocity, D is the diameter of the tube and ω is the frequency. Two non-dimensional parameters α and Re are defined as

$$\alpha = R\sqrt{\frac{\omega}{\nu}}; \quad \text{and} \quad Re = \frac{Ru_\infty}{\nu} \tag{4.4}$$

They are referred to as the *Womersley* and *Reynolds* numbers respectively. In order to understand the impact of these parameters, these values for some arteries are listed in Table 4.1

From the values of α it is fairly obvious that for the vessels listed, the influence of α is great. In other words, the transient term can not be simply neglected. However, for veins and extracorporeal blood-handling systems (external systems) the Womersley number or parameter can be very low ($\alpha << 1$). It is also possible that this parameter is low for arterioles and capillaries. Thus, a steady flow calculation may be useful for limited number of problems. If $\alpha << 1$, we can reduce the equation 4.3 to

$$0 = -Re\frac{\partial p^*}{\partial z^*} + \frac{1}{r^*}\frac{\partial}{\partial r^*}\left(r^*\frac{\partial u_z^*}{\partial r^*}\right) \tag{4.5}$$

or in dimensional form

$$-\frac{1}{\rho}\frac{\partial p}{\partial z} + \frac{\nu}{r}\frac{\partial}{\partial r}\left(r\frac{\partial u_z}{\partial r}\right) = 0 \tag{4.6}$$

Following section gives some insight into steady Newtonian and non-Newtonian flows.

4.2   Steady Flow in Rigid Tubes

The Newtonian flow equation for steady flow can be rewritten as

$$\frac{\partial}{\partial r}\left(r\frac{\partial u_z}{\partial r}\right) = \frac{r}{\nu}\frac{\partial p}{\partial z} \tag{4.7}$$

where $\nu = \mu/\rho$ is the dynamic viscosity. Integration of the above equation with respect r gives

$$u_z = \frac{r^2}{4\mu}\frac{\partial p}{\partial z} + ar + b \tag{4.8}$$

where a and b are the constants to be determined by applying appropriate boundary conditions. Assuming $\partial u_z/\partial r = 0$ at $r = 0$, we obtain $a = 0$. At $r = R$, $u_z = 0$ and thus

Table 4.1: Some typical blood flow parameters for humans. Collected from various sources, see [1, 2]

Artery	Flow rate (cycle averaged, ml/s)	Diameter (cycle averaged, mm)	Reynolds number (Radius based)	Wall shear stress, dyne/cm^2	Womersley number
Thoracic aorta	45-93	23-28	320 - 665	1.0 - 2.0	22
Femoral		5.4			4.0
Common carotid	8.7	7.3	216	7.9	

$$b = -\frac{R^2}{4\mu}\frac{\partial p}{\partial z} \tag{4.9}$$

Substituting we get

$$u_z = -\frac{R^2}{4\mu}\frac{\partial p}{\partial z}\left[1 - \frac{r^2}{R^2}\right] \tag{4.10}$$

Integrating the above equation across the cross section of the tube gives the flow rate Q as

$$Q = -\frac{\pi R^4}{8\mu}\frac{\partial p}{\partial z} \tag{4.11}$$

The wall shear stress is given as

$$\tau_w = \mu\frac{\partial u_z}{\partial r} = \frac{r}{2}\frac{\partial p}{\partial z} \tag{4.12}$$

The above equations are also referred to as *Poiseuille's law* for Newtonian fully developed profile. For Newtonian flow the above solution is suitable. Due to the constant pressure gradient of a fully developed flow, the shear stress varies linearly from zero at the centre of the tube to an appropriate value at the walls (see Equation 4.12). If we assume non-Newtonian flow and assume a plug at the centre where the fluid travels as a plug. Within this region the stress is less than the yield stress. If we assume this region is within a critical radius of R_c, the shear stress within this region is $\tau < \tau_y$[1]. Out side this radius $\tau > \tau_y$ and at the interface $\tau = \tau_y$., i.e,

$$\tau_y = \frac{R_c}{2}\frac{\partial p}{\partial z} \tag{4.13}$$

If we assume the fluid to be Casson fluid (refer to Equation 3.37),

$$\sqrt{\tau} = \sqrt{\frac{r}{2}\frac{\partial p}{\partial z}} = \sqrt{\tau_y} + \sqrt{\mu\dot{\gamma}} = \sqrt{\frac{R_c}{2}\frac{\partial p}{\partial z}} + \sqrt{\mu\dot{\gamma}} \tag{4.14}$$

Substituting $\dot{\gamma} = \frac{\partial u_z}{\partial z}$ and squaring both sides

$$\frac{r}{2}\frac{\partial p}{\partial z} = \frac{R_c}{2}\frac{\partial p}{\partial z} + \mu\frac{\partial u_z}{\partial r} + 2\sqrt{\frac{R_c}{2}\frac{\partial p}{\partial z}}\sqrt{\mu\frac{\partial u_z}{\partial r}} \tag{4.15}$$

Rearranging and simplifying

$$\mu\frac{\partial u_z}{\partial r} = \frac{1}{2}\frac{\partial p}{\partial z}\left[r - 2\sqrt{rR_c} + R_c\right] \tag{4.16}$$

The above equation can be integrated along the radial direction to the radius R, we get,

$$u_z(r) = \frac{1}{4\mu}\frac{\partial p}{\partial z}\left[(r^2 - R^2) - \frac{8}{3}(r^{3/2} - R^{3/2}) + 2R_c(R - r)\right] \tag{4.17}$$

Note that the integration constant is determined by applying $u_z = 0$ at $r = R$. The plug flow velocity profile can be obtained by substituting $r = R_c$ in the above equation. The flow rate can be obtained by integrating $u_z(r)$ over the cross sectional area.

$$Q = \int_{o}^{R} u_z(r)2\pi r dr = -\frac{\pi R^4}{8\mu}\frac{\partial p}{\partial z}F(\zeta) \tag{4.18}$$

where

$$F(\zeta) = 1 - \frac{16}{7}\sqrt{\zeta} + \frac{4}{3}\zeta - \frac{1}{21}\zeta^4 \tag{4.19}$$

with $\zeta = 2\tau_y/R|dp/dx| = Rz/R$. If we substitute $\tau_y = 0$ and $\zeta = 0$ into the Casson model equations above, we obtain the equations for Newtonian flow. Even though the Womersley parameter is assumed to be very small in this section, the pressure gradient and velocity can be described in terms of harmonics as

$$\frac{\partial p}{\partial z} = \frac{\partial \hat{p}}{\partial z}e^{i\omega t}; \quad u_z = \hat{u}_z e^{i\omega t} \tag{4.20}$$

where $i = \sqrt{-1}$. The complex representation of the pressure and velocity is attributed to the Euler's relation

$$e^{i\omega t} = cos(\omega t) + isin(\omega t) \tag{4.21}$$

where the real part is $cos(\omega t) = \Re[e^{i\omega t}]$ and the imaginary part is $sin(\omega t) = IM[e^{i\omega t}]$. It is also important to note that $i^2 = -1$ and $i^3 = -i$.

With the relationships in Equation 4.20, the velocity profiles at low Womersley numbers for Newtonian (Eq.4.10) and non-Newtonian (Eq.4.17) flows may be written as,

$$u_z(r) = -\frac{1}{4\mu}\frac{\partial \hat{p}}{\partial z}\left(R^2 - r^2\right)e^{i\omega t} \quad \text{and}$$

$$u_z(r) = \frac{1}{4\mu}\frac{\partial \hat{p}}{\partial z}\left[(r^2 - R^2) - \frac{8}{3}(r^{3/2} - R^{3/2}) + 2R_c(R - r)\right]e^{i\omega t} \tag{4.22}$$

These equations are quasi-static equations. In the above equations quantities with aˆindicates a known amplitude.

4.3   Unsteady Flow in Rigid Tubes

Equation 4.2 represents the governing equation for all values of Womersley parameter. If we substitute Equation 4.20 into Equations 4.2 we get

$$\nu\frac{\partial^2 \hat{u}_z(r)}{\partial r^2} + \frac{\nu}{r}\frac{\partial \hat{u}_z(r)}{\partial r} - i\omega\hat{u}_z(r) = \frac{1}{r}\frac{\partial \hat{p}}{\partial z} \tag{4.23}$$

Replacing r with $s = i^{3/2}\alpha r/R$, we can rewrite the above equation as

$$s^2\frac{\partial^2 \hat{u}_z}{\partial s^2} + s\frac{\partial \hat{u}_z}{\partial s} + (s^2 - n^2)\hat{u}_z = 0 \tag{4.24}$$

This equation is known as the Bessel's equation of first kind and n^{th} order. The solution to this equation is[3]

$$\hat{u}_z(r) = \frac{i}{\rho\omega}\frac{\partial\hat{p}}{\partial z}\left[1 - \frac{J_o(i^{3/2}\alpha r/R)}{J_o(i^{3/2}\alpha)}\right] \tag{4.25}$$

Substituting into Equation 4.20 we get

$$u_z(r) = \frac{i}{\rho\omega}\frac{\partial\hat{p}}{\partial z}\left[1 - \frac{J_o(i^{3/2}\alpha r/R)}{J_o(i^{3/2}\alpha)}\right]e^{i\omega t} \tag{4.26}$$

Only the real part of the above equation is used in the calculations. Similar analytical solution to non-Newtonian flows is not available and numerical solution is normally used.

4.4   Unsteady Flow in Distensible Tubes

The simplest form of unsteady compliant model available for the arterial system is the basic Windkessel model (see Figure 4.2). This model represents the compliant artery or system as a combination of resistance and capacitance as shown in Figure 4.2. The capacitance (spring and a moving wall in Figure 4.2) accounts for the moving wall and the resistance R_p at exit represents the resistance offered by the network downstream.
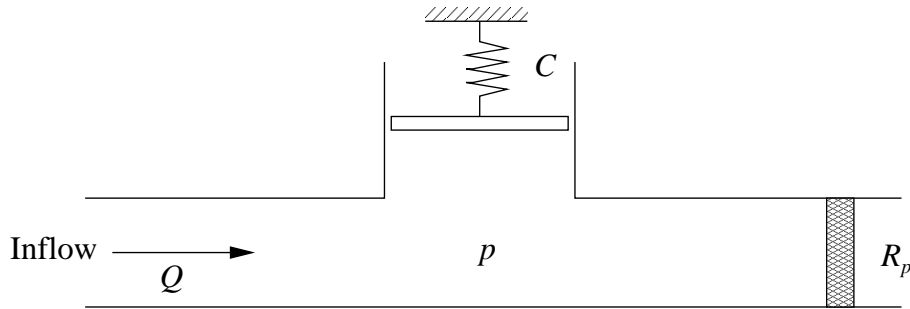
Figure 4.2: Windkessel element representation.

The distensibility (capacitance) of the vessel is defined as

$$C = \frac{dV}{dp} \tag{4.27}$$

where V is the volume and p is the pressure. Simple mass balance between the inlet and exit can be related to rate of change in volume. The flow rate into the vessel is Q the flow rate at exit is p/R_p. The difference between the inlet and exit flow rate must be equal to any rate of change in volume of the vessel, i.e.,

$$Q - \frac{p}{R_p} = \frac{dV}{dt} = \frac{dV}{dp}\frac{dp}{dt} = C\frac{dp}{dt} \tag{4.28}$$

or

$$\frac{dp}{dt} = \frac{Q}{C} - \frac{p}{CR_p} \tag{4.29}$$

Perumal Nithiarasu, Swansea University

Assuming that the systole takes place between $t = 0$ and $t = t_s$ and diastole takes place between $t = t_s$ and $t = T$, we can assume $Q(t) = Q_0$ during systole and $Q(t) = 0$ during diastole. With this assumption the equation for systole may be written as

$$\frac{dp}{dt} = \frac{Q_0}{C} - \frac{p}{CR_p} \tag{4.30}$$

Assuming a initial pressure value of $p = p_0$ we can integrate the above equation and get

$$p(t) = R_p Q_0 - (R_p Q_0 - p_0)e^{\frac{-t}{R_p C}} \tag{4.31}$$

During diastole the equation becomes

$$\frac{dp}{dt} = -\frac{p}{R_p C} \tag{4.32}$$

Applying $p = p_T$ at $t = T$ and integrating

$$p(t) = p_T e^{\frac{-(t-T)}{R_p C}} \tag{4.33}$$

Although Windkessel relationship is simple, its use is very limited as the time lag between the proximal and distal ends of an arterial system is not included in this model.

4.5 Summary

The chapter is expected to introduce the reader to some analytical methods. Majority of the literature available are meant for solving flow through different types of circular vessels. In reality, the blood vessels are not perfectly circular and flow through vessel networks are not easily solved using analytical solutions. Thus, numerical treatment of many of the governing equations is essential to completely study the blood vessels.

Bibliography

[1] C.R. Ethier and C.A. Simmons. *Introductory Biomechanics. From Cells to Organisms.* Cambridge University Press, 2007.

[2] K.B. Chandran, A.P. Yoganathan, and S.E. Rittgers. *Biofluid Mechanics. The Human Circulation.* Taylor & Francis, 2007.

[3] L. Waite and J. Fine. *Applied Biofluid Mechanics.* McGraw Hill, 2007.

Chapter 5

Computational Methods

5.1   Introduction

Many of the realistic problems of biofluid dynamics have no exact solution. Where available, the analytical solutions are often limited to very simple problems with simple boundary conditions. Thus, computational or numerical methods play an important role in obtaining realistic solutions to many biofluid dynamics problems. The need for numerical solutions is demonstrated in Figure 5.1. If the variation is linear, it is a matter of determining two constants from appropriate conditions to represent the variable. The situation is similar if the variation is quadratic but now we need at least three known conditions to determine the variation. However, if the representation of a variable using analytical relations is either difficult or not possible then we have to employ an approximation as shown in Figure 5.1(d). In this figure the linear variation is applied in small spatial intervals to closely represent the true variation. It is obvious from the figure that if the size of the *spatial* interval approaches zero, the approximate numerical solution approaches the exact solution. The principles of all numerical approximations are similar to the one explained above. In a similar fashion a fluid flow variable can also be *discretized* in time.

Figure 5.2(a) shows a typical numerical model[1]. A typical domain discretization is shown in Figure 5.2(b). Once the physical problem is simplified, the next step is to decide on the mathematical model governing the problem. With appropriate spatial and temporal discretizations, and boundary and initial conditions an approximate solution to these equations can be obtained.

As mentioned before, discretization methods involve two components: spatial and temporal discretizations. The spatial discretization consists of setting up a mesh or a grid by which the continuum of space is replaced by a finite number of points where the numerical values of the variables will have to be determined. It is intuitively obvious that the accuracy of a numerical approximation will be directly dependent on the size of the mesh, that is, the better the discretized space approaches the continuum, the better the approximation of the numerical scheme. In other words, the error of a numerical simulation tends to zero when the mesh size tends to zero, and the rapidity of this variation will be characterized by the order of the numerical discretization of the equations. On the other hand, for complex geometries the solution will also be dependent on the form of the mesh.

Once a mesh has been defined the equations can be discretized, leading to the transformation of the differential or integral equations to discrete algebraic operations involving the values of the unknowns at the mesh points. For time-dependent problems an intermediate step is obtained,
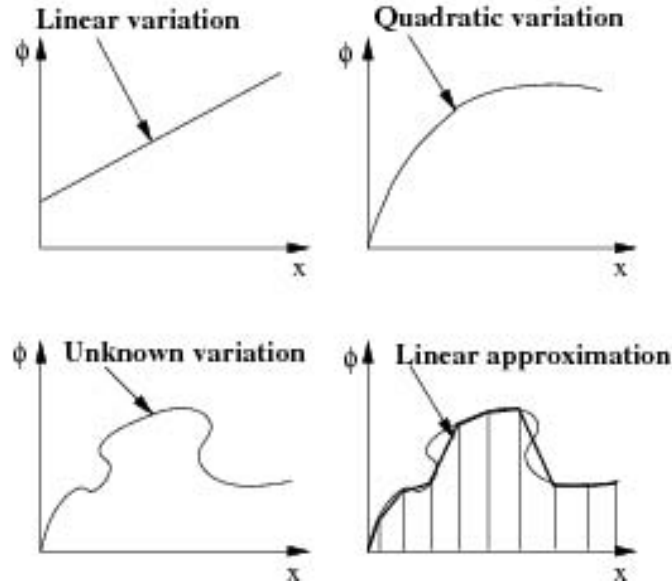
Figure 5.1: Numerical approximation in space

namely a system of ordinary differential equations (ODE's) in time which, through an integration scheme in time, will ultimately lead to an algebraic system for the unknowns at a given time level. For physical time-dependent problems, such as those associated with transient flow behaviour or those connected to time-varying boundary conditions, there is obviously no alternative to the use of a time-dependent mathematical model whereby, in addition, time accuracy of the numerical solution is required. However, with stationary problems an alternative exists, and the user can decide to work with a time-independent formulation, or apply a time-dependent model, and follow the numerical solution in time until the steady state is reached.

5.2   Spatial Discretization

The major spatial discretization methods are the finite difference, finite volume and finite element methods. The finite difference method (FDM) is a popular technique, whilst the finite element method (FEM) is popular for a variety of problems of biofluid dynamics. The finite volume method (FVM) by which the integral form of the conservation laws are discretized can be treated as an independent method due to its flexibility on unstructured meshes.

5.2.1   Finite Difference Method(FDM)

The finite difference method is based on the properties of Taylor expansions. It is the oldest of the methods applied to obtain numerical solutions of differential equations, and the first application is considered to have been developed by Euler in 1768. It may be the simplest method to apply, but it requires a high degree of regularity in the mesh. In particular, the mesh have to be set up in a structured way, by which means the mesh points, in an n-dimensional space, are located at the intersections of n family of rectilinear or curved lines[2, 3, 4].

(a) Numerical model

(b) Mesh
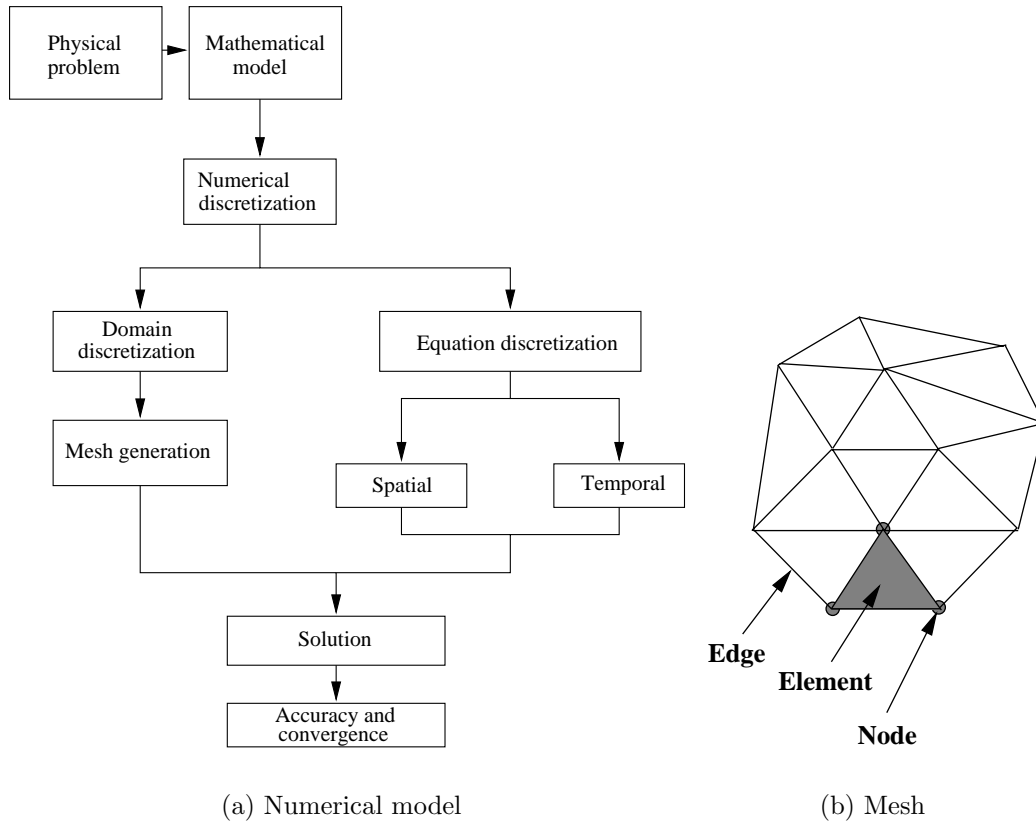
Figure 5.2: A typical numerical model and a typical grid or mesh. Elements, nodes and edges.
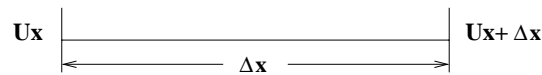
Figure 5.3: One dimensional FDM discretization.

The forward Taylor expansion of a variable u in space may be written as(Figure 5.3)

$$u_{(x+\Delta x)} = u_{(x)} + \frac{\Delta x}{1!}\frac{\partial u_{(x)}}{\partial x} + \frac{(\Delta x)^2}{2!}\frac{\partial^2 u_{(x)}}{\partial x^2} + \frac{(\Delta x)^3}{3!}\frac{\partial^3 u_{(x)}}{\partial x^3} + \cdots \tag{5.1}$$

Similarly a backward Taylor series may be written as

$$u_{(x-\Delta x)} = u_{(x)} - \frac{\Delta x}{1!}\frac{\partial u_{(x)}}{\partial x} + \frac{(\Delta x)^2}{2!}\frac{\partial^2 u_{(x)}}{\partial x^2} - \frac{(\Delta x)^3}{3!}\frac{\partial^3 u_{(x)}}{\partial x^3} + \cdots \tag{5.2}$$

The idea of finite difference methods is actually quite simple, since it corresponds to an estimation of a derivative by the ratio of two differences according to the definition of the derivative. Now we consider three different formulae (Figure 5.4). We can write a forward difference formula
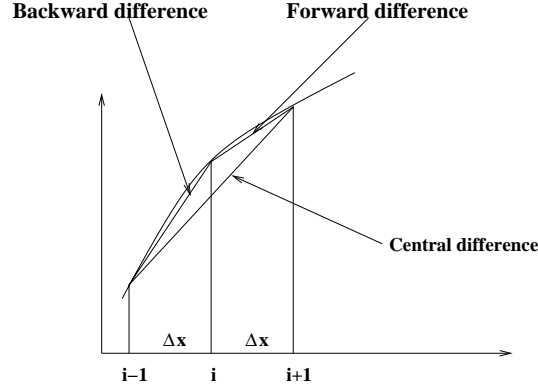
Figure 5.4: Spatial gradient approximations.

for a first order derivative by either taking the difference between $i + 1^{th}$ (or $x + \Delta x^{th}$) and i^{th}(or x^{th}) values of the variable and dividing by the distance between the two points or by using the forward Taylor expansion as

$$\frac{u_{i+1} - u_i}{\Delta x} = \frac{\partial u_i}{\partial x} + O(\Delta x) \tag{5.3}$$

Similarly the backward difference (Figure 5.4 or Equation 5.2) may be written as

$$\frac{u_i - u_{i-1}}{\Delta x} = \frac{\partial u_i}{\partial x} + O(\Delta x) \tag{5.4}$$

The central difference is obtained by taking the difference between the points on both sides of the ith point and dividing the difference by the distance between $i + 1^{th}$ and $i - 1^{th}$ points. Alternatively the central difference formula can be obtained by adding Equations 5.1 and 5.2 as

$$\frac{u_{i+1} - u_{i-1}}{2\Delta x} = \frac{\partial u_i}{\partial x} + O(\Delta x)^2 \tag{5.5}$$

The forward difference formula for $\partial u_i / \partial x$ can be considered as a central difference with respect to the point (Figure 5.5),

$$x_{i+1/2} = \frac{x_i + x_{i+1}}{2} \tag{5.6}$$

$$\left[\frac{\partial u}{\partial x}\right]_{i+1/2} = \frac{u_{i+1} - u_i}{\Delta x} + O(\Delta x)^2 \tag{5.7}$$

$$\left[\frac{\partial u}{\partial x}\right]_{i-1/2} = \frac{u_i - u_{i-1}}{\Delta x} + O(\Delta x)^2 \tag{5.8}$$
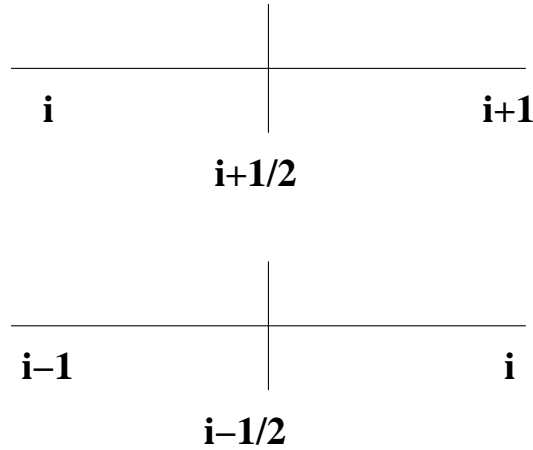
Figure 5.5: Central difference between adjacent points.

For difference formulae using an arbitrary number of points, a one-side, second-order difference formula for $\partial u_i/\partial x$, containing only the upstream points $i - 2$, $i - 1$, i, can be obtained by an expression of the form

$$\frac{\partial u_i}{\partial x} = \frac{au_i + bu_{i-1} + cu_{i-2}}{\Delta x} + O(\Delta x)^2 \tag{5.9}$$

The coefficients (a, b, c) are found from a Taylor expansion. Writing

$$u_{i-1} = u_i - \frac{\Delta x}{1!}\frac{\partial u_i}{\partial x} + \frac{(\Delta x)^2}{2!}\frac{\partial^2 u_i}{\partial x^2} - \frac{(\Delta x)^3}{3!}\frac{\partial^3 u_i}{\partial x^3} + \cdots \tag{5.10}$$

$$u_{i-2} = u_i - \frac{2\Delta x}{1!}\frac{\partial u_i}{\partial x} + \frac{(2\Delta x)^2}{2!}\frac{\partial^2 u_i}{\partial x^2} - \frac{(2\Delta x)^3}{3!}\frac{\partial^3 u_i}{\partial x^3} + \cdots \tag{5.11}$$

To substitute and compare coefficients

$$a + b + c \;=\; 0 \tag{5.12}$$

$$2c + b \;=\; -1 \tag{5.13}$$

$$4c + b \;=\; 0 \tag{5.14}$$

Substituting a, b and c values

$$\frac{\partial u_i}{\partial x} = \frac{3u_i - 4u_{i-1} + u_{i-2}}{2\Delta x} + O(\Delta x)^2 \tag{5.15}$$

Second order terms may be approximated again by using the Taylor series expansions. If we subtract Equation 5.2 from Equation 5.1 and labeling nodes with i (see Figure 5.6), we get the central difference approximation for second order derivatives as
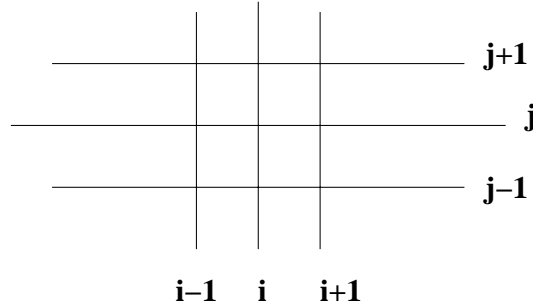
Figure 5.6: Structured grid

$$\frac{\partial^2 u_i}{\partial x^2} = \frac{u_{i+1} - 2u_i + u_{i-1}}{\Delta x^2} + O(\Delta x)^2 \tag{5.16}$$

Alternatively, we can discretize the second derivative as

$$\frac{\partial^2 u_i}{\partial x^2} = \frac{\left[\frac{\partial u}{\partial x}\right]_{i+1} - \left[\frac{\partial u}{\partial x}\right]_i}{\Delta x} \tag{5.17}$$

Application of backward difference to the first order derivatives in the above equation results in Equation 5.16. One sided backward formula for second derivatives may be written as

$$\frac{\partial^2 u_i}{\partial x^2} = \frac{u_i - 2u_{i-1} + u_{i-2}}{\Delta x^2} + O(\Delta x)^2 \tag{5.18}$$

Two dimensional FDM formulae for first and second order derivatives may be written as (Figure 5.6)

$$\left[\frac{\partial u}{\partial x}\right]_{i,j} = \frac{u_{i+1,j} - u_{i,j}}{\Delta x} + O(\Delta x) \tag{5.19}$$

$$\left[\frac{\partial u}{\partial y}\right]_{i,j} = \frac{u_{i,j+1} - u_{i,j}}{\Delta y} + O(\Delta y) \tag{5.20}$$

$$\left[\frac{\partial^2 u}{\partial x^2}\right]_{i,j} = \frac{u_{i+1,j} - 2u_{i,j} + u_{i-1,j}}{\Delta x^2} + O(\Delta x) \tag{5.21}$$

The mixed derivatives can be discretized using backward differences as

$$\left[\frac{\partial}{\partial x}\left(\frac{\partial u}{\partial y}\right)\right]_{i,j} = \frac{\partial}{\partial x}(\Psi)_{i,j} = \frac{\Psi_{i,j} - \Psi_{i-1,j}}{\Delta x} + O(\Delta x) \tag{5.22}$$

Substituting,

$$\Psi_{i,j} = \left[\frac{\partial u}{\partial y}\right]_{i,j} = \frac{u_{i,j} - u_{i,j-1}}{\Delta y} + O(\Delta y) \tag{5.23}$$

and

$$\Psi_{i-1,j} = \left[\frac{\partial u}{\partial y}\right]_{i-1,j} = \frac{u_{i-1,j} - u_{i-1,j-1}}{\Delta y} + O(\Delta y) \tag{5.24}$$

we get

$$\left[\frac{\partial}{\partial x}\left(\frac{\partial u}{\partial y}\right)\right]_{i,j} = \frac{u_{i,j} - u_{i,j-1} - u_{i-1,j} + u_{i-1,j-1}}{\Delta x \Delta y} + O(\Delta x, \Delta y) \tag{5.25}$$

Similarly forward and central differences can be done. If $\Delta x = \Delta y$, Equation 5.25 is reduced to

$$\left[\frac{\partial}{\partial x}\left(\frac{\partial u}{\partial y}\right)\right]_{i,j} = \frac{u_{i,j} - u_{i,j-1} - u_{i-1,j} + u_{i-1,j-1}}{\Delta x^2} + O(\Delta x^2) \tag{5.26}$$

5.2.2 Finite Volume Method (FVM)

The FVM takes full advantage of an arbitrary mesh, where a large number of options are open for the definition of the control volumes around which the conservation laws are expressed[3, 4]. Modifying the shape and location of the control volumes associated with a given mesh point, as well as varying the rules and accuracy for the evaluation of the fluxes through the control surfaces, gives considerable flexibility to the finite volume method. In addition, by the direct discretization of the integral form of the conservation laws we can ensure that the basic quantities mass, momentum and energy will remain conserved at the discrete level.
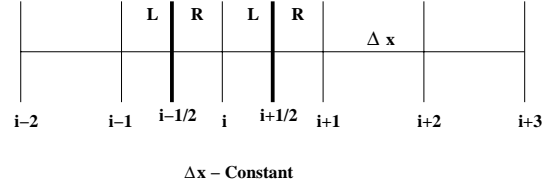
Figure 5.7: One-dimensional finite volume discretization.

One-dimensional approximation

The equation in integral conservation form is (Figure 5.7)

$$\frac{d}{dt}\int_x u\,dx + \int_s \boldsymbol{n}f\,ds = 0 \tag{5.27}$$

$$\begin{aligned}
x_{i-1/2} &= x_i - \Delta x/2 \\
x_{i+1/2} &= x_i + \Delta x/2 \\
u_{i\pm 1/2} &= u(x_{i\pm 1/2}) \\
f_{i\pm 1/2} &= f(u_{i\pm 1/2})
\end{aligned} \tag{5.28}$$

The conservation equation becomes

$$\frac{d}{dt}(\Delta x \bar{u}_i) + f_{i+1/2} - f_{i-1/2} = 0 \tag{5.29}$$

The cell average of a u is calculated as

$$\bar{u}_i = \frac{1}{\Delta x}\int_{x_{i-1/2}}^{x_{i+1/2}} u(x,t)\,dx \tag{5.30}$$

The Taylor expansion of $u(x)$ is

$$u_x = u_i + \frac{\xi}{1!}\frac{\partial u}{\partial x} + \frac{\xi^2}{2!}\frac{\partial^2 u}{\partial x^2} - \frac{\xi^3}{3!}\frac{\partial^3 u}{\partial x^3} + \cdots \tag{5.31}$$

where

$$\xi = (x - x_i) \tag{5.32}$$

Now

$$\bar{u}_i \;\; = \;\; \frac{1}{\Delta x} \int_{x-\Delta x/2}^{x+\Delta x/2} u(x)dx$$

$$(5.33)$$

$$= \;\; \left[u_i + \frac{\Delta x^2}{24} \frac{\partial^2 u}{\partial x^2} + \frac{\Delta x^4}{1920} \frac{\partial^4 u}{\partial x^4} \right] + O(\Delta x^6) \tag{5.34}$$

Or

$$\bar{u}_i = u_i + O(\Delta x^2) \tag{5.35}$$

If $f = u$,

$$
\begin{aligned}
f^L_{i+1/2} &= \bar{u}_i \\
f^R_{i+1/2} &= \bar{u}_{i+1} \\
f^L_{i-1/2} &= \bar{u}_{i-1} \\
f^R_{i-1/2} &= \bar{u}_i
\end{aligned}
\tag{5.36}
$$

The above expressions lead to discontinuity of fluxes at faces. However, an average will avoid discontinuity, i.e.,

$$\bar{f}_{i+1/2} = \frac{1}{2}\left[f^L_{i+1/2} + f^R_{i+1/2} \right] = \frac{1}{2}[\bar{u}_i + \bar{u}_{i+1}] \tag{5.37}$$

$$\bar{f}_{i-1/2} = \frac{1}{2}\left[f^L_{i-1/2} + f^R_{i-1/2} \right] = \frac{1}{2}[\bar{u}_{i-1} + \bar{u}_i] \tag{5.38}$$

The final dicrete form of Equation 5.27 is

$$\Delta x \frac{d\bar{u}_i}{dt} + \frac{1}{2}(\bar{u}_{i+1} - \bar{u}_{i-1}) = 0 \tag{5.39}$$

Which is a second order central finite difference scheme. However, this is not true for mesh with different cell sizes and for unstructured meshes. In multi-dimensions, both the cell centered (see Figure 5.8) and vertex centered (see Figure 5.9) finite volume methods are commonly used[3].

Two-dimensional approximation

Lets start with the integral form of a scalar equation in two dimensions as

$$\frac{d}{dt} \int_\Omega u d\Omega + \int_s \mathbf{f}.d\mathbf{s} = 0 \tag{5.40}$$

Cell centered approximation

$$\frac{\partial}{\partial t} \int_{\Omega} u d\Omega + \int_{ABCD} (f dy - g dx) = 0 \tag{5.41}$$

$$f_{AB} = \frac{1}{2}(f_A + f_B) \tag{5.42}$$

and

$$f_A = \frac{1}{4}(f_{ij} + f_{i+1,j} + f_{i-1,j+1} + f_{i,j-1}) \tag{5.43}$$

Simplification results in

$$\int_{ABCD} \mathbf{f}.d\mathbf{s} = \frac{1}{2}[(f_A - f_C)\Delta y_{DB} + (f_B - F_D)\Delta y_{AC} - (g_A - g_C)\Delta x_{DB} - (g_B - g_D)\Delta_{AC}] \tag{5.44}$$
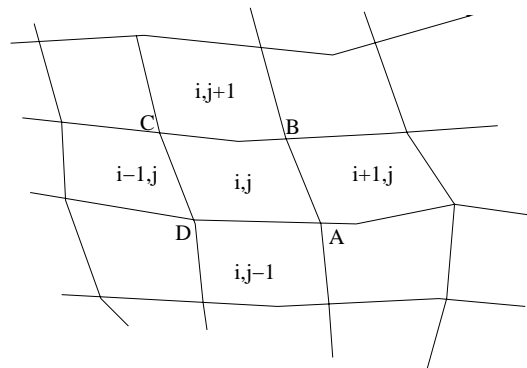
Figure 5.8: Cell centered finite volume method.
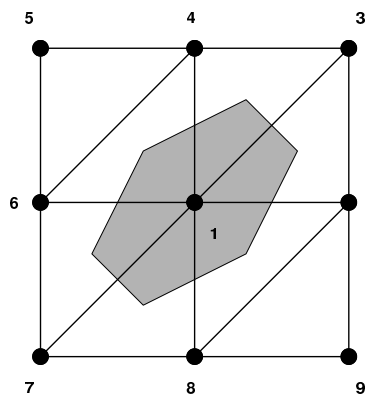
Figure 5.9: Vertex centered finite volume method.

5.2.3   Finite Element Method

The finite element method originated from the field of structural analysis as a result of many years of research, mainly between 1940 and 1960. The concept of 'elements' can be traced back to the techniques used in stress calculations, whereby a structure was subdivided into small substructures of various shapes and re-assembled after each 'element' had been analysed. The development of this technique and its formal elaboration led to the introduction of what is now called the finite element method.

The most widely used weighted residual form of the finite element method is the Galerkin method, in which the weighting functions are taken equal to the interpolation function $N_I(x)$. This is also called the Bubnov-Galerkin method, to be distinguished from the Petrov-Galerkin method, in which the test functions are different from the interpolation function N_I. The weighted residual form of a typical differential equation may be written as[1, 5, 6]

$$\int W \left[\frac{\partial \hat{U}}{\partial t} + \frac{\partial \hat{F}}{\partial x} + \frac{\partial \hat{G}}{\partial x} \right] dx = 0 \tag{5.45}$$

The weights W are related to the approximating functions (shape functions or trail functions) of the system.
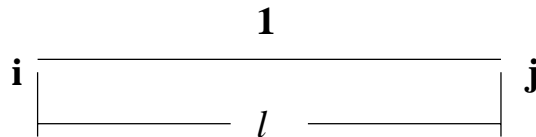
Figure 5.10: One-dimensional finite element.

The spatial discretization of linear one-dimensional finite element may be carried out for a function φ is as (see Figure 5.10)

$$\varphi = N_i \varphi_i + N_j \varphi_j \tag{5.46}$$

where

$$N_i = \frac{x_j - x}{x_j - x_i}; N_j = \frac{x - x_i}{x_j - x_i} \tag{5.47}$$

Note the following properties of approximating or shape functions.

$$N_i + N_j = 1 \tag{5.48}$$

at node i, $N_i = 1$, $N_j = 0$ at node j, $N_i = 0$, $N_j = 1$

Derivatives of the shape functions are constants over the element for linear approximation. The weighted residual form can now be rewritten as

$$\int \{\mathbf{N}\} \left[\frac{\partial \hat{\mathbf{U}}}{\partial \mathbf{t}} + \left[\frac{\partial \mathbf{N}}{\partial \mathbf{x}} \right] \{\mathbf{F}\} + \left[\frac{\partial \mathbf{N}}{\partial \mathbf{x}} \right] \{\mathbf{G}\} \right] \mathbf{dx} = \mathbf{0} \tag{5.49}$$

Element by element system may now be constructed by substituting

$$\mathbf{N} = \left\{ \begin{array}{c} N_1 \\ N_2 \end{array} \right\}; \quad \mathbf{F} = \left\{ \begin{array}{c} F_1 \\ F_2 \end{array} \right\}; \quad \mathbf{G} = \left\{ \begin{array}{c} G_1 \\ G_2 \end{array} \right\} \tag{5.50}$$

and

$$\left[\frac{\partial \mathbf{N}}{\partial \mathbf{x}} \right] = \left[\begin{array}{cc} \frac{\partial N_1}{\partial x} & \frac{\partial N_2}{\partial x} \end{array} \right] \tag{5.51}$$

The elemental equations must be assembled before writing the set of simultaneous equations. Some useful integration formulae for linear approximation are:
One-dimension

$$\int_\Omega N_1^a N_2^b d\Omega = \frac{a! b! l}{(a+b+1)!} \tag{5.52}$$

where l is the length of an element.
Two-dimensions-triangular elements

$$\int_\Omega N_1^a N_2^b N_3^c d\Omega = \frac{a! b! c! 2A}{(a+b+c+2)!} \tag{5.53}$$

where A is the area of a triangular element.

5.2.4   Boundary Conditions

1. *Dirichlet boundary condition:* The value of the function is given on a boundary. Implementation of Dirichlet condition is direct.
2. *Neumann boundary condition:* The flux or gradient is given on a boundary.

5.3   Temporal Discretization

The transient terms of any equation can be discretized using the same principles as spatial discretization. By suitably adjusting the time levels in space, different numerical schemes can be created. In order to demonstrate various time discretization techniques, consider the following one dimensional, transient heat conduction equation

$$\rho c_p \frac{\partial T}{\partial t} - \frac{\partial}{\partial x} \left(k \frac{\partial T}{\partial x} \right) = 0 \tag{5.54}$$

where ρ is the density of material, c_p is the specific heat of the material, T is the temperature, t is the time and k is the thermal conductivity of the material. Figure 5.12 shows a typical temperature variation in time and possible time discretization methods.
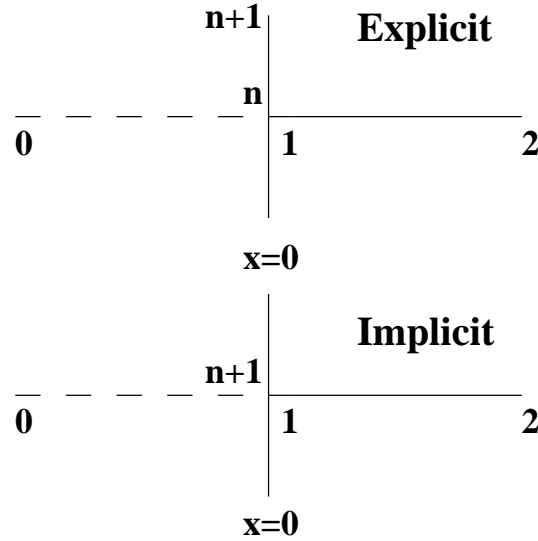
Figure 5.11: Neumann boundary conditions.

5.3.1 Explicit Methods

Let us assume the thermal conductivity in the above equation is constant and the spatial term is discretized using central difference method. We therefore get a discrete form as

$$\rho c_p \frac{\Delta T}{\Delta t} = k \frac{u_{i+2} - u_i - u_{i+1} - u_{i-1}}{2\Delta x^2} \tag{5.55}$$

With reference to Figure 5.12 we can write a simple forward difference for ΔT as

$$\Delta T = T^{n+1} - T^n \tag{5.56}$$

Where $n + 1$ (unknown) and n (known) indicate different time levels at an interval of Δt. Substituting into Equation 5.55

$$\rho c_p \frac{T^{n+1} - T^n}{\Delta t} = k \frac{u_{i+2} - u_i - u_{i+1} - u_{i-1}}{2\Delta x^2} \tag{5.57}$$

Now the question to be answered is at what time level the RHS should be considered. If we consider the RHS to be at nth time level (known), the method is called *explicit*.

5.3.2 Semi-implicit Methods

If we take

$$f = k \frac{u_{i+2} - u_i - u_{i+1} - u_{i-1}}{2\Delta x^2} \tag{5.58}$$

and define

$$f^{n+\theta} = \theta f^{n+1} + (1 - \theta) f^n \tag{5.59}$$
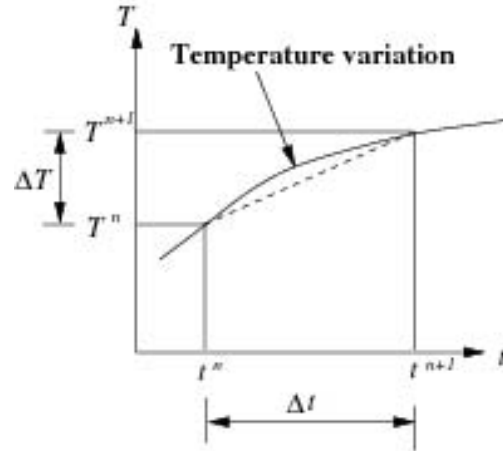
Figure 5.12: Time discretization

we can rewrite Equation 5.57 as

$$\rho c_p \frac{T^{n+1} - T^n}{\Delta t} = f^{n+\theta} \tag{5.60}$$

If $\theta = 0$, we get the explicit scheme discussed in the previous section. If we take $\theta = 0.5$, the scheme is called *semi-implicit*.

5.3.3   Fully- Implicit Methods

In Equation 5.60 if $\theta = 1$, the scheme is implicit.

5.4   Some Numerical Algorithms

In the previous sections, we discussed various spatial and temporal discretization methods. Here, we discuss some discretization algorithms, i.e., combination of spatial and temporal discretizations for different differential equations.

5.4.1   Convection and Convection-diffusion equations

A linear convection equation of the type

$$\frac{\partial \varphi}{\partial t} + u \frac{\partial \varphi}{\partial x} = 0 \tag{5.61}$$

is often used in biofluid mechanics and computational fluid dynamics to understand various discretization schemes. In the above equation u is the velocity and assumed to be independent of φ. The so called forward in time and central in space (FTCS) scheme in its explicit form may be written using FDM as

$$\frac{\varphi_i^{n+1} - \varphi_i^n}{\Delta t} + u\frac{\varphi_{i+1}^n - \varphi_{i-1}^n}{2\Delta x} = 0 \tag{5.62}$$

This equation is unconditionally unstable, i.e., this scheme will not produce any solution for φ at any circumstance. Thus, it is essential to avoid such schemes. The instability is developed by the negative dissipation added by the discretization[2]. Addition of the real diffusion to the equation in its discrete form is sufficient to avoid instability until a quantity referred to as Peclet number (Pe) is below unity. For convection dominated flows (flow at very high velocities) however natural diffusion alone is not sufficient. The FTCS discretization for a convection-diffusion equation is

$$\frac{\varphi_i^{n+1} - \varphi_i^n}{\Delta t} + u\frac{\varphi_{i+1}^n - \varphi_{i-1}^n}{2\Delta x} - \nu\frac{\varphi_{i+1}^n - 2\varphi_i^n + \varphi_{i-1}^n}{\Delta x^2} = 0 \tag{5.63}$$

where ν is the diffusion coefficient. The Peclet number is defined as

$$Pe = \frac{lu}{2\nu} \tag{5.64}$$

where l is the element length (length between nodes i and $i+1$). As long as $Pe < 1$ the above equation gives a stable solution. If natural diffusion is not available, an artificial diffusion k may replace ν. However, such an artificial diffusion can be naturally derived using the method called Lax-Wendroff scheme. If natural diffusion ν is not available, a Lax-Wendroff scheme may be used to solve a convection equation. The Lax-Wendroff scheme for convection equation may be obtained by replacing ν with $\Delta t u^2/2$. Note that the Lax-Wendroff coefficient has a dimension of m^2/s, same as a diffusion coefficient. The Lax-Wendroff scheme may be written as

$$\frac{\varphi_i^{n+1} - \varphi_i^n}{\Delta t} + u\frac{\varphi_{i+1}^n - \varphi_{i-1}^n}{2\Delta x} - \frac{\Delta t u^2}{2}\frac{\varphi_{i+1}^n - 2\varphi_i^n + \varphi_{i-1}^n}{\Delta x^2} = 0 \tag{5.65}$$

The Peclet number condition discussed above is very much linked to the limit on Δt. The diffusion time step may be derived by writing $\Delta t u^2/2 = \nu$. The wave speed u is normally limited to one element or segment of a spatial discretization. Such limitation, in addition to giving accurate solution, it will also provide stable solution, i.e., by writing $u = l/\Delta t$, we can maintain stability of a Lax-Wendroff scheme. Alternatively, we can say the Courant-Friedrichs-Lewy(CFL) number $\frac{\Delta t u}{l}$ must be maintained below unity. Using this definition, we can also derive diffusion limit as

$$\frac{\Delta t}{2}\frac{l^2}{\Delta t^2} = \nu \tag{5.66}$$

or

$$\Delta t = \frac{l^2}{2\nu} \tag{5.67}$$

In practice,

$$\Delta t = min\left(\frac{l}{u}, \frac{l^2}{2\nu}\right) \tag{5.68}$$

works well. There are many other methods available to solve both scalar and vector equations[2, 5]. Describing all these methods is not within the scope of this text. Some solution procedures for vector valued problems and the Navier-Stokes equations are described in the following chapters.

5.5   Summary

This chapter introduced the basics of numerical methods. In addition to spatial and temporal discretizations, the principles of algorithm development were also briefly discussed. For more details on various CFD schemes, readers are referred to the text books listed in this chapter.

Bibliography

[1] R.W. Lewis, P. Nithiarasu, and K.N. Seetharamu. *Fundamentals of the Finite Element Method for Heat and Fluid Flow*. Wiley, Chiester, 2004.

[2] C.A.J. Fletcher. *Computational techniques for fluid dynamics, Volume 1 Fundamentals and general techniques*. Springer Verlag, 1988.

[3] C. Hirsch. *Numerical computation of internal and external flows, Volumes 1 and 2*. John Wiley and Sons, 1989.

[4] J.C. Tannehill, D.A. Anderson, and R.H. Pletcher. *Computational Fluid Mechanics and Heat Transfer*. Taylor and Francis, 1997.

[5] O.C. Zienkiewicz, R.L. Taylor, and P. Nithiarasu. *The finite element method for fluid dynamics*. Elsevier Butterworth-Heinemann, Elsevier Butterworth-Heinemann, Burlinton, MA, 2005.

[6] J. Donea and A. Huerta. *Finite Element Method for Flow Problems*. Wiley, 2003.

Chapter 6

Numerical Modelling of Wave Propagation

6.1 Introduction

This chapter is dedicated to one-dimensional numerical modelling of wave propagation through arterial networks. One-dimensional modelling is becoming a useful tool for gaining a better understanding of blood flow in the arterial circulation and how it is affected by various interventions or diseases[1]. At present, 3D modelling of the entire arterial tree is not feasible. Apart from the unavailability of precise information regarding 3D geometry and material properties, the computational time required to model such an extensive network of branching vessels, including the fluid-structure interaction between blood and vessel walls, is simply too great. However, it has long been recognized that since the wavelengths of the pressure-flow waves produced by the heart are much greater than the diameter of the vessels, it is valid to consider flow to be quasi one-dimensional[2]. The one-dimensional equations of flow may be expressed in terms of vessel cross-sectional area A, velocity u and pressure p. Pressure is related to A via the chosen non-linear elastic wall law (i.e. $p = p(A)$). There are indeed several to choose from (for example see [3]) which reflects the fact that the wall law is an empirical and/or mathematical simplification of the true mechanics of vessel walls, which are anisotropic and not perfectly cylindrical. It is also well-known that the arterial wall is a visco-elastic material and thus pressure is determined not only by A but its derivatives also, although these effects are generally considered small enough to be ignored [4]. Another consideration is the treatment of blood viscosity. While various approximations have been used [5], most authors [6] calculate its effects in 1D by using an assumption of fully-developed Newtonian steady flow with a parabolic velocity profile over a given cross-section (Poiseuille flow).

6.2 One-Dimensional Equations

The one-dimensional equations governing the cross sectional area of cylindrical vessels and velocity may be derived by simplifying the general continuity and momentum equations. The general one-dimensional continuity equation that incorporates the cross sectional area may be written as

$$\frac{\partial(\rho A)}{\partial t} + \frac{\partial(\rho A u)}{\partial x} = 0 \tag{6.1}$$

where (A) is the cross-sectional area and (u) is the mean velocity over a cross-section. Simplifying the above equation for incompressible flows (constant density ρ) and writing the momentum equation also in one-dimension, we get the set of governing equations for modelling one-dimensional fluid-structure interaction in arterial networks. The equations are written as

$$\frac{\partial A}{\partial t} + \frac{\partial (Au)}{\partial x} = 0 \tag{6.2}$$

and

$$\frac{\partial u}{\partial t} + u\frac{\partial u}{\partial x} + \frac{1}{\rho}\frac{\partial p}{\partial x} - \frac{1}{\rho}\frac{\partial \tau}{\partial x} = 0 \tag{6.3}$$

where p is the internal pressure, $\rho \approx 1060$ kg/m^3 is blood density, assumed constant for blood which is essentially incompressible, and $\tau = \mu(\frac{\partial u}{\partial r})|_R$ is the shear stress, where μ is viscosity (approximately 0.035 poise for blood), r is the radial direction in three-dimensional cylindrical coordinates, and R is the vessel radius.

There are viscous and inertial components to the shear stress term [7], and these are proportional to u and du/dt respectively. However, it is common to ignore the inertial component which is relatively insignificant at low values of the Womersley parameter[8] $\alpha = R\sqrt{\omega\rho/\mu}$ where ω is the angular frequency of a given harmonic. For example, the inertial component would be most significant in a large artery (say $R = 1.7$cm) with a high frequency oscillation. Various formulations for the viscous resistance are possible and the field of *blood rheology* is a complex one [9]. However, in the major arteries, flow is often considered to be laminar and the expression for Poiseuille flow, which assumes fully developed ($\frac{\partial u}{\partial x} = 0$), steady ($\frac{\partial u}{\partial t} = 0$) flow, is used as follows:

$$\frac{d\tau}{dx} = \frac{8\mu Q}{\pi R^4} = \frac{8\pi\mu u}{A} \tag{6.4}$$

where $Q = Au$ is the volume flow rate. This expression will not be valid in arterioles or capillaries where flow is non-Newtonian (when the size of red blood cells becomes significant compared to vessel diameter) nor when flow is turbulent[10], which may occur in some disease states [11]. Incorporating Eq.(6.4) into Eqs.(6.2) and (6.3), the coupled system of equations governing blood flow can be expressed in conservation form:

$$\frac{\partial \mathbf{U}}{\partial t} + \frac{\partial \mathbf{F}}{\partial x} = \mathbf{S} \tag{6.5}$$

where
$$\mathbf{U} = \begin{bmatrix} A \\ u \end{bmatrix}, \mathbf{F} = \begin{bmatrix} uA \\ \frac{u^2}{2} + \frac{p}{\rho} \end{bmatrix} \text{ and } \mathbf{S} = \begin{bmatrix} 0 \\ -8\pi\mu\frac{u}{A} \end{bmatrix}$$

Since there are three variables, a third equation is required to close the system. This constitutive equation describes how vessel area varies with pressure and thus deals with the fluid-structure interaction of the problem. Many different relations have been used in the past and may be categorised as linear elastic models [4], where pressure is linearly related to area; non-linear elastic models [12] where this relation is non-linear; collapsible tube models [10], where special effort is made to accommodate tubes that can collapse as well as distend; and visco-elastic models [13], which account for the viscoelasticity of the vessel wall. While the visco-elastic models are the most complete, they are also the most complicated. Since the effects of wall viscosity are generally

assumed to be small, a non-linear elastic relation is usually sufficient. The most common relation used in studies of this type is that used by Formaggia[14] and others and is written here as

$$p = p_{ext} + \beta \left(\sqrt{A} - \sqrt{A_0} \right) \tag{6.6}$$

where p_{ext} is the external pressure from surrounding tissue, A_0 is the area when there is zero transmural pressure (i.e. $p = p_{ext}$) and β accounts for the material properties of the elastic vessel (although it should be noted that A_0 also appears):

$$\beta = \frac{\sqrt{\pi} h E}{A_0 (1 - \sigma)^2} \tag{6.7}$$

where h is the vessel wall thickness, E is Young's Modulus and σ is the Poisson ratio, assumed to be 0.5 (i.e. the vessel wall is incompressible). All of these parameters are assumed to be independent of transmural pressure. Note that the Eq.(6.6) may be rewritten in terms of wave speed as follows:

$$p = p_{ext} + 2\rho c^2 \left(1 - \sqrt{\frac{A_0}{A}} \right) \tag{6.8}$$

The intrinsic wave speed of a vessel is related to β via

$$c_0 = \sqrt{\frac{\beta \sqrt{A_0}}{2\rho}} = \sqrt{\frac{hE}{2\rho R_0 \left(1 - \sigma^2 \right)}} \tag{6.9}$$

where the second expression is called the Moens-Korteweg equation (with $A_0 = \pi R_0^2$) and relates the material properties of the vessel to its intrinsic wave speed, that is, the speed at which an infinitesimally small pulse would propagate in an *initially unstressed* (i.e. $A(t = 0) = A_0$ everywhere) vessel. Infinitesimally small pulses in *initially stressed* (i.e. $A(t = 0) = A$ everywhere) vessels propagate at a slightly higher wave speed,

$$c = \sqrt{\frac{\beta \sqrt{A}}{2\rho}} \tag{6.10}$$

Note that finite amplitude pulses do not propagate at a speed c, but at $|u + c|$, as will be discussed later. As a consequence, the peak of a pressure wave propagates faster than its foot which would inevitably lead to shock formation (where the peak catches up with the foot) in a long enough tube. However, shocks generally do not form in the real arterial system since the frequency of the pulses and the length of the vessels are too low.

6.3 The Characteristic System

The system of equations Eq.(6.5) is non-linear and highly coupled, making direct analytical solutions impossible. Thus, a numerical solution is required. However when implementing the numerical solution, it is useful to have available a linearised de-coupled form of the equations which can be used when applying boundary conditions. The system is first written in quasi-linear

form, which is then used to derive the characteristic system. By taking the spatial derivative of Eq.(6.6)

$$\frac{\partial p}{\partial x} = \frac{\partial p_{ext}}{\partial x} + \frac{\beta}{2\sqrt{A}}\frac{\partial A}{\partial x} - \frac{\beta}{2\sqrt{A_0}}\frac{\partial A_0}{\partial x} + \left(\sqrt{A} - \sqrt{A_0}\right)\frac{\partial \beta}{\partial x} \tag{6.11}$$

the number of independent variables in the momentum equation can be reduced to two by replacing $\frac{\partial p}{\partial x}$ with Eq.(6.11). Using Eq.(6.5), the quasi-linear form is

$$\frac{\partial \mathbf{U}}{\partial t} + \mathbf{H}\frac{\partial \mathbf{U}}{\partial x} = \mathbf{C} \tag{6.12}$$

where

$$\mathbf{U} = \begin{bmatrix} A \\ u \end{bmatrix}, \mathbf{H} = \begin{bmatrix} u & A \\ \frac{\beta}{2\rho\sqrt{A}} & u \end{bmatrix},$$

$$\mathbf{C} = -\frac{1}{\rho}\begin{bmatrix} 0 \\ 8\pi\mu\frac{u}{A} + \frac{\partial p_{ext}}{\partial x} - \frac{\beta}{2\sqrt{A_0}}\frac{\partial A_0}{\partial x} + \left(\sqrt{A} - \sqrt{A_0}\right)\frac{\partial \beta}{\partial x} \end{bmatrix}$$

The eigenvalues ($\mathbf{\Lambda}$) of Eq.(??) are given by $|\mathbf{\Lambda I} - \mathbf{H}| = 0$ [15]. For physiological flows, $u < c$, so there are two real eigenvalues and the system is hyperbolic.

$$\mathbf{\Lambda} = \begin{bmatrix} \lambda_1 \\ \lambda_2 \end{bmatrix} = u \pm \sqrt{\frac{\beta\sqrt{A}}{2\rho}} = \begin{bmatrix} u + c \\ u - c \end{bmatrix} \tag{6.13}$$

The set of left eigenvectors ($\mathbf{l}_i$) are first found by solving the equation $\mathbf{l}_i\mathbf{H} = \lambda_i\mathbf{l}_i$, which leads to the left eigenmatrix

$$\mathbf{L} = \begin{bmatrix} \mathbf{l}_1^T \\ \mathbf{l}_2^T \end{bmatrix} = \begin{bmatrix} c/A & 1 \\ -c/A & 1 \end{bmatrix} \tag{6.14}$$

Noting that $\mathbf{LHL}^{-1} = \Lambda$, pre-multiplying Eq.(6.14) by $\mathbf{L}$ gives (in component form, $i = 1, 2$)

$$\mathbf{l}_i\frac{\partial \mathbf{U}}{\partial t} + \lambda_i\mathbf{l}_i\frac{\partial \mathbf{U}}{\partial x} + \mathbf{l}_i\mathbf{C} = 0 \tag{6.15}$$

Then the characteristic variables are defined by

$$dw_i = \left(\mathbf{l}_i\frac{d\mathbf{U}}{dt} + \mathbf{l}_i\mathbf{C}\right)dt \tag{6.16}$$

If this relation is integrable[16], the characteristic system can be expressed as

$$\frac{\partial w_i}{\partial t} + \lambda_i\frac{\partial w_i}{\partial x} = 0 \tag{6.17}$$

To make the characteristic system applicable near the boundaries, the spatial derivatives of β, A_0 and p_{ext} are assumed to be zero, and if viscous resistance is small, then $\mathbf{C} \approx 0$ and the following expression can be integrated:

$$dw_{1,2} = du \pm \sqrt{\frac{\beta}{2\rho}} A^{-3/4} dA \tag{6.18}$$

where the expression for c has been substituted from Eq.(6.10). When $\mathbf{C} = 0$ the characteristic variables are constant along the characteristic lines defined by $\frac{dx}{dt} = \lambda$ (Riemann invariants) which, upon integration, are

$$\begin{bmatrix} w_1 \\ w_2 \end{bmatrix} = \begin{bmatrix} u + 4c \\ u - 4c \end{bmatrix} \tag{6.19}$$

Finally, the primitive variables can be calculated from the characteristic variables by adding or subtracting the two equations in Eq.(6.19), giving

$$A = \frac{(w_1 - w_2)^4}{1024} \left(\frac{\rho}{\beta} \right)^2 \tag{6.20}$$

$$u = \tfrac{1}{2} \left(w_1 + w_2 \right) \tag{6.21}$$

The physical interpretation of the characteristic system is that pressure and velocity *wavefronts* propagate forwards (by convention, away from the heart) at a speed of $u+c$ and backwards (towards the heart) at $u - c$. A wavefront may be considered to be a particular point on a pulse [17] (for example, the peak or the foot). Throughout this work, the terms 'wave' or 'pulse' refer to a finite amplitude, finite duration change in pressure and velocity, while a 'wavefront' strictly refers to an infinitesimal change in one of the characteristic variables, w_1 or w_2. Forward-running wavefronts are initially generated by the contraction of the heart which squeezes blood into the aorta. These wavefronts, which compose the forward-running pressure pulse, then propagate throughout the entire arterial tree. At branching points or whenever there is a change in vessel properties, the wavefronts are reflected and travel back towards the heart. These may re-reflect before reaching the heart, and thus the pressure and flow measured at any point in the arterial system may be explained as the combination of many forward and backward-running wavefronts.

6.4   Boundary Conditions

There are two ways of prescribing boundary conditions. *Reflecting* boundary conditions are achieved by simply prescribing the desired values of pressure, area or velocity. However this results in total negative reflection of any backward-travelling waves. Such reflections are not physiological since they would only occur where there is a sudden and very large increase in characteristic admittance (i.e. a tube that opens to an infinite cavity). In contrast, *non-reflecting* boundary conditions involve prescribing the *forward component* of pressure, area or velocity at the inlet. Then any backward waves pass through the boundary without reflection, simulating the case where the vessel extends uniformly beyond the boundary. This approach is more intuitive since information arising from inside the computational domain (backward components) is combined with information from outside the domain (prescribed forward components) to yield total values at the boundary.

The characteristic system is useful for calculating non-reflecting boundary conditions since it is expressed in terms of variables that are associated with forward (w_1) and backward-travelling

(w_2) wavefronts. Thus specifying boundary conditions becomes a matter of specifying the incoming wavefront (which can only arise from outside the computational domain) and predicting the effects of the outgoing wavefront on the boundary node (which cannot be affected by phenomena outside of the computational domain).

Since $u < c$, $\lambda_1 > 0$ and $\lambda_2 < 0$ (i.e. the system is subsonic), and so one boundary condition must be specified at both the inlet and outlet. In both cases, the outgoing characteristic may be calculated via linear extrapolation in the $x - t$ plane, where for the next time step $n + 1$,

$$w_2^{n+1}\big|_{x=x_0} = w_2^n\big|_{x=x_0-\lambda_2^n \Delta t} \tag{6.22}$$

and

$$w_1^{n+1}\big|_{x=x_L} = w_1^n\big|_{x=x_L-\lambda_1^n \Delta t} \tag{6.23}$$

at the inlet and outlet respectively, where x_0 and x_L are the coordinates of the inlet and outlet.

In general, prescribing area, pressure or velocity on a boundary node is achieved by simply setting the appropriate value on the boundary node after all other nodal values have been calculated. At the inlet, the non-prescribed variable can be calculated from the outgoing characteristic via Eq.(6.22) and Eq.(6.19), while the prescribed variable can be assigned directly. To prescribe area at the inlet,

$$\begin{aligned} A_{in}^{n+1} &= \bar{A}^{n+1} \\ u_{in}^{n+1} &= w_2^{n+1} + 4\bar{A}^{n+1}\sqrt{\frac{\beta}{2\rho}} \end{aligned} \tag{6.24}$$

where the over-bar represents a prescribed value, and the subscript in refers to the inlet node. To prescribe pressure at the inlet,

$$\begin{aligned} A_{in}^{n+1} &= \left(\frac{\bar{p}^{n+1}-p_{ext}}{\beta} + \sqrt{A_0}\right)^2 \\ u_{in}^{n+1} &= w_2^{n+1} + 4A_{in}^{n+1}\sqrt{\frac{\beta}{2\rho}} \end{aligned} \tag{6.25}$$

To prescribe velocity at the inlet,

$$\begin{aligned} A_{in}^{n+1} &= \frac{\left(\bar{u}^{n+1}-w_2^{n+1}\right)^4}{64}\left(\frac{\rho}{\beta}\right)^2 \\ u_{in}^{n+1} &= \bar{u}^{n+1} \end{aligned} \tag{6.26}$$

Similar expressions can readily be obtained for prescribing values at the outlet.

Prescribing the *forward* component of a variable can be achieved by prescribing the incoming characteristic (w_1) [18]. The actual values assigned to both A_{in} and u_{in} are determined at run time based on the prescribed incoming characteristic and the current value of the outgoing characteristic (from Eq.(6.22)) which is not known *a priori*.

Thus to prescribe forward area, rearrange (6.20) to give

$$w_{1in}^{n+1} = w_2^0 + 8\left(\bar{A}^{n+1}\right)^{1/4}\sqrt{\frac{\beta}{2\rho}} \tag{6.27}$$

To prescribe forward pressure, substitute (6.25) into (6.27)

$$w_{1in}^{n+1} = w_2^0 + 4\sqrt{\frac{2}{\rho}}\sqrt{(\bar{p}^{n+1} - p_{ext}) + \beta\sqrt{A_0}} \tag{6.28}$$

Finally, forward velocity may be prescribed by rearranging (6.21)

$$w_{1in}^{n+1} = 2\bar{u}^{n+1} - w_2^0 \tag{6.29}$$

In these equations, w_2^0 is the initial value of w_2 and is also equal to the value of w_2 at any time if no backward-running waves reach the inlet.

6.5 Solution Methods

Standard Galerkin discretisation of Eq.(6.5) leads to spatial instability due to the presence of the convective term. One possible way of achieving better spatial stability is by including the Taylor-Galerkin stabilisation, which is the finite element equivalent of Lax-Wendroff stabilisation for the finite difference method, and also gives a second order time accuracy. Derivation of the Taylor-Galerkin discretisation for the A, Q system has been performed by Formaggia, Sherwin and co-workers [18, 19] and is the same for the A, u system. For completeness it is included here. Eq.(6.5) can be rearranged to give

$$\frac{\partial \mathbf{U}}{\partial t} = \mathbf{S} - \frac{\partial \mathbf{F}}{\partial x} \tag{6.30}$$

where $\mathbf{U}$, $\mathbf{F}$ and $\mathbf{S}$ are the vectors of primitive variables, conservative variables and source term respectively.

Differentiating with respect to time and applying the chain rule,

$$\frac{\partial^2 \mathbf{U}}{\partial t^2} = \mathbf{S_U}\frac{\partial \mathbf{U}}{\partial t} - \frac{\partial}{\partial x}\left(\mathbf{F_U}\frac{\partial \mathbf{U}}{\partial t}\right) \tag{6.31}$$

where $\mathbf{F_U} = \frac{\partial \mathbf{F}}{\partial \mathbf{U}}$ ($= \mathbf{H}$ in Eq.(??)) and $\mathbf{S_U} = \frac{\partial \mathbf{S}}{\partial \mathbf{U}}$. Substituting Eq.(6.31) into Eq.(6.30) removes the time derivatives from the right-hand side.

$$\frac{\partial^2 \mathbf{U}}{\partial t^2} = \mathbf{S_U}\left(\mathbf{S} - \frac{\partial \mathbf{F}}{\partial x}\right) - \frac{\partial (\mathbf{F_U}\mathbf{S})}{\partial x} + \frac{\partial}{\partial x}\left(\mathbf{F_U}\frac{\partial \mathbf{F}}{\partial x}\right) \tag{6.32}$$

The Taylor series expansion in time is

$$\mathbf{U}^{n+1} = \mathbf{U}^n + \Delta t\frac{\partial \mathbf{U}^n}{\partial t} + \frac{\Delta t^2}{2}\frac{\partial^2 \mathbf{U}^n}{\partial t^2} + O\left(\Delta t^3\right) \tag{6.33}$$

where Δt is the time step and n refers to the current time step. Ignoring 3rd and higher order terms, and substituting Eq.(6.30) and Eq.(6.32) yields the final explicit semi-discrete form:

$$\frac{\mathbf{U}^{n+1} - \mathbf{U}^n}{\Delta t} = \mathbf{S}^n - \frac{\partial \mathbf{F}^n}{\partial x} - \frac{\Delta t}{2}\left[\frac{\partial}{\partial x}\left(\mathbf{F_U^n}\mathbf{S}^n - \mathbf{F_U^n}\frac{\partial \mathbf{F}^n}{\partial x}\right) - \mathbf{S_U^n}\frac{\partial \mathbf{F}^n}{\partial x} - \mathbf{S_U^n}\mathbf{S}^n\right] \tag{6.34}$$

Note that the second bracketed term is the Taylor-Galerkin stabilisation term.

6.5.1   Global Taylor-Galerkin Method

The standard spatial discretisation for the finite element method is performed over the global domain Ω which has boundaries denoted by Γ. Galerkin weighting $\mathbf{N}^T$ along with a linear spatial discretisation provides a residual equation which converges to the exact solution when the element size approaches zero, that is,

$$\int_{\Omega} \left(\mathbf{N}^T \frac{\Delta \hat{\mathbf{U}}^n}{\Delta t} - \mathbf{N}^T \hat{\mathbf{R}}^n \right) d\Omega = 0 \tag{6.35}$$

where $\mathbf{R}$ is the right-hand side of Eq.(6.34). The hat signifies that these variables are approximated by the finite element method, where for any variable $\mathbf{\Phi}$, for example, $\hat{\mathbf{\Phi}} = N_i \tilde{\Phi}_i + N_j \tilde{\Phi}_j = \mathbf{N}\tilde{\mathbf{\Phi}}$ means that the value of $\hat{\mathbf{\Phi}}$ anywhere in a given one-dimensional element is interpolated between two discrete nodes (i, j) with nodal values $\tilde{\Phi}_{i,j}$ via the linear interpolation functions $N_i = (x_j - x)/(x_j - x_i)$ and $N_j = (x - x_i)/(x_j - x_i)$. Evaluation of Eq.(6.35) results in the following equation in compact matrix form:

$$[\mathbf{M}] \{\Delta \mathbf{U}\} = \Delta t \left([\mathbf{K}] \{\mathbf{F}\}^n + [\mathbf{L}] \{\mathbf{S}\}^n + \{\mathbf{f}_\Gamma\}^n \right) \tag{6.36}$$

where $[\mathbf{M}]$ is called the mass matrix and $[\mathbf{K}]$ and $[\mathbf{L}]$ are coefficient matrices for convection, Taylor-Galerkin and source terms; each of these are $N_{nodes} \times N_{nodes}$ matrices, where N_{nodes} is the number of nodes in Ω. Also, $\Delta \mathbf{U} = \mathbf{U}^{n+1} - \mathbf{U}^n$ and $\mathbf{f}$ contains boundary fluxes. On internal nodes these fluxes are usually ignored for the Global Galerkin method (thus $\mathbf{f} = \mathbf{f}_\Gamma$), since the flux contributions from the two adjoining elements exactly cancel. While this not so on boundaries, this term is still not used since Dirichlet boundary conditions are set explicitly (see section 6.4).

6.5.2   Locally Conservative Taylor-Galerkin Method

The Locally Conservative Galerkin (LCG) method is a technique introduced by Thomas and Nithiarasu [20, 21, 22] which treats each element as a sub-domain with its own boundaries. In this case Eq.(6.36) is written over an elemental sub-domain (Ω_e):

$$[\mathbf{M}_e] \{\Delta \mathbf{U}\} = \Delta t \left([\mathbf{K}_e] \{\mathbf{F}\}^n + [\mathbf{L}_e] \{\mathbf{S}\}^n + \{\mathbf{f}_{\Gamma_e}\}^n \right) \tag{6.37}$$

Now $[\mathbf{M_e}]$, $[\mathbf{K_e}]$ and $[\mathbf{L_e}]$ are 2x2 matrices, and this system of equations is solved on individual elements, independent of surrounding elements. Information is transmitted between elements via the flux term which is imposed as a Neumann boundary condition. It can be shown that the LCG method is equivalent to the Global Galerkin method for convection-diffusion type problems except on global boundaries [21]. One advantage of LCG method is that only small equations need to be solved; for one-dimensional problems, the 2x2 matrices can be evaluated directly before coding, which removes the need for any matrix inversions. For brevity, only the derivation for the inviscid case will be considered, which is achieved by removing all terms involving $\mathbf{S}$ and $\mathbf{S_U}$. This reduced form is as follows:

$$\int_{\Omega_e} \mathbf{N}^T \frac{\Delta \hat{\mathbf{U}}^n}{\Delta t} = -\int_{\Omega_e} \mathbf{N}^T \frac{\partial \hat{\mathbf{F}}^n}{\partial x} + \frac{\Delta t}{2} \int_{\Omega_e} \mathbf{N}^T \frac{\partial}{\partial x} \left(\hat{\mathbf{F}}_{\mathbf{U}}^n \frac{\partial \hat{\mathbf{F}}^n}{\partial x} \right) d\Omega_e = 0 \tag{6.38}$$

The time integral is treated in the usual way [23] resulting in the element mass matrix

$$[\mathbf{M}_e] = \frac{l_e}{6} \begin{bmatrix} 2 & 1 \\ 1 & 2 \end{bmatrix} \tag{6.39}$$

where l_e is the element length. The lumped mass matrix may also be used,

$$[\mathbf{M}_e] = \frac{l_e}{2} \begin{bmatrix} 1 & 0 \\ 0 & 1 \end{bmatrix} \tag{6.40}$$

While the lumped mass matrix is sometimes considered undesirable for transient problems, we can demonstrate that there is negligible difference when comparing consistent and lumped mass matrices[1]. Thus, in what follows, the lumped mass matrix has been used since it is somewhat more efficient. The convection term is integrated by parts,

$$-\int_{\Omega_e} \mathbf{N}^T \frac{\partial \hat{\mathbf{F}}^n}{\partial x} d\Omega_e = \int_{\Omega_e} \frac{\partial \mathbf{N}^T}{\partial x} \hat{\mathbf{F}}^n d\Omega_e - \int_{\Gamma_e} \mathbf{N}^T \hat{\mathbf{F}}^n \mathbf{n} d\Gamma_e \tag{6.41}$$

where $\hat{\mathbf{F}}$ is computed in a small post-processing step as the average value of $\mathbf{F}$ from adjacent elements. Similarly the Taylor-Galerkin term is integrated by parts,

$$\int_{\Omega_e} \mathbf{N}^T \frac{\partial}{\partial x} \left(\mathbf{F}_{\mathbf{U}}^n \frac{\partial \hat{\mathbf{F}}^n}{\partial x} \right) d\Omega_e = -\int_{\Omega_e} \frac{\partial \mathbf{N}^T}{\partial x} \mathbf{F}_{\mathbf{U}}^n \frac{\partial \hat{\mathbf{F}}^n}{\partial x} d\Omega_e + \int_{\Gamma_e} \mathbf{N}^T \bar{\mathbf{F}}_{\mathbf{U}}^n \frac{\partial \hat{\bar{\mathbf{F}}}^n}{\partial x} d\Gamma_e \tag{6.42}$$

Evaluation of Eq.(6.41) and Eq.(6.42) provides the coefficient matrix $[\mathbf{K}_e]$ for the inviscid case. If source terms are also included, the full matrix is found to be

$$[\mathbf{K}_e] = \left(\frac{1}{2} + \frac{\Delta t}{4} \breve{\mathbf{S}}_{\mathbf{U}}^n \right) \begin{bmatrix} -1 & -1 \\ 1 & 1 \end{bmatrix} - \frac{\Delta t}{2l_e} \breve{\mathbf{F}}_{\mathbf{U}}^n \begin{bmatrix} 1 & -1 \\ -1 & 1 \end{bmatrix} \tag{6.43}$$

where $\breve{\mathbf{F}}_{\mathbf{U}}$ and $\breve{\mathbf{S}}_{\mathbf{U}}$ are the average values over the elemental sub-domain (not to be confused with the post-processed flux value which is the average of adjacent elements). This is an alternative to numerical integration, which is equivalent when using linear shape functions. Similarly the coefficient matrix $[\mathbf{L}_e]$ is found to be

$$[\mathbf{L}_e] = \left(\frac{l_e}{6} + \frac{\Delta t l_e}{12} \breve{\mathbf{S}}_{\mathbf{U}}^n \right) \begin{bmatrix} 2 & 1 \\ 1 & 2 \end{bmatrix} + \frac{\Delta t}{4} \breve{\mathbf{F}}_{\mathbf{U}}^n \begin{bmatrix} -1 & -1 \\ 1 & 1 \end{bmatrix} \tag{6.44}$$

For the flux term, the contributions from the Taylor-Galerkin terms are not included since these arise from the numerical technique and will be zero on the boundaries. Thus,

$$\{\mathbf{f}_e\} = \left\{ \begin{array}{c} \tilde{\tilde{\mathbf{F}}}_i^n \\ -\tilde{\tilde{\mathbf{F}}}_j^n \end{array} \right\} \tag{6.45}$$

The system can then be implemented in computer code by substituting Eqs.(6.39), (6.43), (6.44) and (6.45) into Eq.(6.37) and implementing the boundary conditions (see section 6.4). Assuming that $u \ll c$, it can be shown that the stability condition for the characteristic system Eq.(6.19) is [24, 25]

$$\Delta t_{max} \approx \frac{\Delta x_{min}}{c_{max}} \tag{6.46}$$

although for a non-zero source term ($\mathbf{C}$) this will be slightly lower. Experience has shown that Eq.(6.46) with a small safety factor (i.e. using $\Delta t = 0.9\Delta t_{max}$) works well for the coupled system (Eq.(6.5)).

(a)
Schematic
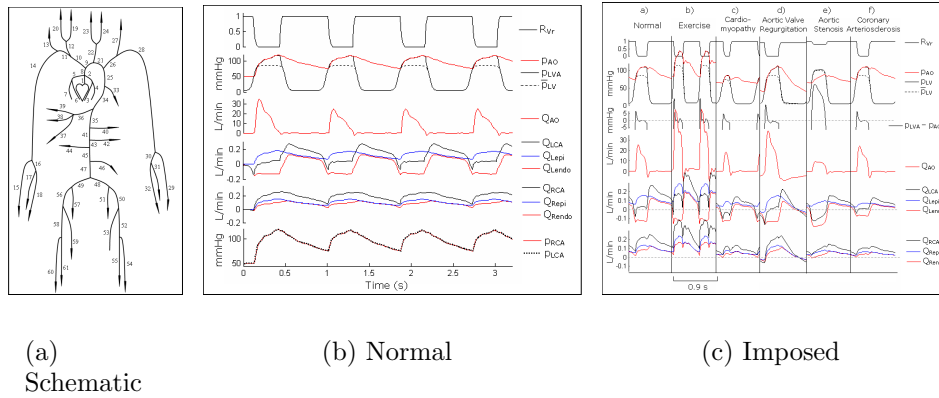
(b) Normal

(c) Imposed

Figure 6.1: 1D arterial flow network approximation. Approximation, Wave forms from normal and imposed conditions.

6.6   Some Results

The data used in essentially all 1D models comes originally from Noordergraaf et al [26] and Westerhof et al [27]. The model used here is shown in Figure 6.1(a) and for full details see reference [1].

Figure 6.1(b) shows various waveforms for a normal adult at rest. The model produces waveforms that contain all the well-known features that are obtained from *in vivo* measurements, with regularity arising after the first beat. The common haemodynamic measures of systolic/diastolic(mean) aortic pressures of 110/73(94), cardiac output (CO = mean Q_{AOroot}) of 4.5 L/min, contractility index (maximum dp_{LV}/dt) of 1179 mmHg/s, and systemic vascular resistance (SVR = mean p_{AO} / CO with central venous pressure taken to be zero) of 1671 dynes/s/cm^5 as obtained would all be considered normal for an adult human at rest. Figure 6.1(c) shows various imposed conditions.

Exercise is characterised by an increase in heart rate, force of ventricular contraction and peak pressure. Systemic vascular resistance also drops because more small blood vessels are recruited for oxygen transfer [28]. To simulate moderate exercise, the model parameters were adjusted as follows: HR = 115 bpm, $\bar{p}_{LV}$ = 115/5mmHg and RVOT = RVCT = 35ms. Cardiomyopathy may take several forms but is generally characterised by a reduction in the capacity of the heart to generate force. Accordingly, peak $\bar{p}_{LV}$ was reduced to 60 mmHg, while the isovolumic contraction and relaxation times were increased by 30% compared with the normal 'at rest' case. Compromise of the structural integrity of the aortic valve can lead to leakage of blood from aorta to ventricle

during diastole. To model mild valve regurgitation, the maximum valve reflection coefficient was set to $R_{Vr}(\max) = 0.9$. Aortic valve stenosis (or just 'Aortic Stenosis') is a narrowing of the aortic valve which impedes systolic flow. This leads to a significant pressure gradient between the left ventricle (LV) and the aorta, and to compensate, the LV must generate much greater pressures to maintain adequate arterial pressures and flows. This may be modelled with a reduced maximum valve transmission coefficient or non-zero reflection coefficient during systole as well as an increased $\bar{p}_{LV}$. Coronary arteriosclerosis is a stiffening of the coronary vessel walls due to the deposition of lipids, lipid by-products and calcium. To provide a basic model of arteriosclerosis, Young's modulus of the coronary vessels was increased by a factor of 4. Results from all these imposed conditions are shown in Figure 6.1(c).

6.7 Summary

This chapter provided a brief description of how to model fluid-structure interaction in an arterial network. Many of the numerical methods described in the Chapter 5 can be employed to solve the one-dimensional equations discussed here. Only one way of solving the governing equations are provided here. Many more results and discussions are available in the reference [1].

Bibliography

[1] J.P. Mynard and P. Nithiarasu. A 1d arterial blood flow model incorporating ventricular pressure, aortic valve and regional coronary flow using the locally conservative galerkin (lcg) method. *Communications in Numerical Methods in Engineering*, 24:367–417, 2008.

[2] V.L. Streeter, W.F. Keitzer, and D.F. Bohr. Pulsatile pressure and flow through distensible vessels. *Circulation Research*, 13(1):3–20, 1963.

[3] W. Ruan, M.E. Clark, M. Zhao, and A. Curcio. Global solution to a hyperbolic problem arising in the modeling of blood flow in circulatory systems. *Journal of Mathematical Analysis and Applications*, 331:1068–1092, 2007.

[4] J.K. Raines, M.Y. Jaffrin, and A.H. Shapiro. A computer simulation of arterial dynamics in the human leg. *Journal of Biomechanics*, 7(1):77–91, 1974.

[5] B.W. Schaaf and P.H. Abbrecht. Digital computer simulation of human systemic arterial pulse wave transmission: A nonlinear model. *Journal of Biomechanics*, 5(4):345–364, 1972.

[6] G. Porenta, D.F. Young, and T.R. Rogge. A finite-element model of blood flow in arteries including taper, branches, and obstructions. *Journal of Biomechanical Engineering*, 108(2):161–7, 1986.

[7] D.F. Young and F.Y. Tsai. Flow characteristics in models of arterial stenoses – ii. unsteady flow. *Journal of Biomechanics*, 6(5):547–559, 1973.

[8] J. R. Womersley. An elastic tube theory of pulse transmission and oscillatory flow in mammalian arteries. Technical Report TR 56-614, WADC Technical Report, 1957.

[9] A. Quarteroni, M. Tuveri, and A. Veneziani. Computational vascular fluid dynamics: problems, models and methods. *Computing and Visualization in Science*, 2(4):163–197, 2000.

[10] A.H. Shapiro. Steady flow in collapsible tubes. *Journal of Biomechanical Engineering*, 99:126–147, 1977.

[11] P.D. Stein and H.N. Sabbah. Turbulent blood flow in the ascending aorta of humans with normal and diseased aortic valves. *Circulation Research*, 39(1):58–65, 1976.

[12] L. Formaggia, J.F. Gerbeau, F. Nobile, and A. Quarteroni. On the coupling of 3D and 1D navier-stokes equations for flow problems in compliant vessels. *Computer Methods in Applied Mechanics and Engineering*, 191, 2001.

[13] L. Formaggia, D. Lamponi, and A. Quarteroni. One-dimensional models for blood flow in arteries. *Journal of Engineering Mathematics*, 47:251–276, 2003.

[14] L. Formaggia, F. Nobile, A. Quarteroni, and A. Veneziani. Multiscale modelling of the circulatory system: a preliminary analysis. *Computing and Visualization in Science*, 2(2):75–83, 1999.

[15] C. Hirsch. *Numerical Computation of Internal and External Flows: Computational Method for Inviscid and Viscous Flows*, volume 2. John Wiley and Sons, Chichester, UK, 1990.

[16] Kevin W. Thompson. Time dependent boundary conditions for hyperbolic systems. *Journal of Computational Physics*, 68(1):1–24, 1987.

[17] M. Anliker, R.L. Rockwell, and E. Ogden. Nonlinear analysis of flow pulses and shock waves in arteries, part i: Derivation and properties of mathematical model. *Zeitschrift für Angewandte Mathematik und Physik (ZAMP)*, 22(2):217–246, 1971.

[18] L. Formaggia, F. Nobile, and A. Quarteroni. A one dimensional model for blood flow: Application to vascular prosthesis. In I. Babuska, T. Miyoshi, and P.G. Ciarlet, editors, *Mathematical Modeling and Numerical Simulation in Continuum Mechanics, Lecture Notes in Computational Science and Engineering*. Springer-Verlag, Berlin, 2002.

[19] S.J. Sherwin, L. Formaggia, J. Peiró, and V. Franke. Computational modelling of 1D blood flow with variable mechanical properties and its application to the simulation of wave propagation in the human arterial system. *International Journal for Numerical Methods in Fluids*, 43(6-7):673–700, 2003.

[20] P. Nithiarasu. A simple locally conservative galerkin (LCG) finite-element method for transient conservation equations. *Numerical Heat Transfer Part B - Fundamentals*, 46(4):357–370, 2004.

[21] C.G. Thomas and P. Nithiarasu. An element-wise, locally conservative galerkin (LCG) method for solving diffusion and convection-diffusion problems. *International Journal for Numerical Methods in Engineering*, In Press, 2007.

[22] C.G. Thomas. *A locally conservative Galerkin (LCG) finite element method for convection-diffusion and Navier-Stokes equations*. PhD thesis, University of Wales Swansea, 2006.

[23] R.W. Lewis, P. Nithiarasu, and K.N. Seetharamu. *Fundamentals of the finite element method for heat and fluid flow.* John Wiley and Sons, 2004.

[24] S.J. Payne. Analysis of the effects of gravity and wall thickness in a model of blood flow through axisymmetric vessels. *Medical and Biological Engineering and Computing*, 42:799–806, 2004.

[25] B.S. Brook, S.A.E.G. Falle, and T.J. Pedley. Numerical solutions for unsteady gravity-driven flows in collapsible tubes: evolution and roll-wave instability of a steady state. *Journal of Fluid Mechanics*, 396:223–256, 1999.

[26] A. Noordergraaf, D. Verdouw, and H.B. Boom. The use of an analog computer in a circulation model. *Progress in Cardiovascular Disease*, 5:419–439, 1963.

[27] N. Westerhof, F. Bosman, C.J. De Vries, and A. Noordergraaf. Analog studies of the human systemic arterial tree. *Journal of Biomechanics*, 2(2):121–134, 1969.

[28] E.M. Khouri, D.E. Gregg, and C.R. Rayford. Effect of exercise on cardiac output, left coronary flow and myocardial metabolism in the unanesthetized dog. *Circulation Research*, 17(5):427–437, 1965.

Chapter 7

Three Dimensional Problems

7.1 Introduction

Over the last five years, there has been a significant increase in realistic multi-dimensional computational modelling of human body related problems. Realistic three dimensional blood flow calculations started around mid-nineties [1]-[7]. As seen the progress in this area has been rapid and the outcomes from such studies are increasingly used in the clinical settings. Majority of these studies are geometrically patient-specific and some of them even use *in vivo* measurements to apply appropriate velocity boundary conditions. The patient-specific study normally starts with a scan and any other measured data, if available. The image is then segmented to extract the required geometry. The commonly employed methods of segmentation include deformable models[8] and level-set methods[9]. These methods work by using background and artery image intensities as references. The geometry extracted is then used in generating a three dimensional mesh before a flow solver is used to get a solution.

The majority of such studies on physiological flows have been focused on the understanding of blood flow and related problems[1]-[6]. This is mainly due to the fact that cardiovascular problems account for the majority of disease related deaths in the developed world. However, the basic causes of cardiovascular problems are more widespread than blood flow behaviour. The problems associated with the human airways may include asthma[17], airway stenosis[18], obstructive sleep apnoea[19, 20], throat cancer[21], nasal airway blockage[22] and chronic obstructive pulmonary disease (COPD)[23]. Untreated, sleep apnoea can lead to pulmonary hypertension and to heart disease. It is, therefore, also essential to focus our attention to the human respiratory system. Patient specific studies on human airways are rather limited and these studies concentrate mainly on the lower human airways[24]. The upper human airways have received limited attention from the patient specific numerical modelling community, despite the fact that sleep apnea, throat cancer and nasal airway blockage are becoming more prevalent in developed countries.

7.2 Navier-Stokes Equations

The *in vivo* blood flow is generally assumed to be laminar Newtonian in a normal human body. It is anticipated that transition to turbulence is possible near a sever stenosis. It is also possible that the flow is turbulent close the the aortic valves. The blood is a non-Newtonian fluid but the

non-Newtonian flow effect can normally be neglected below a shear rate of $100s^{-1}$ (see Chapter 2). At normal conditions the flow is Newtonian in large arteries. However, it is possible that the non-Newtonian effect is important in a body with diseases. In this chapter, we assume that the blood flow is laminar and Newtonian.

Unlike blood flow, the air flow in a human airway may not be simply assumed to be laminar, although air is always a Newtonian fluid. Thus, for dealing with airway fluid dynamics we need turbulence models to account for the expected turbulence. The popular approaches currently used are Large Eddy Simulation (LES) and Reynolds Averaged Navier-Stokes (RANS). Some times unsteady RANS is also employed to obtain approximate transient solutions in human airways. In this chapter we use a one-equation RANS turbulence model to represent the turbulence.

The governing Navier-Stokes equations may be written in indicial form as
Mean continuity

$$\frac{1}{\beta^2}\frac{\partial p}{\partial t} + \frac{\partial \rho \bar{u}_i}{\partial x_i} = 0 \tag{7.1}$$

Mean momentum

$$\frac{\partial \bar{u}_i}{\partial t} + \frac{\partial}{\partial x_j}(\bar{u}_j \bar{u}_k) = -\frac{1}{\rho}\frac{\partial p}{\partial x_i} + \frac{\partial \tau_{ij}}{\partial x_j} + \frac{\partial \tau_{ij}^R}{\partial x_j} \tag{7.2}$$

where β is an artificial compressibility parameter, $\bar{u}_i$ are the mean velocity components, p is the mean pressure, ρ is the density, τ_{ij} is the mean laminar shear stress tensor given as

$$\tau_{ij} = \nu \left(\frac{\partial \bar{u}_i}{\partial x_j} + \frac{\partial \bar{u}_j}{\partial x_i} - \frac{2}{3}\frac{\partial \bar{u}_k}{\partial x_k}\delta_{ij} \right) \tag{7.3}$$

The Reynolds stress tensor, τ_{ij}^R, is introduced by Boussinesq's assumption, as

$$\tau_{ij}^R = -\overline{u_i' u_j'} = \nu_T \left(\frac{\partial \bar{u}_i}{\partial x_j} + \frac{\partial \bar{u}_j}{\partial x_i} - \frac{2}{3}\frac{\partial \bar{u}_k}{\partial x_k}\delta_{ij} \right) \tag{7.4}$$

In these equations, ν is the kinematic viscosity of the fluid, ν_T is the turbulent eddy viscosity and δ_{ij} is the Kroneker delta.

The Spalart–Allmaras (SA) [25] model was first introduced for aerospace applications and now is is commonly used in incompressible flow calculations. The SA model is a one equation model, which employs a single scalar equation and several constants, to model turbulence. We find this model both to be fast and accurate for incompressible flows compared to other RANS models [26, 27]. The scalar equation is

$$\frac{\partial \hat{\nu}}{\partial t} + \frac{\partial u_j \hat{\nu}}{\partial x_j} = c_{b1}\hat{S}\hat{\nu} + \frac{1}{\sigma}\left[\frac{\partial}{\partial x_i}(\nu + \hat{\nu})\frac{\partial \hat{\nu}}{\partial x_i} + c_{b2}\left(\frac{\partial \hat{\nu}}{\partial x_i}\right)^2 \right] - c_{w1}f_w \left[\frac{\hat{\nu}}{y}\right]^2 \tag{7.5}$$

where

$$\hat{S} = S + (\hat{\nu}/k^2 y^2)f_{v2} \tag{7.6}$$

$$f_{v2} = 1 - X/(1 + Xf_{v1}) \tag{7.7}$$

In Equation (7.6), S is the magnitude of vorticity. The eddy viscosity is calculated as

$$\nu_T = \hat{\nu} f_{v1} \tag{7.8}$$

where

$$f_{v1} = X^3/(X^3 + c_{v1}^3) \tag{7.9}$$

$$X = \hat{\nu}/\nu \tag{7.10}$$

The parameter f_w is given as

$$f_w = g \left[\frac{1 + c_{w3}^6}{g^6 + c_{w3}^3} \right]^{1/6} \tag{7.11}$$

$$g = r + c_{w2}(r^6 - r) \tag{7.12}$$

$$r = \frac{\hat{\nu}}{\hat{S} k^2 y^2} \tag{7.13}$$

The constants are $c_{b1} = 0.1355, \sigma = 2/3, c_{b2} = 0.622, k = 0.41, c_{w1} = c_{b1}/k^2 + (1 + c_{b2})/\sigma, c_{w2} = 0.3, c_{w3} = 2$ and $c_{v1} = 7.1$.

Note that the turbulence equations and eddy viscosity are absent for laminar blood flow problems.

7.3 Numerical Scheme

The CFD algorithm used here has been tested in the past for various laminar and turbulent flows. The method is based upon the Characteristic Based Split (CBS) algorithm[28]–[34]. The algorithm is based upon the fractional step method to stabilise pressure and a characteristic based approach to stabilize discrete convection operators. This combination, along with a local time stepping, was found to be robust[35, 36]. The method has been employed, both in its fully explicit and semi-implicit forms, in the past. We have used the artificial compressibility based method here [28, 31]. The method solves the incompressible Navier-Stokes equations in three steps. In the first step, an intermediate momentum field is solved. In the second step, pressure is computed and in the third step, the momentum field is corrected. The one equation Spalart–Allmaras [25, 37] turbulence model is added as a fourth step. The first three steps of the CBS scheme used in its semi–discrete form may be summarised as
Step1: Intermediate momentum

$$\Delta \tilde{U}_i = \tilde{U}_i - U_i^n = \Delta t \left[-\frac{\partial}{\partial x_j}(u_j U_i) + \frac{\partial \tau_{ij}}{\partial x_j} + \frac{\partial \tau_{ij}}{\partial x_j}^R + \frac{\Delta t}{2} u_k \frac{\partial}{\partial x_k} \left(\frac{\partial}{\partial x_j}(u_j U_i) \right) \right]^n \tag{7.14}$$

where $U_i^n = U_i(t_n); \Delta t = t^{n+1} - t^n$ and ˜indicates an intermediate quantity. The higher order terms are due to time discretization using the Characteristic Galerkin approach [38, 39, 33].
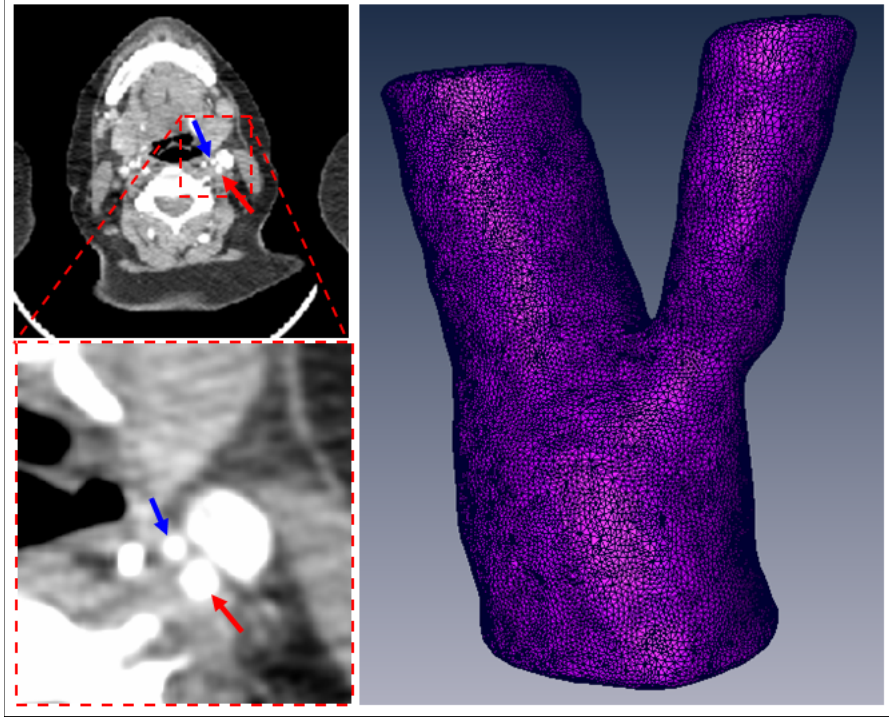
Figure 7.1: (Left) Two views of a single CT image slice with internal and external carotid arteries indicated by red and blue arrows respectively. From multiple 2D slices, a 3D patient-specific mesh of the normal carotid bifurcation was constructed (right).

Step2: Pressure

$$\left(\frac{1}{\beta^2}\right)^n \Delta p = \left(\frac{1}{\beta^2}\right)^n (p^{n+1} - p^n) =$$

$$-\Delta t \left[\frac{\partial U_i^n}{\partial x_i} + \theta_1 \frac{\partial \Delta \tilde{U}_i}{\partial x_i} - \Delta t \theta_1 \left(\frac{\partial^2 p^n}{\partial x_i \partial x_i} + \theta_2 \frac{\partial^2 \Delta p}{\partial x_i \partial x_i} \right) \right] \tag{7.15}$$

Step3: Momentum correction

$$\Delta U_i = U_i^{n+1} - U_i^n = \Delta \tilde{U}_i - \Delta t \frac{\partial p}{\partial x_i}^{n+\theta_2} \tag{7.16}$$

where $0.5 \leq \theta_1 \leq 1$ and $0 \leq \theta_2 \leq 1$. For the explicit scheme, employed in the present study, $\theta_2 = 0$. The equations are derived from the observation that the time discretization is carried out along the characteristic. A simple approximate backward integration gives the equations with some extra convection stabilization terms (last term in right hand side at step1). These extra terms are consistent and reduce oscillations, due to the standard Galerkin discretization of convective terms. These higher order terms are very important when the time discretization is explicit. The artificial compressibility parameter β is defined locally, based on the local velocity scales. Further details on the selection of β may be found in [28].
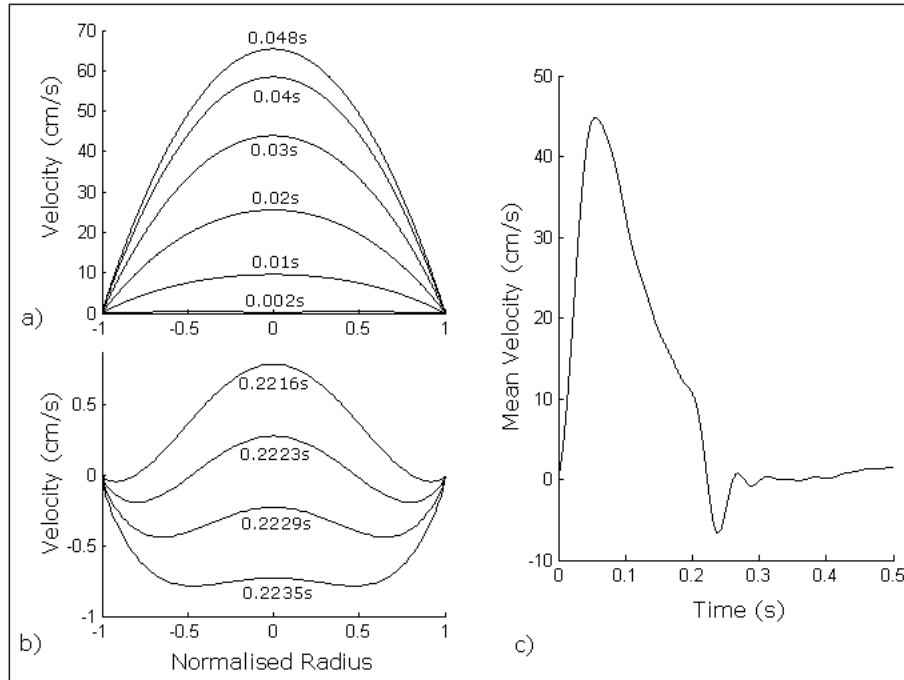
Figure 7.2: The inlet velocity profile at various times a) during the initial upstroke and b) around the time of flow reversal. c) The mean velocity over the whole cardiac cycle.

The scalar transport turbulence equations are also subjected to the characteristic time discretization, similar to Step 1. Once the semi–discrete form is available, the standard Galerkin spatial discretization follows [38, 33]. For laminar blood flow problems, the fourth step is not used.

7.4   Cardiovascular Problems

7.4.1   Flow Through a Carotid Bifurcation

The geometry of the 3D model was constructed (Figure 7.1) from a set of anonymous computed tomography (CT) images obtained from Singleton Hospital, Swansea, UK, which consisted of 390 axial slices, from the thorax to the nasal passage. Data preparation, segmentation and mesh generation were performed with the data visualisation software AMIRA (Mercury Computer Systems, Chelmsford, MA, USA). A detailed description of these procedures may be found in [40, 41]. Generation of boundary conditions and all post-processing was performed in Matlab. The simulations were performed using an in-house computational fluid dynamics solver [42].

Boundary Conditions

In 1D, the mean pressure, velocity or cross-sectional area at the inlet can be prescribed in a straightforward manner via the entering characteristic. In the 3D, however, the no-slip condition $(u|_R = 0)$ must be satisfied on the walls. A velocity profile for the inlet boundary condition may be obtained from *Hagen-Poiseuille flow*, but this is only appropriate for fully-developed, steady flows. A better alternative is a fully-developed unsteady solution known as *Womersley flow* [43, 44, 45].
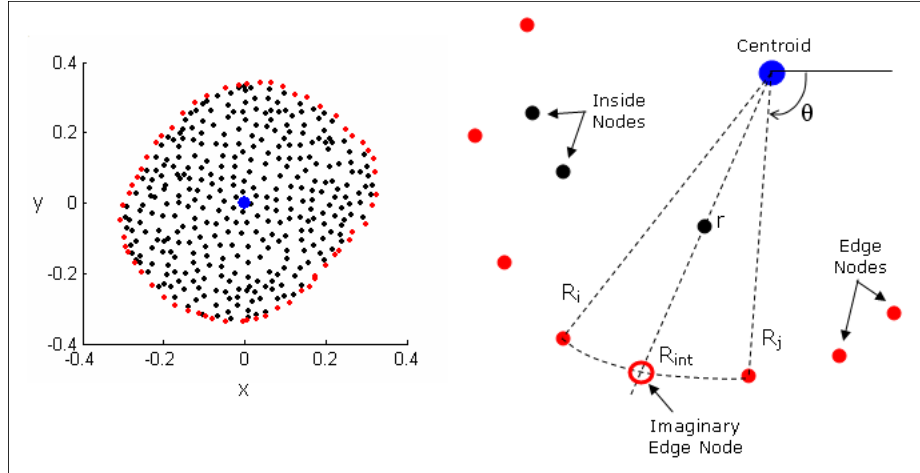
Figure 7.3: Schematic demonstrating how to map a radial velocity profile on to the 2D boundary surface nodes.
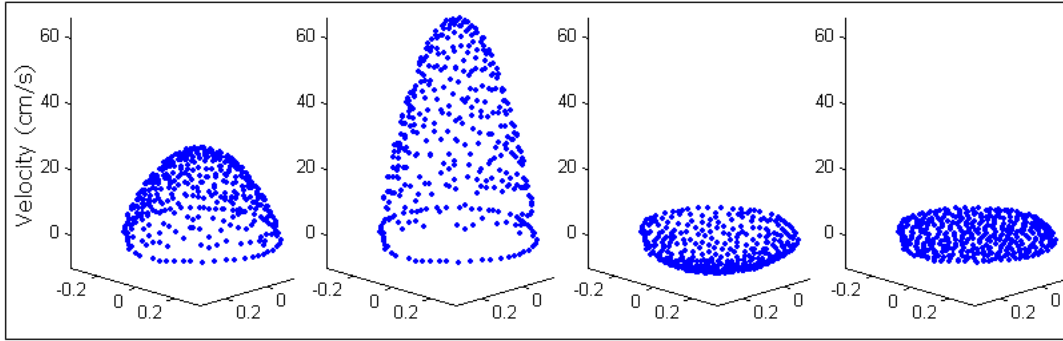
Figure 7.4: 2D inlet velocity profile at various times in the cardiac cycle. The vertical axis is velocity.

This is a 2D linear viscous solution of the Navier-Stokes equations in cylindrical tubes, and has been used in previous 3D modelling studies (for example, in [40, 46]). Consider a sinusoidal mean pressure gradient at a given cross-section given by

$$\frac{\partial p}{\partial x} = B \cos(\omega t + \phi) \tag{7.17}$$

where B is the amplitude, $\omega = 2\pi f$ is the angular frequency (radians/s) and ϕ is the phase angle (radians). x refers to the axial direction and in cylindrical coordinates, $\frac{\partial p}{\partial r} = \frac{\partial p}{\partial \theta} = 0$, where r is the radial component and θ is the tangential component. The velocity profile in that cross-section is given by

$$u(r) = \Re\left(\frac{B}{j\omega} \left[1 - \frac{J_0\left(j^{3/2} \sqrt{\frac{\omega}{\nu}} r \right)}{J_0\left(j^{3/2} \sqrt{\frac{\omega}{\nu}} R \right)} \right] e^{(j\omega t + \phi)} \right) \tag{7.18}$$

where R is the vessel radius, $j = \sqrt{-1}$ is the imaginary number, $\nu = \frac{\mu}{\rho}$ is the kinematic viscosity, J_0 is the Bessel function of the first kind and order 0, and $\Re()$ denotes the real part (note:
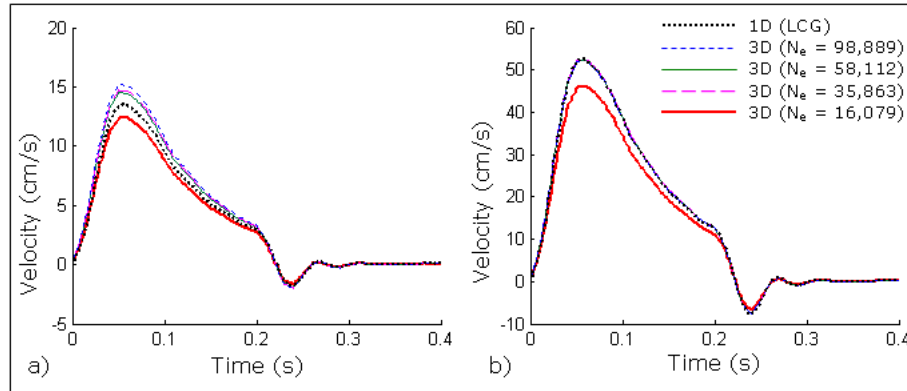
Figure 7.5: a) Internal and b) external carotid artery outlet mean velocities, showing the convergence of the 3D model as mesh density is increased and a comparison with the 1D model.

the imaginary part is not used). The Womersley solution assumes that the velocity in the radial and tangential directions are zero ($v = w = 0$).

Eq.(7.18) can only be applied to signals of the type in Eq.(7.17). However using the assumption of linearity, the velocity profile for an arbitrary pressure gradient may be obtained by adding the profiles of a number of sinusoidal harmonics. While in theory, exact representation of an arbitrary signal may require an infinite number of harmonics, physiological signals can be represented with sufficient accuracy using only a few harmonics. Table 7.1 provides the 15 harmonics used in this model which were obtained by performing a Fourier Series analysis on a measured aortic velocity waveform [47]. For each of these harmonics, the radial velocity profile was calculated from Eq.(7.18). All velocity profiles were then added together to yield the resultant velocity profile. The final result was also scaled to provide the desired peak velocity. Figure 7.2a,b shows the velocity profile at various times during the initial upstroke and around the time of flow reversal, while Figure 7.2c shows the mean velocity for the whole cardiac cycle. For large mean velocities, the velocity profiles are essentially parabolic. However more complex profiles are seen at near-zero velocities, where it is possible to have positive velocities near the centre of the vessel but negative velocities near the walls [40].

The velocity profile must then be mapped to the 2D inlet surface. If the inlet were perfectly circular, each node could be assigned a velocity for each time step based on its normalised radius. However, the input surface is generally not circular and so prescribing nodal velocities is somewhat more complex. The mapping, illustrated in Figure 7.3, may thus be performed as follows.
1. Identify the inlet *edge nodes* based on the surface IDs of the surrounding elements.
2. Determine the centroid of the inlet, calculated as the average of x and y values, and perform a mapping on all nodes so that the centroid is at (0,0).
3. Express the positions of all inlet surface nodes in 2D polar coordinates (r, θ), with the third co-ordinate assumed constant over the whole inlet surface.
4. Calculate a normalised radius for each inside node. This is found by first identifying the two edges nodes with the closest value of θ. From the absolute radii of these two edge nodes (R_i and R_j), a linearly interpolated radius (R_{int}) of an imaginary edge node is found. This imaginary edge

(a) Full aorta   (b) Geometry used for   (c)   Finite   element
                      calculations   mesh
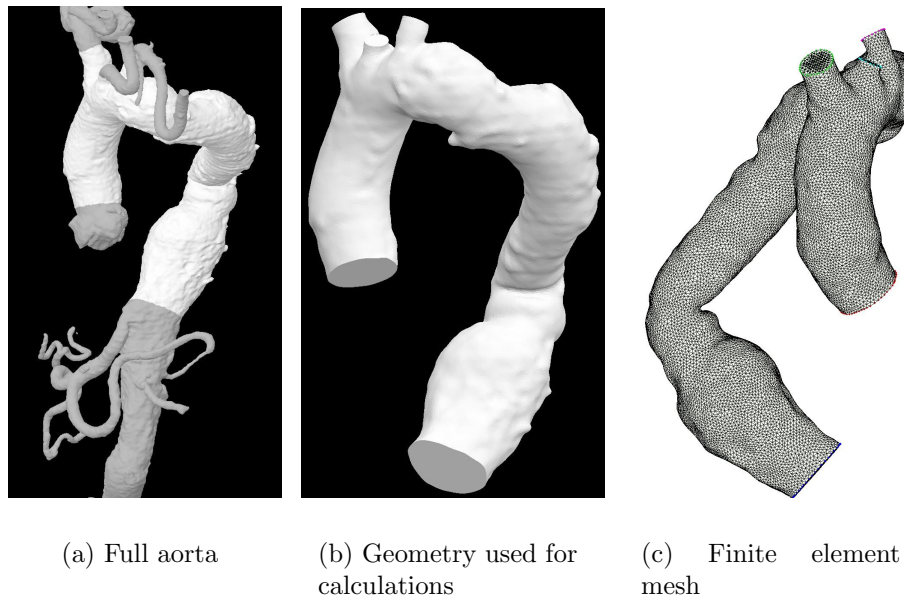
Figure 7.6: A aorta with an aneurysm. Geometry and mesh.

node is on the same line that connects the inside node with the centroid.

5. Based on the radius of the imaginary edge node, the normalised radius (r_n) of the inside node can be calculated as $r_n = \frac{r}{R_{int}}$, and the appropriate velocity prescribed. This mapping results in a smooth 3D inlet velocity profile, as shown in Figure 7.4 at four different times during the cardiac cycle.

Figure 7.5 shows the mean velocity profiles at the two exists. This figure also shows the results from the one dimensional study for the identical inlet conditions. As shown, the agreement is excellent between the one dimensional and the larger 3D exit velocity profiles. This is due to the fact that the diameter of this branch is fairly uniform along the length and nearly circular. The agreement between the one dimensional solution and the smaller exit is not very good. This shows the need for 3D patient-specific studies when the vessels are nonuniform and not nearly circular.

7.4.2   Flow Through a Human Aorta

The second example considered is a human aorta with an Abdominal Aortic Aneurysm(AAA) as shown in Figure 7.6. Figure 7.6(a) shows the segmented full aorta and in Figure7.6(b) the computational domain is presented. Figure 7.6(c) shows one of the finite element meshes used in the calculations. Many meshes with few hundred elements to two million elements were generated. The inlet velocities are prescribed similar to the previous problem. The mean flow rate here is assumed to be 5l/m. At exits the flow is divided according to normal physiological conditions. Prescription of flow rates at exits is essential if appropriate resistances are not available. The blood vessel is assumed to be static although in reality, aorta is compliant.

Figure 7.7 shows the wall shear stress (WSS) distributions at various times of a blood flow cycle. In cardiovascular problems WSS is the most important quantity. The WSS value should

Table 7.1: Harmonics used to construct the inlet velocity profile

Harmonic	Frequency (Hz)	Amplitude (dynes cm^{-2} s^{-1})	Phase (rad)
0	0	126.88125	0
1	1.63548	219.048	-1.59841
2	3.27097	156.0645	3.04933
3	4.90645	80.2545	1.81371
4	6.54193	57.64425	1.22483
5	8.17742	56.193375	-0.107859
6	9.8129	25.0012125	-1.55024
7	11.4484	17.1054	-1.40587
8	13.0839	24.2474625	-2.93862
9	14.7194	8.1630375	1.45781
10	16.3548	10.90725	2.74547
11	17.9903	12.6963375	0.490823
12	19.6258	2.7560325	-2.48452
13	21.2613	5.98305	-0.254379
14	22.8968	5.02695	-2.84223
15	24.5323	2.558115	0.376408

be optimal to live without any arterial diseases. It is interesting to notice a small folding near the neck of the aneurysm in this geometry. This folding is a very important location for the doctors to treat as this has the largest WSS, especially just after the peak systole($t = 0.27$s).

7.5   Human Airways

7.5.1   A model human airway problem

A model human upper airway is considered first to verify the steady state calculations. The geometry used is an idealised oropharynx from Reference [48]. This reference provides some experimental data for the idealised geometry. Although identical reproduction of the experimental configuration is difficult, we have reproduced an approximate configuration from the geometrical data given in Heenan et al. [48]. We have generated an unstructured mesh with about one million tetrahedral elements to discretize the domain as shown in Figure 7.8.

Figures 7.9 and 7.10 show some sample qualitative results at a flow rate of 37.35 l/m. The u_3 velocity distribution clearly shows the acceleration as the flow enters the pharynx and also when it leaves the pharynx through the epiglottis. As a result of the complex nature of the geometry, some slow moving, re–circulatory regions are also noticed, near the entrance to pharynx. It is also observed that the majority of the pressure drop occurs as the fluid enters the pharynx and also as it passes the epiglottis. The oral cavity shows almost no pressure change. The qualitative results obtained compare well with the experimental results given by Heenan et al. [48].

To further increase the confidence in the flow solver, the pressure drop calculations were carried out for different flow rates. The pressure drop is calculated as the difference between the average

(a) $t = 0.09$s   (b) $t = 0.27$s   (c) $t = 0.45$s   (d) $t = 0.63$s   (e) $t = 0.81$s
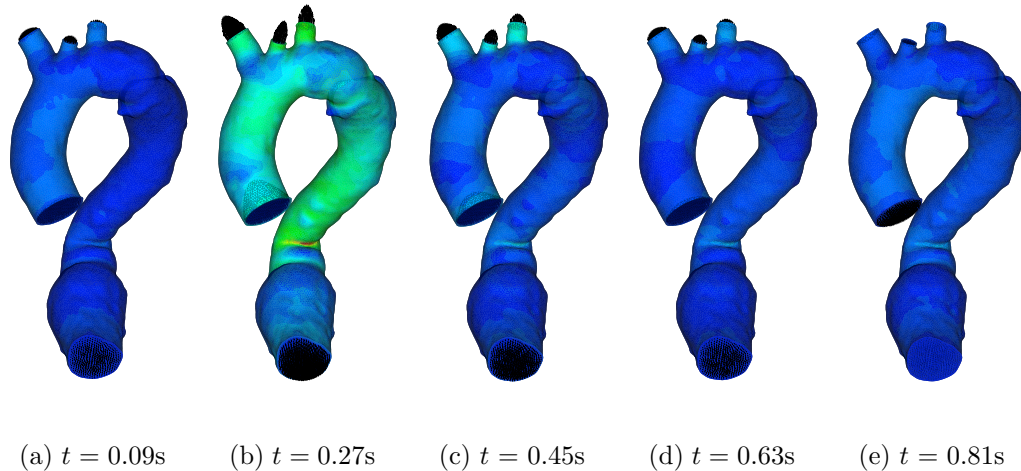
Figure 7.7: A aorta with an aneurysm. Wall shear stress distribution.

pressure values at the inlet and exit. Figure 7.11 shows the comparison of pressure drop values obtained from the present numerical study and the experimental data. As seen the agreement between the two results is good. The small difference between the results may be attributed to the minor differences in the geometry. The geometry used here was constructed from the thirteen cross sections provided by Heenan et al. [48]. The sections were linearly connected to obtain the full geometry.

7.5.2   Inhalation studies

Inhalation studies are important for determining the flow behaviour during drug deliveries. The area at the inlet of the patient specific geometry is approximately 222 mm^2. The properties of air are assumed to be constant. A kinematic viscosity of 1.69×10^{-5} m^2/s and density of 1.2 kg/m^3 were used in the calculations. The flow rate in the human airways normally varies between 15 and 45 l/m depending on the state of the subject. The inhalation flow is studied by prescribing a velocity based on the assumed flow rate. In order to accurately represent the velocity boundary conditions, it may be essential to consider the flow through the nasal passages. As mentioned previously, it was not easy to construct the geometry of the nasal passages using low resolution scans. We will consider the influence of nasal air passages in a future article.

The mesh used consists of about half a million elements. The mesh sensitivity study shows that, at a Reynolds number (based on 100mm) of 1000, a difference in the pressure drop of about 5% between meshes with half and one million linear tetrahedral elements. Certainly, a higher quality solution can be obtained on the mesh with one million elements. However, to save time, we adopted the mesh with half a million elements. This mesh is sufficient to demonstrate the main features of human upper airway fluid dynamics. At the inlet of the geometry, a constant velocity value is assumed depending on the flow rate.

The qualitative results, at an inhalation flow rate of 33.76 l/m, are presented in Figures 7.12–7.14. The vector plots in Figure 7.12 clearly show a recirculation region just below the vocal

Figure 7.8: An idealised human upper airway model. Unstructured mesh.

cords. Although the geometry looks fairly straight, the recirculation makes the physics more interesting. As expected, the flow accelerates near the tongue base (oropharynx) as it passes into the laryngopharynx (see Figure 7.11). The flow stabilises and reaches a nearly developed state as it moves towards the bifurcation, within the trachea.

Figure 7.13 shows the pressure distribution. Once again all the action takes place near the laryngopharynx. The flow recirculation below the epiglottis also creates a negative wall pressure distribution at the posterior surface of the airway. However, the pressure at the anterior remains positive. The negative pressure created by the recirculation and the naturally narrow portion of oropharynx are responsible for the large pressure drop. As in the model airway discussed in the previous section, here also the pressure changes are almost nil in the oral cavity.

The wall shear stress distribution in Figure 7.14 also shows a trend in accordance with the flow distribution. The maximum wall shear stress occurs near the narrow portion of the airway. It is also noticed that the wall shear stress is low near the recirculation on the posterior surface of the airway. However, the accelerating downward velocity along the anterior wall opposite the recirculation increases the velocity gradient and increases the wall shear stress.

Table 7.2 presents comparisons of the pressure drop for the model airway presented in the previous section and the patient specific airway studied in this subsection for three different flow

(a) u_3 velocity com-   (b) Pressure
ponent
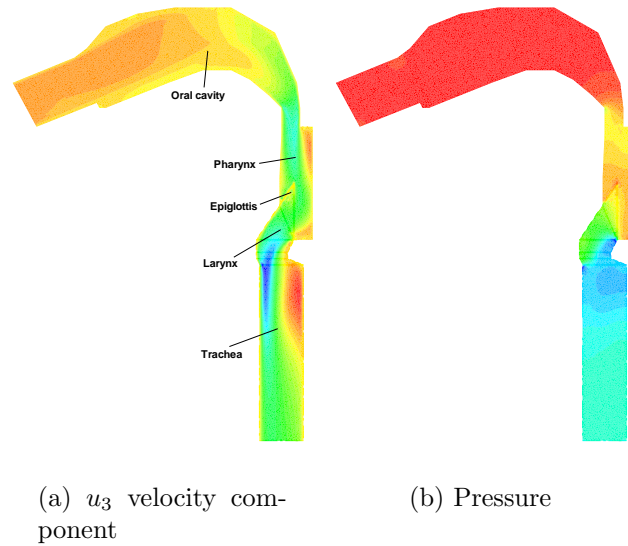
Figure 7.9: Flow through an idealised human upper airway, flow rate $= 37.35$l/min

Table 7.2: Pressure drop (Pa) comparison of numerical calculations of model and patient specific human upper airways

Flow rate	Model airway (present)	Cast model ([49])	Patient specific airway (present)
16.88	12.89	-	10.58
33.76	47.73	44.00	41.95
50.64	108.45	-	99.746

rates. Although a very close match between the two is not anticipated, the difference between the pressure drops is not extremely high. The difference is about 8% at 50.64 l/m, about 12.1% at 33.76 l/m and 17.9% at 16.88 l/m. There are two major differences between the model and patient specific upper human airways. The first is that, although similarity exists between the two, they are not geometrically identical. The second difference is that the model airway has about a 16% longer flow path than the patient specific airway. This second difference is clearly reflected in the higher pressure drop obtained on the model human upper airway.

Figures 7.15 and 7.16 show the wall pressure and shear stress distributions along the anterior and posterior walls of the airway up to the bifurcation. From the pressure distribution, it is clear that the major pressure drop occurs between -620 and -632mm with the minimum pressure reported near -631mm. This is the location just above the vocal folds in the laryngopharynx. The negative pressure difference obtained at 16.88l/m is almost nil and, as the flow rate increases, the pressure drop noticed in the laryngopharynx also increases. The negative pressure created near the vocal folds triggers a flow recirculation near the posterior surface, as the flow leaves the laryngopharynx, into the larynx and trachea. The recirculation near the posterior wall results in flow acceleration near the anterior wall, with an increase in velocity gradients along the anterior

Figure 7.10: Flow through an idealised human upper airway. Velocity vectors

wall. This is clearly represented by the higher wall shear stress distribution on the anterior wall between -650 and -700mm. In addition, the shear stress peaks at both the anterior and posterior walls coincide with the negative peak pressure value. The combination of the negative pressure difference and the peak shear stress value makes the laryngopharynx location an important area for airway collapse investigation. It is noticed that both the pressure difference and wall shear stress distributions are not very smooth. This is mainly due to the rapid changes in the surface contours. A higher mesh resolution may marginally increase the smoothness of the wall shear stress distribution. Even on structured meshes, the shear stress distribution is expected to have rapid changes all along the surface [50].

7.6 Summary

The three-dimensional modelling procedures are still not well established due to patient-specific nature of the geometries and difficulties associated with fluid-dynamics itself. Many groups and industry are very seriously involved in developing a suitable software for modelling from patient-scans.

Bibliography

[1] C.A. Taylor, T.J.R. Hughes, and C.K. Zarins. Finite element modeling of blood flow in arteries. *Computer Methods in Applied Mechanics and Engineering*, 158:155–196, 1998.

[2] J.S. Milner, J.A. Moore, B.K. Rutt, and D.A. Steinman. Hemodynamics of human carotid
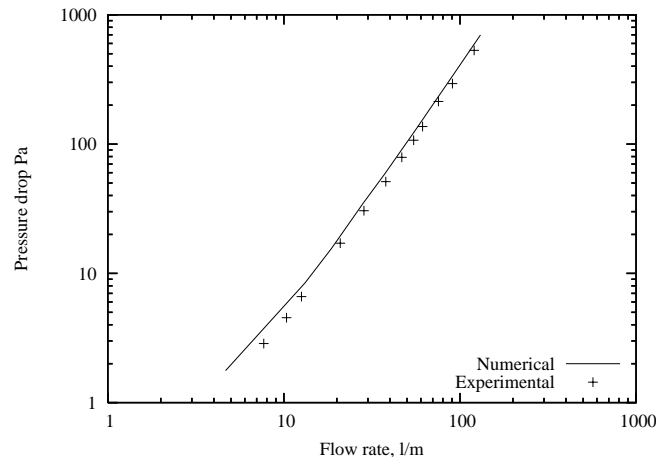
Figure 7.11: Flow through an idealised human upper airway. Pressure drop. Experimental data from Heenan et al. [48]

artery bifurcations: Computational studies with models reconstructed from magnetc resonance imaging of normal subjects. *Journal of Vascular Surgery*, 28:143–155, 1998.

[3] D.A. Steinman, J.S. Milner, C.J. Norley, S.P. Lownie, and D.W. Holdsworth. Image-based computational simulation of flow dynamics in a giant intracranial aneurysm. *AJNR Journal of American Society of Neuroradiology*, 24:559–566, 2003.

[4] R. Löhner R, J. Cebral, O. Soto, P. Yim, and J.E. Burgess. Applications of patient-specific cfd in medicine and life sciences. *International Journal for Numerical Methods in Fluids*, 43:637–650, 2003.

[5] R. Torii, M. Oshima, T. Kobayashi, K. Takagi, and T.E. Tezduyar. Computer modelling of cardiovascular fluid-structure interactions with the deforming-spatial-domain/stabilized space-time formulation. *Computer Methods in Applied Mechanics and Engineering*, 195:1885–1895, 2006.

[6] A. Valencia, S. Botto, J. Sordo, M. Galvez, and L. Badilla. Comparison of haemodynamics in verebral aneurysms of different sizes located in the ophtalmic artery. *International Journal for Numerical Methods in Fluids*, 53:793–809, 2007.

[7] R. Van Loon. Computational heart valve models to investigate aortic stenosis. *Comm. Num. Meth. Eng.*, Submitted, 2008.

[8] M. Kass, A. Witkin, and D. Terzopoulos. Snakes: Active contour models. *International Journal of Computer Vision*, pages 321–331, 1988.

[9] J. Sethian. *Level Set Methods and Fast Marching Methods*. Cambridge University Press, Cambridge, 1999.

[10] F. Calamante, P.J. Yim, and J.R. Cebral. Estimation of bolus dispersion effects in perfusion mri using image-based computational fluid dynamics. *NuroImage*, 19:341–353, 2003.

(a) Vectors

(b)   Recirculation below   the   vocal cords
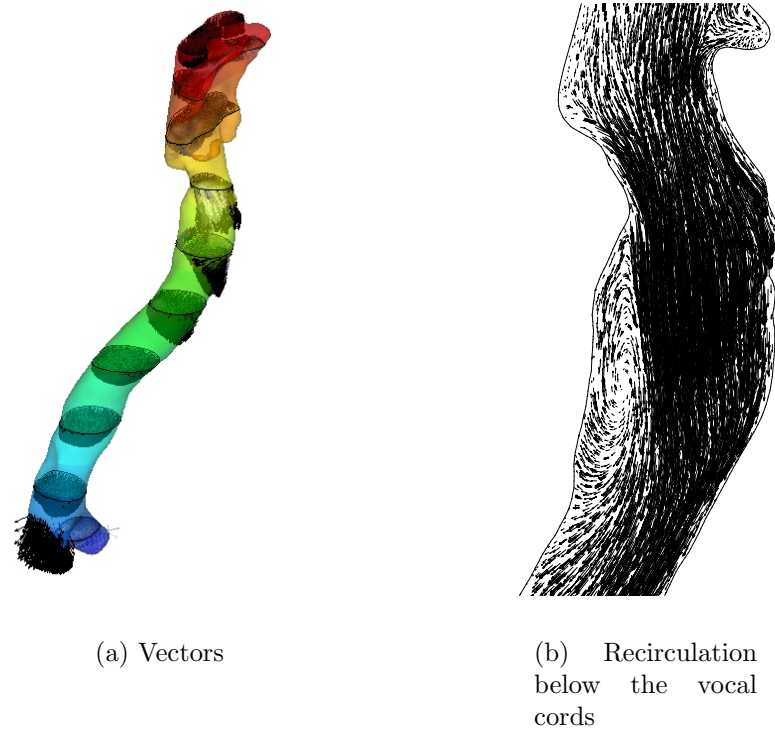
Figure 7.12: Velocity vector plots at an inhaling flow rate of 33.76l/m

[11] M.A. Castro, C.M. Putman, and J.R. Cebral. Patient-specific computational modeling of cerebral aneurysms with multiple avenues of flow from 3d rotational angiography images. *Academic Radiology*, 13:811–821, 2006.

[12] J.R. Cebral, P.J. Yim, R. Löhner, O. Sato, and P.L. Choyke. Blood flow modeling in carotis arteries with computational fluid dynamics and mr imaging. *Academic Radiology*, 9:1286–1299, 2002.

[13] M.R. Kaazempur-Mofrad, M. Bathe, H. Karcher, H.F. Younis, H.C. Seong, E.B. Shim, R.C. Chan, D.P. Hinton, A.G. Isasi, A. Upadhyaya, M.J. Powers, L.G. Griffiths, and R.D. Kamm. Role of simulation in understanding biological systems. *Computers and Structures*, 81:715–726, 2003.

[14] R. Moreno, F. Nicoud, and H. Rousseau. Non-linear-transformation field to build moving meshes for patient specific blood flow simulations. *European Conference on Computational Fluid Dynamics, ECCOMAS CFD 2006, P. Wesseling, E. Onate, J. Periaus (eds), TU Delft, The Netherlands*, 2006.

[15] G. Tabor, D. Tame, F. Pierron, P.G. Young, A. Watkinson, and J. Thompson. Patient specific arterial flow simulation with additional geometric elements. *European Conference on Computational Fluid Dynamics, ECCOMAS CFD 2006, P. Wesseling, E. Onate, J. Periaus (eds), TU Delft, The Netherlands*, 2006.

(a)   (b) Side   (c) Pos-   (d) Side
Ante-   terior
rior
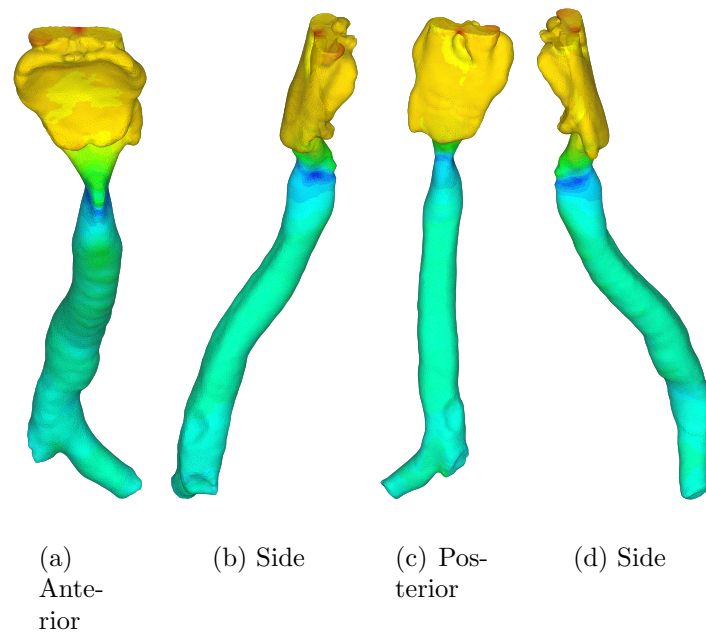
Figure 7.13: Pressure distribution at a flow rate of 33.76l/min. Maximum pressure = 63.233 Pa, Minimum pressure = -23.90 Pa, Total pressure drop = 41.95 Pa

[16] B.J.B.M. Wolters, M.C.M. Rutten, G.W.H. Schurink, U. Kose, J. de Hart, and F.N. van de Vosse. A patient-specific computational model of fluid-structure interation in abdominal aortic aneurysms. *Medical Engineering & Physics*, 27:871–883, 2005.

[17] P. Ebden, A. Jenkins, G. Houston, and B.H. Davies. Comparison of 2 high-dose corticosteroid aerosol treatments, beclomethasone dipropionate (150 ug day) and budesonide (1600 ug day), for chronic astma. *THORAX*, 41:869–874, 1986.

[18] D.B. Hawkins and W.M. Luxford. Laryngel stenosis from endotracheal intubation - a review of 58 cases. *Annals of Otology Rhinology and Laryngology*, 89:454–458, 1980.

[19] J. Wright, R. Johns, I. Watt, A. Melville, and T. Sheldon. Health effects of obstructive sleep apnoea and the effectiveness of continuous positive airways pressure: A systematic review of the research evidence. *British Medical Journal*, 314:851–860, 1997.

[20] I. Ayappa and D.M. Rapoport. The upper airway in sleep: Physiology of the pharynx. *Physiological Review*, 7:9–33, 2003.

[21] M.F. De Boer, L.K. McCormick, J.F.A. Pruyn, R.M. Ryckman, and B.W. van den Borne. Physical and psychosocial correlates of head and neck cancer: A review of the literature. *Ptolaryngology-Head and Neck Surgery*, 120:427–436, 1999.

[22] M.B. Constantian and R.B. Clardy. The relative importance of septal and nasal valvular surgery in correcting airway obstruction in primary and secondary rhinoplasty. *Plastic and Reconstructive Surgery*, 98:38–54, 1996.

(a) An-   (b) Side   (c)   (d) Side
terior   Pos-
                          terior
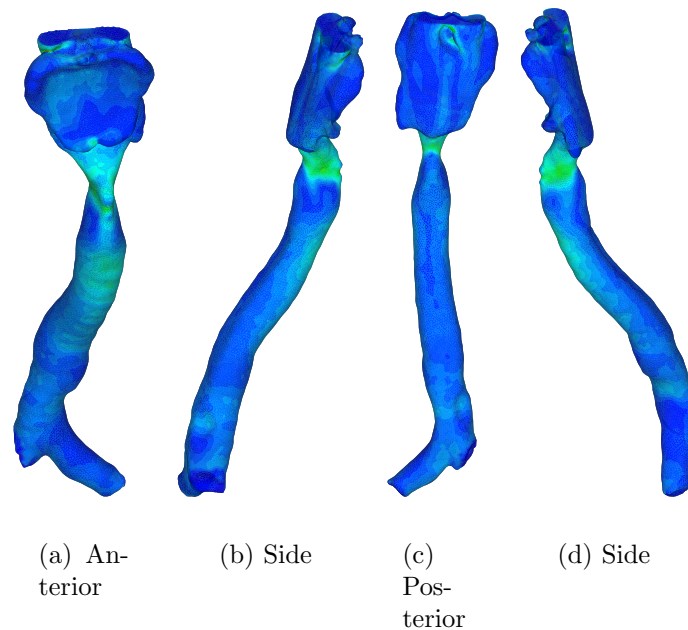
Figure 7.14: Wall shear stress distribution at a flow rate of 33.76l/min. Maximum shear stress = 0.513 Pa

[23] V. Kulish. *Human Respiration. Anotamy and physiology, mathematical modeling, numerical simulation and applications.* WIT Press, Southampton, 2006.

[24] J.R. Cebral and R.M. Summers. Tracheal and central bronchial aerodynamics using virtual bronchoscopy and computational fluid dynamics. *IEEE Transactions on Medical Imaging*, 23:1021–1033, 2004.

[25] P.R. Spalart and S.R. Allmaras. A one-equation turbulence model for aerodynamic flows. *AIAA paper 92-0439*, 1992.

[26] P. Nithiarasu and C-B. Liu. An explicit characteristic based split (cbs) scheme for incompressible turbulent flows. *Computer Methods in Applied Mechanics and Engineering*, 195:2961–2982, 2006.

[27] P. Nithiarasu, C-B. liu, and N. Massarotti. Laminar and turbulent flow through a model human upper airway. *Communications in Numerical Methods in Engineering*, 23:1057–1069, 2007.

[28] P. Nithiarasu. An efficient artificial compressibility (ac) scheme based on the characteristic based split (cbs) method for incompressible flows. *International Journal for Numerical Methods in Engineering*, 56:1815–1845, 2003.

[29] P. Nithiarasu, N.P. Weatherill, K. Morgan, O. Hassan, P. Ebden, and H. Whittet. Computational modelling of sleep apnoea. *Conversazione*, Swansea:Poster, 11 Dec 2003.

(a) Pressure   (b) Shear stress
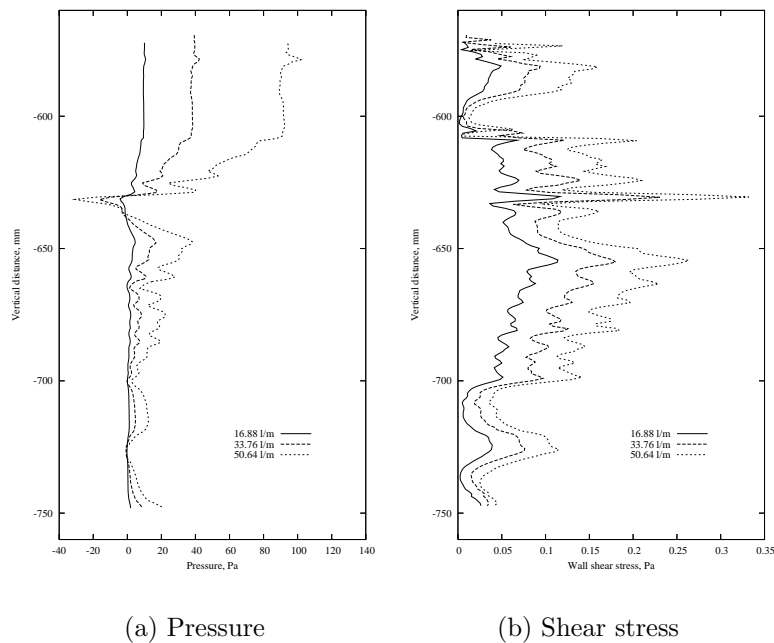
Figure 7.15: Pressure and shear stress distributions along the anterior wall up to bifurcation. The data is extracted approximately along the centre of the anterior surface

[30] P. Nithiarasu. Upper human airway fluid dynamics. *3rd Sym. on Multidisciplinary Research in Medical Sciences*, Swansea:Presentation, 23 May 2003.

[31] P. Nithiarasu, J.S. Mathur, N.P. Weatherill, and K. Morgan. Three-dimensional incompressible flow calculations using the characteristic based split (cbs) scheme. *International Journal for Numerical Methods in Fluids*, 44:1207–29, 2004.

[32] P. Nithiarasu. An arbitrary lagrangian eulerian (ale) method for free surface flow calculations using the characteristic based split (cbs) scheme. *International Journal for Numerical Methods in Fluids*, 48:1415–1428, 2005.

[33] P. Nithiarasu, R. Codina, and O.C. Zienkiewicz. The characteristic based split (cbs) scheme − a unified approach to fluid dynamics. *International Journal for Numerical Methods in Engineering*, 66:1514–1546, 2006.

[34] P. Nithiarasu, O. Hassan, K. Morgan, N.P. Weatherill, C. Fielder, H. Whittet, P. Ebden, and K.R. Lewis. Steady flow through a realistic human upper airway geometry. *International Journal for Numerical Methods in Fluids*, 57:631–651, 2008.

[35] R. Codina, H-C. Owen, P. Nithiarasu, and C-B. Liu. Numerical comparison of cbs and sgs as stabilization techniques for the incompressible navier-stokes equations. *International Journal for Numerical Methods in Engineering*, 66:1672–1689, 2006.

(a) Pressure   (b) Shear stress
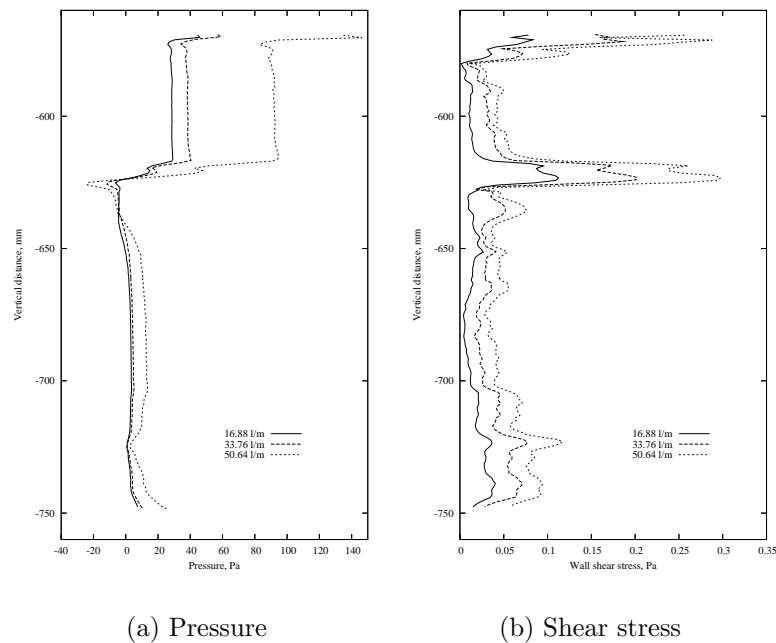
Figure 7.16: Pressure and shear stress distributions along the posterior wall up to bifurcation. The data is extracted approximately along the centre of the posterior surface

[36] N. Massarotti, F. Fausto, R.W. Lewis, and P. Nithiarasu. Explicit and semi-implicit cbs procedures for incompressible viscous flows. *International Journal for Numerical Methods in Engineering*, 66:1618–1640, 2006.

[37] P.R. Spalart, W.H. Jou, M. Strelets, and S.R. Allmaras. Comments on the feasibility of les for wings, and on a hybrid rans/les approach. *Advances in DNS/LES: First AFOSR International Conference on DNS/LES, Liu C and Liu Z (Eds), Greyden, Columbus, OH*, 1997.

[38] O.C. Zienkiewicz, R.L. Taylor, and P. Nithiarasu. *The finite element method for fluid dynamics*. Elsevier Butterworth-Heinemann, Elsevier Butterworth-Heinemann, Burlinton, MA, 2005.

[39] R. Löhner R, K. Morgan, and O.C. Zienkiewicz. The solution of non-linear hyperbolic equation systems by the finite element method. *International Journal for Numerical Methods in Fluids*, 4:1043–1063, 1984.

[40] A. Quarteroni, M. Tuveri, and A. Veneziani. Computational vascular fluid dynamics: problems, models and methods. *Computing and Visualization in Science*, 2(4):163–197, 2000.

[41] J.P. Mynard. One-dimensional blood flow modelling with the Locally Conservative Galerking (LCG) method. *MRes Thesis, Swansea University, Swansea, UK*, 2007.

[42] O.C. Zienkiewicz, R.L. Taylor, and P. Nithiarasu. *The Finite Element Method for Fluid Dynamics*. Elselvier, London, 6th edition, 2005.

[43] J.R. Womersley. Method for the calculation of velocity, rate of flow and viscous drag in arteries when the pressure gradient is known. *Journal of Physiology*, 127(3):553–563, 1955.

[44] J.R. Womersley. Oscillatory flow in arteries: the constrained elastic tube as a model of arterial flow and pulse transmission. *Physics in Medicine and Biology*, 2:178–187, 1957.

[45] J. R. Womersley. An elastic tube theory of pulse transmission and oscillatory flow in mammalian arteries. Technical Report TR 56-614, WADC Technical Report, 1957.

[46] C.A. Taylor, T.J.R. Hughes, and C.K. Zarins. Finite element modeling of blood flow in arteries. *Computer Methods in Applied Mechanics and Engineering*, 158(1-2):155–196, 1998.

[47] D.J. Penny and J.J. Smolich. Personal communication. 2007.

[48] A.F. Heenan, E. Matida, A. Pollard, and W.H. Finlay. Experimental measurements and computational modeling of the flow in an idealized human oropharynx. *Experimenta in Fluids*, 35:70–84, 2003.

[49] C. Kleinstreuer and Z. Zhang. Laminar-to-turbulent fluid-particle flows in a human airway model. *International Journal of Multiphase Flow*, 29:271–289, 2003.

[50] W-I. Li, M. Perzl, J. Heyder, R. Langer, J.D. Brain, K.-H. Englmeier, R.W. Niven, and D. A. Edwards. Aerodynamics and aerosol particle deaggregation phenomena in model oral-pharyngeal cavities. *Journal of Aerosol Science*, 27:1269–1286, 1996.